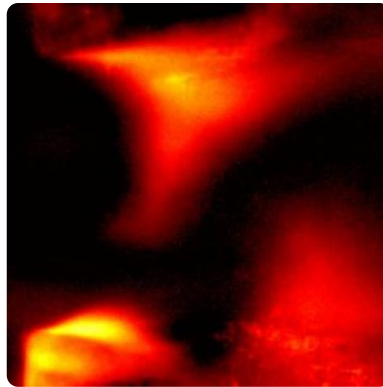




DEPARTMENT OF AEROSPACE ENGINEERING,
INDIAN INSTITUTE OF TECHNOLOGY MADRAS,
CHENNAI – 600 036

**RATE DEPENDENT TRANSITION TO THERMOACOUSTIC
INSTABILITY AND FLAME DYNAMICS DURING SCREECH
IN AN AFTERBURNER**



A Thesis
Submitted by
S. Manikandan

For the award of the degree
Of
DOCTOR OF PHILOSOPHY
Dec, 2021

THESIS CERTIFICATE

This is to certify that the thesis titled, **RATE DEPENDENT TRANSITION TO THERMOACOUSTIC INSTABILITY AND FLAME DYNAMICS DURING SCREECH IN AN AFTERBURNER**, submitted by me under the supervision of Prof. **R. I. Sujith**. The contents of this Thesis, in full or in parts, have not been submitted to any other Institute or University for the award of any degree or diploma.

The research work has been carried out at IIT Madras and Gas Turbine Research Establishment, DRDO.

Chennai 600 036
Date:

S. Manikandan
Research Scholar

Dr. S. Ganesan
Sc 'G', Group Director,
Gas Turbine Research
Establishment, DRDO
Bengaluru.

Prof. R. I. Sujith
Research Guide
Professor
Dept. of Aerospace Engineering
IIT Madras, 600 036

LIST OF PUBLICATIONS

The publications arising out of the work mentioned in this thesis are given as follows:

Manikandan, S., and R. I. Sujith. (2020). Rate Dependent Transition to Thermoacoustic Instability via Intermittency in a Turbulent Afterburner. *Experimental Thermal and Fluid Science*, 114, 110046.
<https://doi.org/10.1016/j.expthermflusci.2020.110046>.

Manikandan, S., Pawar, S. A., and Sujith, R. I. Spatio-temporal analysis of flame dynamics during transverse mode thermoacoustic instability. (In preparation)

To my wife, son, daughter, sister, parents and grandparents.

ACKNOWLEDGEMENTS

I am grateful to my guide, Prof. R. I. Sujith for showing me the culture required in a research environment that pushes the boundaries of scientific knowledge. I have observed students including myself being transformed to a researcher during their academic pursuit. He has been an inspiration for me to pursue an idea for life and overcome the self-doubts in taking such a route against jumping through opportunities.

I owe my wife, kids, sister and parents for bearing with me in not doing my family responsibilities and patiently supporting me through my doctoral program. I thank my grandfather for regularly motivating me to complete my doctoral program.

I thank the team: Dr. Abin Krishnan, Mr. Hashir Mohammed, Dr. Mridula Baro, Mr. Midhun Raghunath, and Mr. Dileesh, IIT Madras, for their perseverance in setting up the laborious facility and conducting strenuous experiments which included many failures. I thank Mr. Maari and his brother, Mr. Manimaran for fabricating the test section and accessories in a timely manner and responding several times to the patch work required in our experiment, with the consideration that they are contributing to the academic pursuit. I am grateful to Mr. Nitin, Mr. Praveen and Mr. R. Manikandan for their help in high-speed imaging the flame dynamics in the last phases of the experiment. I am thankful to Ms. Induja for helping with the phase portraits and recurrence plots. I thank, Dr. V. Ramanujachari, and Dr. V. Natarajan for sharing their valuable experiences and for their support. I need to emphasise that without the support of the experimental team, Prof. R. I. Sujith, Dr. V. Ramanujachari, and Dr. V. Natarajan, the experiments would not have been possible. I thank Dr. Amitesh for his discussions on the flame dynamics and correcting my thesis. I thank Ms. Veda Sri and Dr. Abin

Krishnan for correcting my journal paper. I thank Dr. Samadhan A. Pawar, IIT Madras for his fruitful discussions on the results presented in this study, correcting my thesis and journal paper over several revisions, and as a friend providing moral support.

I thank my friend Mr. Mukund Kumar Pandey for his moral support and long discussions during my tough times through the course of the program. I am grateful to all the professors who imparted me the importance of fundamental understanding of a subject during the course work. I thank my co-guide Dr. S. Ganesan for his encouragement and moral support in completing my doctoral program. I acknowledge the support and funding provided by Defense Research and Development Organization (DRDO), India.

ABSTRACT

KEYWORDS: Thermoacoustic instability; R-tipping; Rate dependent transition; Intermittency; Screech; Bluff-body flame holder; Flame dynamics; Vortex shedding; Vortex-Flame interaction; Afterburner.

Experiments were conducted to study the rate dependent transition to thermoacoustic instability in a turbulent afterburner rig. The afterburner rig contains v-gutters as flame stabilizers and simulates elevated inlet gas temperature using a preheater. Under quasi-static increase in flow Reynolds number of the afterburner, screech is not observed; on the contrary, screech onsets when the Reynolds number is increased at a higher rate. Such a phenomenon is known as rate-induced tipping or R-tipping. When the Reynolds number is increased at a lower rate, screech appears as a few bursts of high-amplitude periodic oscillations amidst low-amplitude aperiodic oscillations, a state known as intermittency. As the rate of change of Reynolds number is increased, more bursts appear and with further increase in the rate, the proportion of periodic oscillations of the bursts increases in the time series of pressure fluctuations, approaching a state of limit-cycle oscillations. We show for the first time, a rate-dependent transition to thermoacoustic instability in a turbulent afterburner happening through intermittency, with respect to increasing the rate of change of Reynolds number. The onset of burst occurs earlier, i.e., bursts occurring at a lower Reynolds number as the rate of change of Reynolds number is increased. The amplitude of bursts during intermittency is higher than that of the limit cycle oscillations. The rate dependent transition to screech through intermittency is analysed by studying the variation of probability density function (PDF) of the amplitude of pressure, variation of the amplitude of bursts, variation of the number of bursts of periodic oscillations, and the inlet conditions corresponding to the

onset of bursts, with respect to different rates of change of Reynolds number. Rate dependent transition observed in the model afterburner suggests that combustion system of a gas turbine engine should be subjected to different engine throttling rates to define the thermoacoustic stability map.

We studied the coupled interaction between p' and \dot{q}' using measurements of global unsteady heat release rate and acoustic pressure. As the Reynolds number is increased at a rate of 335 s^{-1} , the acoustic pressure transitions to sustained oscillations via bursts of periodic oscillations. The wavelet coherence plot provides information on the common spectral power which is an indicator of coupling strength and the phase relationship between the variables (known as phasors). We observe that the bursts of high coupling strength do not have the phasors aligned among them and the alignment increases as the number of bursts of high coupling strength increases. Secondly, we observe the state of bursts of high coupling strength even after the acoustic pressure transitioned from a state of bursts of oscillations to a state of sustained oscillations. The p' attains a state of periodic oscillations (as observed in RPs and probabilities of recurrence ($P(\tau)$) plots) earlier i.e. at a lower Reynolds number than the \dot{q}' and therefore, much of the increase in the cross-correlation coefficient between the $P(\tau)$ of p' and \dot{q}' is because of the increase in the coupling of \dot{q}' with p' .

Further, we captured the flame dynamics using planar measurements of unsteady heat release rate. We observe that alternate vortex shedding and the associated dynamics of unsteady heat release rate is responsible for the sustenance of transverse thermoacoustic instability. Though the mechanism is the vortex shedding, we show that the vortex roll-up itself does not generate acoustic energy. It is the flame ignition and extinction at the

immediate wake of the flame holder that drives the thermoacoustic instability. The suppression techniques devised for disrupting the acoustic sources, cannot be misled by the vortex-flame roll up and requires a thorough investigation before implementing such techniques. Also, we show that the patterns of the phasor field are a result of convection of reacting particles from the immediate wake to different zones of the combustor. Such an understanding can improve the modelling of the unsteady heat release rate of the thermoacoustic system.

TABLE OF CONTENTS

THESIS CERTIFICATE	i
LIST OF PUBLICATIONS	ii
ACKNOWLEDGEMENTS	iv
ABSTRACT	vi
LIST OF TABLES	xii
LIST OF FIGURES	xiii
ABBREVIATIONS	xix
NOTATIONS	xx
CHAPTER 1	21
INTRODUCTION	21
1.1. Literature survey	23
1.1.1. Brief History	26
1.1.2. Mechanisms of Thermoacoustic Instabilities	28
1.1.3. Resonance Vs Self-Excitation	33
1.1.4. Theoretical Modelling Approaches	34
1.1.5. Complex Systems Approach.....	40
1.2. Interim summary and motivation.....	52
1.3. Objective of this thesis	54
1.4. Overview of this thesis.....	56
CHAPTER 2	58
EXPERIMENTAL SETUP AND INSTRUMENTATION	58
2.1. Experimental setup.....	58
2.2. Afterburner geometry.....	59
2.2.1. Other geometries experimented to obtain transverse thermoacoustic instability.....	61
2.3. Controls for the study of rate-dependent transition	63
2.4. Instrumentation	64

2.4.1. Location of pressure transducers in the test section	65
2.5. Experimental procedure	66
CHAPTER 3	68
RATE DEPENDENT TRANSITION TO THERMOACOUSTIC INSTABILITY VIA INTERMITTENCY	68
3.1. Rate induced tipping of screech	70
3.2. Rate dependent transition of screech via intermittency	71
3.3. Analysis of intermittency	72
3.3.1. Analysis of intermittency using recurrence plot	73
3.3.2. Probability distribution of the amplitude of pressure	78
3.3.3. Variation of the amplitude of bursts	80
3.3.4. Variation of the number of bursts	82
3.3.5. Promotion of rate dependent transition.....	83
3.4. Summary	88
CHAPTER 4	90
FLAME DYNAMICS DURING TRANSVERSE THERMOACOUSTIC INSTABILITY	90
4.1. Global flame dynamics during thermoacoustic instability	90
4.2. Mechanism causing transverse thermoacoustic instability	99
4.3. Spatio-temporal analysis of flame dynamics:	107
4.4. Propagation speed of intensity fluctuations:	109
4.5. Summary	114
CHAPTER 5	117
CONCLUSIONS AND SCOPE FOR FUTURE WORK	117
5.1. Scope for future work	119
APPENDIX ‘A’	121
ACOUSTIC FIELD IN THE MODEL AFTERBURNER AND EFFECT OF ORIENTATION OF FUEL INJECTION ON TRANSVERSE THERMOACOUSTIC INSTABILITY	121
A. 1. Acoustic field in the model afterburner	121

A. 2. Effect of orientation of fuel injectors on transverse thermoacoustic instability	128
A. 3. Summary	130

REFERENCES

132

LIST OF TABLES

Table 4.1 :	Relationship between p' at the bottom wall of test section and u_y'	102
Table A.1 :	Constants obtained from curve fit to the amplitude distribution of acoustic pressure.....	124
Table A.2 :	Frequency components and sound speed.....	125

LIST OF FIGURES

Figure 1.1:	(a) Thermoacoustic instability is caused by mutual interaction between flow instabilities, combustion dynamics, and acoustics in the combustion chamber. (b) Acoustic modes act as a feedback to the flow and combustion processes.	21
Figure 1.2:	(a) The effect of unsteady heat release rate in-phase with acoustic pressure, results in increasing amplitude of acoustic pressure. (b) The effect of unsteady heat release rate out-of-phase with acoustic pressure, results in decreasing amplitude of acoustic pressure.....	22
Figure 1.3:	Direction of acoustic oscillations that are excited in cylindrical combustors. Adapted from (Lieuwen and Yang, 2006).	23
Figure 1.4:	A chronology of thermoacoustic instabilities. Adapted from (Culick and Kuentzmann, 2006).....	26
Figure 1.5:	Thermoacoustic interactions in gas turbine combustors. Adapted from (Paschereit et al., 2001).....	29
Figure 1.6:	Vortex roll-up in dump combustor. Adapted from (Schadow and Gutmark, 1992).....	30
Figure 1.7:	Distinct features between resonance and self-excitation. Adapted from (Culick and Kuentzmann, 2006).....	34
Figure 1.8 :	Supercritical Hopf bifurcation.	49
Figure 2.1:	(a) Picture of air supply facility which can simulate afterburner inlet conditions. (b) Schematic of the air supply facility. The air supply facility is a blow-down facility with a kerosene burner (preheater) connected upstream of the afterburner through a plenum.	59
Figure 2.2:	(a) The schematic of the afterburner used in the present study. (b) The afterburner contains three sets of flame holder, fuel injector and spark plug, and are arranged as shown. (c) Dimensions of the flame holder. (d) Zoomed-in view of the flame holder, fuel injector, spark plug, and dynamic pressure transducer.	60
Figure 2.3 :	Test section with optical access on one side of the test section covering full test-section height.....	61
Figure 2.4 :	(a) Initial test section with flanged side plates did not encounter transverse thermoacoustic instability. (b) Picture of test section	

with many flanges during afterburning with three-flame-holder configuration. The red-hot appearance in the picture is due to metal heating by the flame inside the test section.	63
Figure 2.5 : (a) LabView interface. (b) calibration curve for air flow rate vs valve opening for the globe valve. The plotted curves are obtained over multiple trials of valve opening.	64
Figure 2.6: Locations of the pressure transducers, region of high-speed imaging and region accessible to PMT are shown in the schematic of the model afterburner.	66
Figure 3.1 : (a) The amplitude spectrum of pressure fluctuations (b) Cross correlation of the pressure signals obtained from the top and the bottom sides of the rectangular afterburner.	69
Figure 3.2 : The plot of acoustic pressure and the Reynolds number corresponding to the rate of change of Reynolds number (\dot{Re}_{avg}) of (a) 121.5 s^{-1} (screech did not occur), and (b) $1,143.1 \text{ s}^{-1}$ (screech occurred). The fuel flow rate of the preheater and the afterburner for this experiment is 22 lph and 41 lph, respectively.	70
Figure 3.3 : Time series of acoustic pressure and the corresponding Reynolds number is plotted for increasing rate of change of Reynolds number from (a) to (f). A magnified view of aperiodic oscillations and periodic oscillations during bursts is shown in (a). The fuel flow rate of the preheater and the afterburner for this experiment is 29 lph and 41 lph, respectively.	72
Figure 3.4 : Phase portrait of different dynamical states of the acoustic pressure for the rate of change of Reynolds number, $\dot{Re}_{avg} = 456.4 \text{ s}^{-1}$ obtained for 80 ms. (a) Aperiodic oscillations between bursts ($\tau = 15$, $d_o = 11$), (b) Oscillations at the onset of a burst ($\tau = 4$, $d_o = 11$) and (c) periodic oscillations during a burst ($\tau = 4$, $d_o = 11$).	75
Figure 3.5 : Recurrence plot (RP) of the time series of acoustic pressure of the three different dynamical states with $\dot{Re}_{avg} = 456.4 \text{ s}^{-1}$ plotted for duration of 20 ms : (a) aperiodic oscillations ($\tau = 8$, $d_o = 11$, $\epsilon = 35\%$), (b) Onset of a burst ($\tau = 5$, $d_o = 11$, $\epsilon = 35\%$) and (c) periodic oscillation during burst ($\tau = 4$, $d_o = 11$, $\epsilon = 35\%$).....	76
Figure 3.6 : The variation of the mean recurrence rate corresponding to the rate of change of Reynolds number.	78

Figure 3.7 : (a) The amplitude of acoustic pressure which is band pass filtered, corresponding to $\dot{Re}_{avg} = 143.3 \text{ s}^{-1}$. (b) The PDF of amplitude of acoustic pressure for different rates of change of Reynolds number (\dot{Re}_{avg}).....	80
Figure 3.8 : Plot of the average amplitude (μ) of bursts of periodic oscillations and the corresponding standard deviation (σ) of the amplitude distribution for different rates of change of Reynolds number (\dot{Re}_{avg}).....	82
Figure 3.9 : The number of bursts in the time series of pressure is plotted for different rates of change of Reynolds number (\dot{Re}_{avg}).....	83
Figure 3.10 : The onset of burst of periodic oscillations depends on the rate of change of air flow rate. The air flow rate corresponding to the onset of a burst of periodic oscillations is plotted for different preheater and afterburner fuel flow rates: (a) 23 lph (b) 26 lph and (c) 29 lph. Rate of change of air flow rate (r_a), mass flow rate of air corresponding to onset of screech ($\dot{m}_{a,s}$), mass flow rate of fuel in the model afterburner ($\dot{m}_{f,AB}$).....	84
Figure 3.11 : The Reynolds number corresponding to the onset of a burst of periodic oscillations for different rates of change of Reynolds number.....	85
Figure 3.12 : (a) The promotion of Reynolds number corresponding to the onset of a burst of periodic oscillations for different fuel flow rates in the afterburner. (b) The corresponding plot in terms of delay in equivalence ratio.....	86
Figure 3.13 : (a) The variation of frequency of periodic oscillations in the time series of pressure for a given rate of change of Reynolds number. (b) The maximum dominant frequency of periodic oscillations for different rates of change of Reynolds number.....	88
Figure 4.1 : (a) Time series of acoustic pressure and global heat release rate corresponding to flame dynamics of bottom flame holder. (b) Zoomed-in view of the time series for a duration of 50 ms (c) Amplitude spectrum of pressure and unsteady heat release rate obtained for a duration of 100 ms. (d), (e), and (f) correspond to amplitude scalogram of pressure, amplitude scalogram of and unsteady heat release rate, and wavelet coherence between acoustic pressure and unsteady heat release rate, respectively.....	94

Figure 4.2 : Mean and standard deviation of relative phase between p' and q' corresponding to dominant frequency of 1270 Hz and with wavelet coherence greater than 0.75 obtained for every two second data of p' and q' . The back dots correspond to the three dynamical states used in Figure 4.1.	95
Figure 4.3 : (a) Time series of acoustic pressure and global heat release rate corresponding to flame dynamics of bottom flame holder. Columns (I) – (III) represent RPs of p' and q' , and $P(\tau)$, respectively, corresponding to the dynamical states marked in (a) as Row (b), Row (c) and Row (d). The parameter's values used in RPs of p' and q' are $d_o = 12$, $\epsilon = 20\%$ and $d_o = 12$, $\epsilon = 20\%$, respectively.	98
Figure 4.4 : The variation of CPR shows a steep increase in coupling strength compared to the variation in rms of p'	99
Figure 4.5 : Frames I – IV are phase averaged images corresponding to minimum, zero (positive slope), maximum, and zero (negative slope) of the p' measured at the bottom wall of the test section, respectively.	100
Figure 4.6 : (a) Relationship between p' at the bottom side of the test section and u_y' in time. (b) Phase portrait of the p' and u_y' . The positive velocity is taken in the direction pointing towards top side from bottom side of the test section.	102
Figure 4.7 : Conceptual sketch describing the in-phase flapping of stream-1 and stream-2 with respect to acoustic velocity direction, resulting in asymmetric flame structure. Flame structure during (a) positive transverse velocity (b) negative transverse velocity.	103
Figure 4.8: Time series of unsteady heat release rate between top and bottom flame holder obtained from high-speed images (at 25 mm) along with acoustic pressure.	104
Figure 4.9 : Amplitude spectrum of acoustic pressure, \dot{q}'_{top} and \dot{q}'_{bottom}	105
Figure 4.10 : (a) Schematic depicting the axial locations where time series of local q' is derived from high-speed images. (b) – (g) Correlation and phase between p' and local q' shown using wavelet coherence plots.	106
Figure 4.11 : Time-averaged amplitude and phase of unsteady heat release rate obtained during thermoacoustic instability. The amplitude and	

phase angle are plotted as contour and vectors, respectively. The shaded region denotes the region without flame.	107
Figure 4.12 : (a) Rayleigh index obtained over a time period of integration of 2 seconds and is plotted as contours. The vectors denote the phase difference between the unsteady heat release rate and the acoustic pressure. (b) Variation of amplitude of p' along the height of the test section for the first transverse mode. The dotted line is in the region of the test section that is outside the imaging region. (c) And corresponding phase of p' along the height of the test section	109
Figure 4.13 : Magnitude of propagation velocity of intensity fluctuations is plotted as contours overlaid with propagation velocity vectors.	112
Figure 4.14 : Stream lines drawn using the vectors of propagation velocity of intensity fluctuations.....	113
Figure 4.15 : Paths traced by intensity fluctuations starting from four points in the vicinity of the bottom flame holder and reaching different regions of the pattern formed by the phasor plot. The streamline paths are overlaid on the vectors of (a) propagation velocity of intensity fluctuations, (b) phasors obtained between intensity fluctuations and acoustic pressure.	114
Figure A.1 : Variation of amplitude and phase of acoustic pressure obtained in the region upstream of flame holders corresponding to the transducers numbered as 2 to 8 in Figure 2.6.	122
Figure A.2 : Fit of the amplitude equation of impedance tube to the amplitude distribution of acoustic pressure obtained from the experiment.....	124
Figure A.3 : Longitudinal oscillation velocity field in the region upstream of flame holders.	127
Figure A.4 : Instantaneous plot of vectors of acoustic velocity in the region upstream of flame holders. The velocity pattern moves with time. Three dots represent the location of fuel injectors. The origin in the longitudinal axis represents the leading edge of flame holders.....	128
Figure A.5 : Schematic of the fuel injector orientations used for all the injectors, starting from transverse injection to injection in line with the flow direction. The effect of the injector orientation on transverse thermoacoustic instability is studied.....	129
Figure A.6 : The variation of RMS of p' with respect to the flow Reynolds number for different fuel injector orientation such as 90°	

(transverse injection), 60°, 30°, and 0° (in line with the flow direction).....130

ABBREVIATIONS

FTF	Flame Transfer Function
FDF	Flame Describing Function
OH PLIF	OH* Planar Laser Induced Fluorescence
PIV	Particle Imaging Velocimetry
lph	litre per hour
FSR	Full Scale Reading
BFSL	Best Fit Straight Line
max	maximum
min	minimum
avg	average
LPG	Liquified Petroleum Gas
PDF	Probability Density Function
RP	Recurrence Plot
CPR	Cross correlation coefficient of Probability of Recurrence

NOTATIONS

p'	acoustic pressure (Pa)
\dot{q}'	unsteady heat release rate
$P(\tau)$	probability of recurrence
\dot{m}_a	mass flow rate of air (kg/s)
r_a	rate of change of air flow rate ($kg/s/hr$)
$\dot{m}_{f,AB}$	mass flow rate of fuel of the model afterburner (lph)
\dot{Re}_{avg}	average rate of change of Reynolds number (s^{-1})
$\dot{\phi}_{avg}$	average rate of change of equivalence ratio (hr^{-1})
ϕ_{ph}	equivalence ratio of the preheater
ϕ_{ab}	overall equivalence ratio at the afterburner including the fuel flow rate of the preheater
μ	mean of probability distribution function of amplitude of pressure oscillations (kPa)
σ	standard deviation of probability distribution function of amplitude of pressure oscillations (kPa)
$\dot{m}_{a,s}$	mass flow rate of air corresponding to onset of screech (kg/s)
Re_s	Reynolds number corresponding to the onset of a burst of periodic oscillations
$Re_{s,1}$	Re_s corresponding to $\dot{Re}_{avg} = 1 s^{-1}$ and is obtained by extrapolation
ϕ_s	equivalence ratio corresponding to the onset of a burst of periodic oscillations
$\phi_{s,1}$	ϕ_s corresponding to $\dot{Re}_{avg} = 1 s^{-1}$ and is obtained by extrapolation
x	horizontal axis of the test section
y	vertical axis of the test section

CHAPTER 1

INTRODUCTION

Thermoacoustic instability is a plaguing problem in combustion chambers such as the ones used in gas turbines, ramjets, rocket motors and furnaces. Thermoacoustic instability manifests itself as high amplitude pressure oscillations in combustion systems. Such instability is caused by a mutual interaction between the flow instabilities, combustion dynamics, and the acoustic field in the combustion chamber, and manifests itself as acoustic oscillations (Figure 1.1a). Commonly, the acoustic modes act as a feedback to the flow and combustion processes (Candel, 2002), as shown in Figure 1.1b.

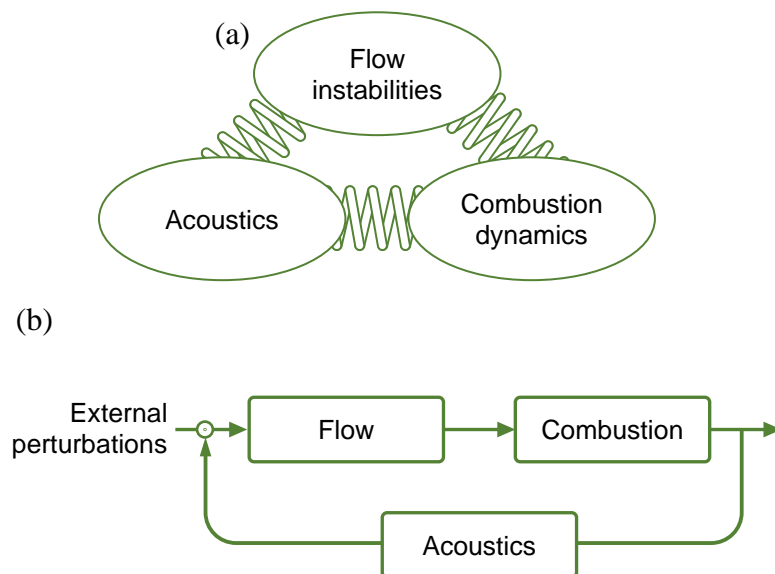


Figure 1.1: (a) Thermoacoustic instability is caused by mutual interaction between flow instabilities, combustion dynamics, and acoustics in the combustion chamber. (b) Acoustic modes act as a feedback to the flow and combustion processes.

The acoustic pressure oscillations increase in amplitude, when they are in phase with the heat release rate oscillations and also if the production of acoustic energy overcomes the acoustic damping in the system (refer Figure 1.2) (Rayleigh, 1878). The phase relationship between the pressure oscillations and the heat release rate oscillations is controlled by the time delay between the response of physical processes such as atomization, vaporization, mixing, ignition delay, etc. and the acoustic perturbations that is affecting the physical processes (Candel, 2002). The acoustic pressure oscillations eventually saturate to limit cycle oscillations, when the acoustic energy fed by the unsteady heat release rate into the combustor is balanced by the acoustic losses in the combustor. These high-amplitude pressure oscillations can have catastrophic consequences such as reduced life or even failure of the components due to increase in thermal and mechanical stresses(Lieuwen and Yang, 2006).

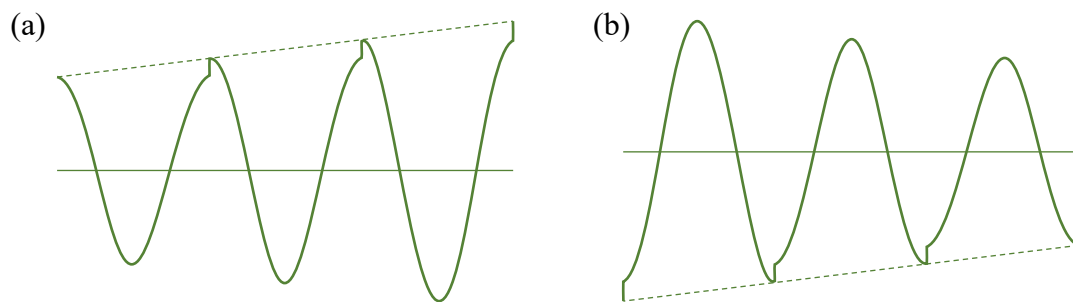


Figure 1.2: (a) The effect of unsteady heat release rate in-phase with acoustic pressure, results in increasing amplitude of acoustic pressure. (b) The effect of unsteady heat release rate out-of-phase with acoustic pressure, results in decreasing amplitude of acoustic pressure.

On the other hand, the stable operation of the combustor is associated with broadband spectra of acoustic pressure fluctuations due to underlying turbulent combustion and is referred to as combustion noise (Strahle, 1978). In a combustion chamber, the state of combustion noise manifests as low-amplitude aperiodic oscillations of pressure.

Dowling and Mahmoudi (2015) provide an excellent review of the developments in the understanding of the sources of combustion noise.

Thermoacoustic instability occurs as sharp tones in one or more of the natural acoustic modes of the combustion chamber. Such instabilities are broadly categorized as rumble, buzz, and screech, based on the frequency of the instability. The rumble and buzz are associated with the frequency range of 50 – 1,000 Hz and are usually observed as longitudinal acoustic oscillations. The screech is associated with frequencies greater than 1,000 Hz and is usually observed as transverse acoustic modes in the form of tangential or radial acoustic oscillations (Culick, 1988; Ghani et al., 2015; Kerbs et al., 2006; Mongia et al., 2006).

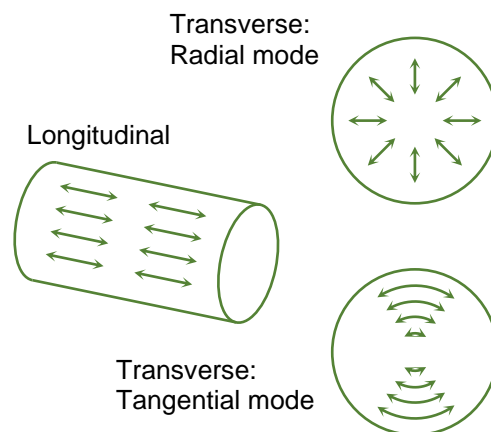


Figure 1.3: Direction of acoustic oscillations that are excited in cylindrical combustors. Adapted from (Lieuwen and Yang, 2006).

1.1. LITERATURE SURVEY

In early investigations of thermoacoustic instability, unsteady heat release rate was assumed as forcing the acoustic oscillator. A time delay description of the forcing function was commonly used for the unsteady heat release rate and is known as Crocco's n - τ model (CROCCO et al., 1960). Interaction index (n) and time-lag (τ) of

the model was deduced for combustion systems to arrive at thermoacoustic stability map of combustion systems. Later, the n - τ model was extended as Flame Transfer Function (FTF) by studying response of the flame subjected to pressure or velocity excitation depending on the type of combustion systems (Andreini et al., 2014; Hemchandra et al., 2011; Rani and Rani, 2018; Schuller et al., 2003; Schuller et al., 2002). Further, the model is refined through introduction of nonlinearities in the transfer function and is known as Flame Describing Function (FDF) in order to account for the occurrence of limit cycle oscillations (Dowling, 1997, 1999; Durox et al., 2009; Schwing et al., 2011). In the pursuit of describing several phenomena observed in the transition to thermoacoustic instability, stochastic description was also introduced in the modelling of the thermoacoustic system (Bonciolini et al., 2017; Noiray and Schuermans, 2013b).

In the last couple of decades, thermoacoustic system was investigated from the perspective of complex systems. A complex system is a system whose distinct behaviour arises out of the relationships or interactions between the components of the system. Study of complex systems is interdisciplinary drawing from sociology, genetics, economics, ecology, immunology, city planning, mathematics, embryology, computer science, politics, etc. Complex systems exhibit distinct behaviours such as nonlinearity, emergence, spontaneous order, adaptation, and feedback loops, etc. (Tranquillo 2019). The distinct behaviours of complex systems arise out of interactions at the local level rather than from a central planning. Simple coupling rules between the components can produce interesting behaviours which are not observed inherently in the components. Thermoacoustic systems are shown to exhibit behaviours of complex systems such as self-organization (George et al., 2018), synchronization (Pawar et al.,

2017), nonlinearity (Sterling and Zukoski, 1991), etc. due to the interaction between acoustics and combustion processes.

Tools to study complex systems include chaos and fractals, game theory, networks, agent-based models and information theory (Tranquillo 2019). Statistical mechanics is an important tool in the study of complex systems. In statistical mechanics, the advances in the understanding of phase transition and critical phenomena led to two important concepts: scaling and universality (Stanley, 1987). Around the phase transition from water to water vapour, the density (order parameter) changes with increase in temperature (control parameter) in a power-law relationship. The exponent of the power-law is called as critical exponent and is observed to have same value in many different systems, thus universality. The critical exponent is 4 for phase transitions, 6 for percolation, etc. (Bunde and Havlin, 1996). Similarly, the scaling behaviour during the transition to thermoacoustic instability is observed to be universal with the emergence of other oscillatory instabilities in turbulent flows (Pavithran et al., 2020).

Thermoacoustic instability is a disturbing problem for the industry which uses combustion systems. Many passive control devices such as Helmholtz resonators, anti-screach liners, baffles, etc. are used in the mitigation of thermoacoustic instability. These devices are effective for a few targeted frequencies and mostly for high frequencies. The alternate view that thermoacoustic system is a complex system, provides new insights in the occurrence of thermoacoustic instability and creates opportunities to adopt concepts such as amplitude death from synchronization theory, disruption of critical regions from complex network theory, etc. These concepts provide

additional flexibility in the design of such devices, that makes them effective for wide range of operational regime of the combustion systems.

1.1.1. Brief History

Thermoacoustic instability is first reported by Higgins in 1802 and is observed as early as 1777, then referred to as ‘singing flames’ (Jones, 1945). Higgins was demonstrating that water is a combustion product of hydrogen-air flames. During the experiment, he lowered a vertical glass tube into the hydrogen-air flame to collect the moisture, unexpectedly the flame ‘sang’. Since then, several hypotheses have been proposed to explain the singing flame. Rayleigh theory provided the condition under which singing flame occurs, and is been used till date (Rayleigh, 1878).

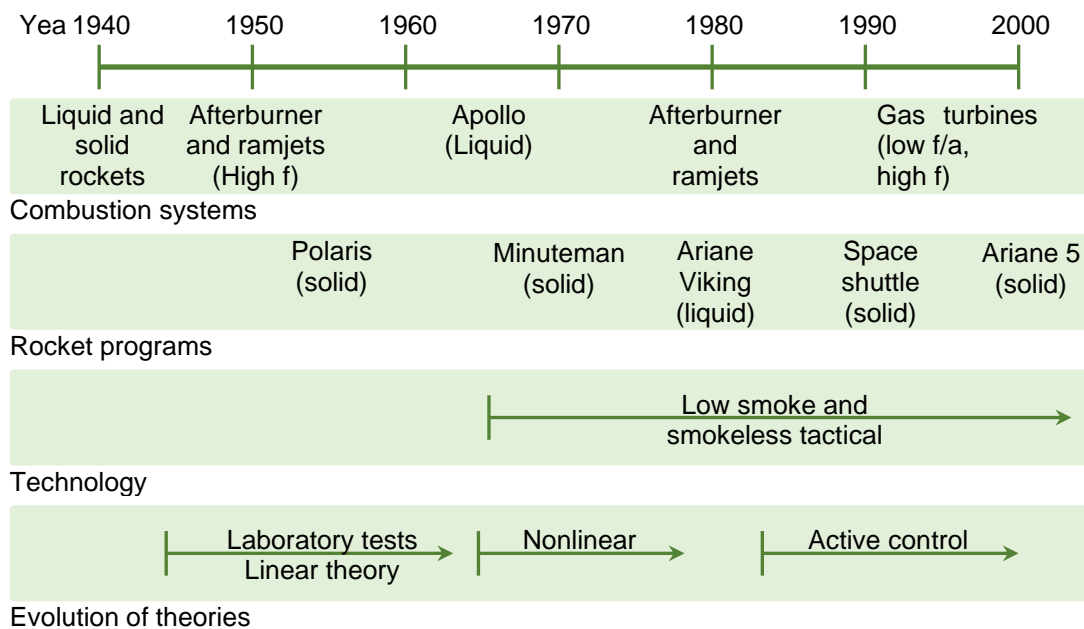


Figure 1.4: A chronology of thermoacoustic instabilities. Adapted from (Culick and Kuentzmann, 2006).

The impact of thermoacoustic instability was first observed in the early 1940s during the development of liquid and solid propellant rockets. Figure 1.4 is a qualitative representation of the chronology of thermoacoustic instabilities, adopted from (Culick

and Kuentzmann, 2006). History of thermoacoustic instability observed in various combustion systems are as follows:

Rockets: Major efforts on thermoacoustic instability during 1960s were motivated by requirements of the Apollo vehicle. The F-1 encountered instabilities with amplitudes greater than 100% of mean pressure (mean pressure of 70 bar) with frequency range of 200-500 Hz. The suppression of instabilities in F-1 engine development required costly trial and error with large number of full-scale tests (~2000 tests) leading to four-year delay in the program. Since then, other rocket development programs such as Space Shuttle solid-propellant rocket boosters, the Minuteman intercontinental ballistic missile, and the Mars Pathfinder descent motor, faced problems of thermoacoustic instability (Culick and Kuentzmann, 2006).

Afterburners: Higher performance requirements from afterburners and ramjets required operation of these combustors near stoichiometric fuel-air ratios. High frequency oscillations known as screech, is treated with passive suppression devices such as acoustic liners. Acoustic liners are found in every afterburner of a gas turbine engine suggestive of its effectiveness in suppressing the thermoacoustic oscillations. NACA report (Trout et al., 1956) summarizes the work done on screech in NACA Lewis laboratory prior to 1954. The increase of high-bypass ratio engines led to lower instability frequencies due to large annular passages of bypass duct which allows the acoustic waves to travel longer. Low frequencies are not easily attenuated by acoustic liners and so modifications in the scheduling of fuel injection is the main strategies for treating such low frequency oscillations. The presence of low frequency oscillations often limits the operating envelope of the afterburner.

Ramjets: The combustors of ramjets are similar to that of afterburners particularly in the use of bluff bodies as flame holders. In the late 1970s and 1980s, research programs on the thermoacoustic instabilities in ramjet engines were initiated by several countries (Clark, 1984; Culick and Rogers, 1980; Sivasegaram et al., 1989). The important understanding from the works of that period, about the cause of thermoacoustic instability in ramjets is the coupling between acoustics and large coherent vortex structures shed by the bluff bodies. Most intense oscillations occurred near stoichiometric fuel-air ratios (Rogers, 1956).

Main combustor of gas turbines: Main combustors were relatively without troublesome oscillations due to large acoustic losses. With the increasing use of gas turbines for power generation, and the importance on reducing NO_x in the 1980s, drove the designers of combustors to a strategy of maintaining lean combustion in the primary zone. Unfortunately, the flame stabilization is poor for lean fuel-air mixtures and tend to encourage the excitation of thermoacoustic instability (Lieuwen and Yang, 2006).

1.1.2. Mechanisms of Thermoacoustic Instabilities

The mechanisms of thermoacoustic instabilities refer to the processes that cause transfer of energy to the acoustic fluctuations from other sources. The primary source of acoustic energy is derived from unsteady heat release rate in the combustion systems. The processes that lead to unsteady heat release rate and the acoustic feedback is shown in Figure 1.5.

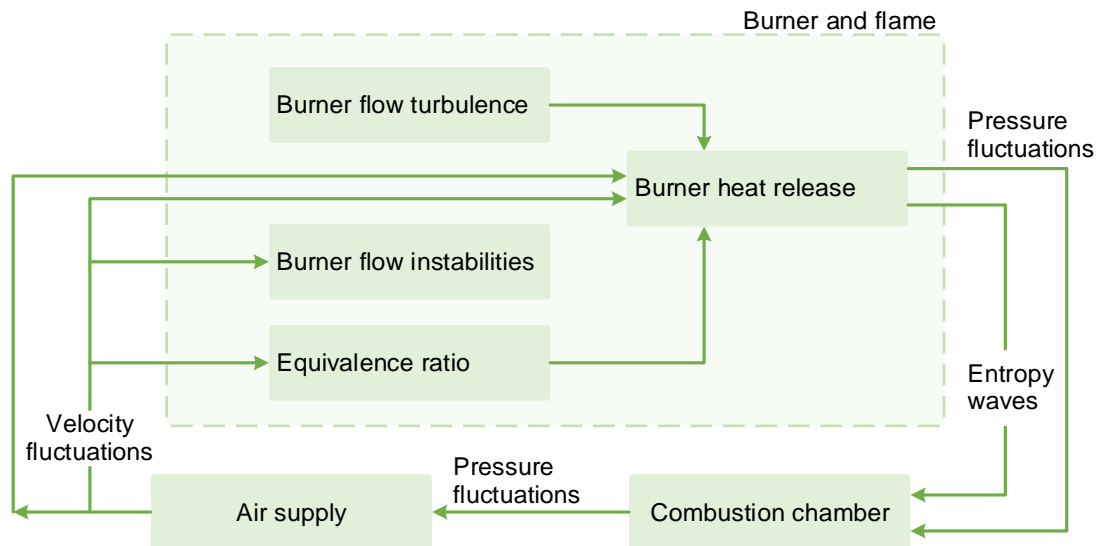


Figure 1.5: Thermoacoustic interactions in gas turbine combustors. Adapted from (Paschereit et al., 2001)

1.1.2.1. *Formation of Large-Scale Coherent Structures:*

In combustion systems, flame holding devices such as bluff-bodies, swirlers, rearward facing steps, etc. are used to anchor flame in the wake of such devices (Zukoski and Marble, 1955). The wake of the flame holding device contains shear layers formed between the high-speed flow in the combustor and the low-speed recirculation zone behind the flame holding device. These shear layers develop instability waves, known as Kelvin-Helmholtz instability, in its initial region. The instability waves grow exponentially with downstream distance and are observed to roll up into vortices (Ho, 1984). These vortices further undergo coalescence or collectively interact to form large coherent structures.

A periodic shedding of large-scale coherent structures is observed in the shear layers of the flame holding devices during the occurrence of thermoacoustic instability. The frequency of shedding of the coherent structures matches with the acoustic frequency of the combustion chamber. The role of vortex shedding in driving acoustic oscillations

was studied by several investigators (Hegde et al., 1987; Parkar et al., 1979; Pitz and Daily, 1983; Poinso et al., 1987; Smith and Zukoski, 1985; Yu et al., 1991). The formation of coherent structures results in large scale mixing of hot combustion products from the recirculation zone and the fresh mixture of reactants as depicted in Figure 1.6. However, fine scale or molecular mixing is required to initiate combustion. Such molecular mixing happens at the interface of the roll-up, resulting in flame front wrinkling. The periodic shedding of vortex leads to an oscillatory consumption of the reactants, consequently an oscillatory heat release rate (Emerson et al., 2011). In some cases, the coherent structures impinge on the combustor walls or exhaust nozzle resulting in vigorous mixing of the remaining unburnt reactants and the combustion products, leading to sudden release of heat (Smith and Zukoski, 1985; Yu et al., 1991). There are different mechanisms through which the large coherent structures transition to small scale turbulence such as vortex interaction, vortex impingement or collision with each other or on a solid surface, and vortex merging (Schadow and Gutmark, 1992).

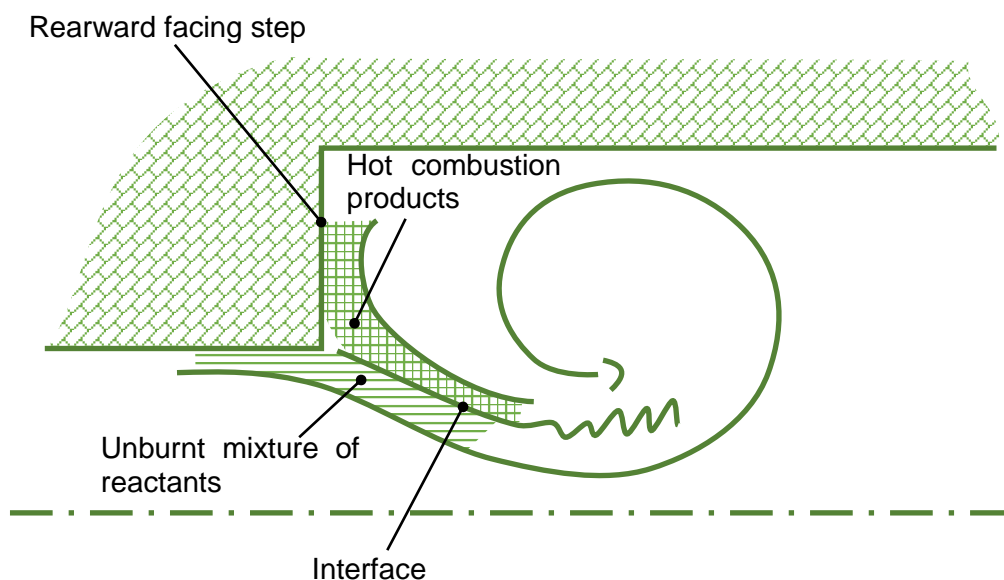


Figure 1.6: Vortex roll-up in dump combustor. Adapted from (Schadow and Gutmark, 1992).

In cylindrical combustion chamber, tangential modes are excited due to asymmetric shedding of vortex from the bluff body flame holders. Blackshear (1955) studied the mechanism of screech using a cylindrical combustor with diametrically positioned V-gutter. The first tangential mode was excited and the pressure node was along the V-gutter. Two single point flame ion sensing instruments (ionization gaps) installed 180° opposite, $\frac{3}{4}$ inch protruding into the combustor were used to measure the oscillation of flame. During screech, the ionization gaps picked up an oscillating signal (i.e., the flame front stroked the sensor in a periodic manner) and are out of phase between the two sensors. The outward flame front motion is in phase with the corresponding pressure signal at that location.

The vortex shedding is induced by the transverse acoustic velocity at the lip of the bluff body flame holders. Rogers & Marble (1956) reported that the mechanism that caused instability is periodic vortex shedding from the lip of the bluff body that occurs at the same frequency as the transverse oscillations. The vortex shedding is induced by the transverse velocity oscillation and convected through the shear layer. The vortex entrains the bulk of unburnt reactants with hot recirculating wake generating a combustion pulse with a time delay. He proposed that the vortex stretches the flame front leading to flame front area fluctuations.

An interesting result apart from the prevailing understanding in the late 1950s is the hysteresis in the occurrence of screech. Elias (1959) studied the effect of inlet air turbulence on the occurrence of screech in a rectangular duct with triangular flame holders. The decreasing turbulence level increased the screech hysteresis. At low turbulence level, the onset of screech occurred at high fuel-air ratio and return to smooth

combustion happened at lower fuel-air ratio compared to high turbulence. The low turbulence level has wide range of fuel-air ratio susceptible to screech. Also, in general, increasing mass flow rate lowered the screech hysteresis zone.

The shed vortex from the flame holders contains unburnt mixtures and impinges on the combustor walls resulting in sudden heat release. Smith & Zukoski (1985) captured phase-locked shadowgraph images of vortex shedding in a step combustor. The vortex forms and impinges against the lower combustor wall. This vortex impingement causes vigorous mixing and completes the reaction of remaining unburnt reactants. Poinso et al. (1987) conducted experiments in multiple inlet dump combustor and captured the spark-schlieren pictures of vortex shedding and vortex cap formation in the dump region.

1.1.2.2. *Equivalence Ratio Fluctuations*

The acoustic pressure oscillations in the combustion chamber propagate upstream and create an oscillatory pressure difference across the fuel injectors. This results in modulation of fuel flow rates varying periodically in time. Similarly, the acoustic velocity oscillations at the inlet of the combustion chamber lead to oscillatory air flow rates into the combustion chamber. The fluctuations in the air and fuel flow rates results in equivalence ratio fluctuations. Gas mixtures with varying equivalence ratio convect into the flame and generate an oscillatory heat release rate which drive the acoustic field. The ratio of the convective time between the injector and the flame, and the acoustic time period is a determining factor in the driving of acoustic oscillations. Lean fuel-air mixtures are particularly sensitive to equivalence ratio fluctuations. Recent increase in use of low NO_x combustor which maintain lean fuel-air mixtures in the

primary zone are susceptible to thermoacoustic instability driven by equivalence ratio fluctuations.

1.1.2.3. *Oscillatory Spray Dynamics*

Interaction of acoustic field with the fuel injectors and fuel supply lines causes a time-varying spray characteristic. The spray characteristic that are modulated are fuel penetration, atomization, evaporation rate, etc. In cross stream fuel injection, the spray penetration is a function of square of air stream velocity. Therefore, the acoustic velocity oscillation at the location of fuel injector leads to oscillatory penetration of fuel. The resultant wavy distribution of fuel in space is convected into the flame generating an oscillatory heat release rate (Shcherbik et al., 2009). The drop size, drop size distribution, and atomization periodicity is found to affect the onset of thermoacoustic instability (Anderson et al., 1998).

1.1.3. Resonance Vs Self-Excitation

In resonance phenomena, the responsible processes are called as linear because the governing differential equations are linear in the system variables. The transient in the linear system forced by an invariant external agent grows according to the form $p' = 1 - e^{-\beta t}$, as shown in Figure 1.7(a). The system variable approaches a limiting value for a linear system because the driving agent supplies only finite power. On the other hand, the self-excited phenomena, features an exponential growth in the transient phase, and approaches a limit-cycle oscillation as shown in Figure 1.7(b). The initial transient is governed by linear processes, and the saturation of the amplitude of the oscillations is governed by nonlinear processes in the system. Thermoacoustic instability exhibits

characteristics of self-excited system and therefore, to understand and control the behaviour of thermoacoustic system, the nonlinear process in the system has to be well understood.

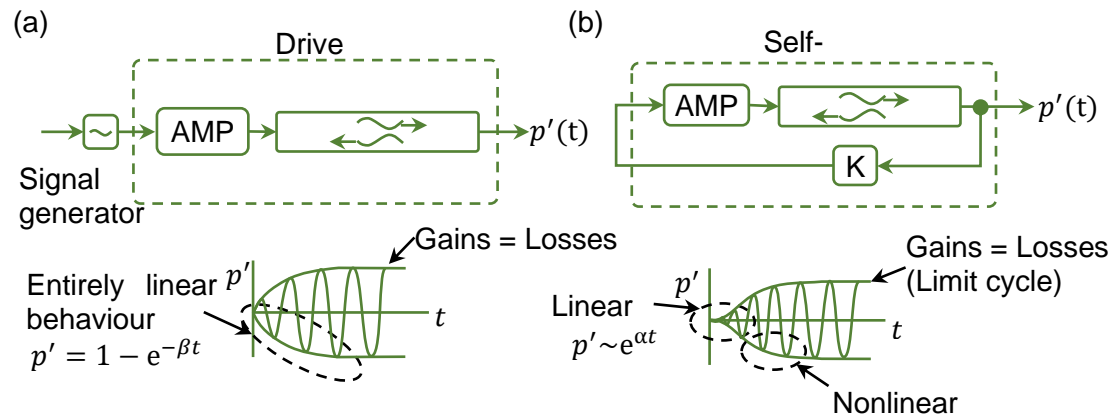


Figure 1.7: Distinct features between resonance and self-excitation. Adapted from (Culick and Kuentzmann, 2006).

1.1.4. Theoretical Modelling Approaches

1.1.4.1. Linear Stability Analysis

The amplitude of acoustic oscillations is observed to be small compared to the mean fluid dynamic variables, therefore perturbation equations of mass, momentum and energy are derived to describe the acoustic oscillations. The governing equation for acoustic oscillations is wave equation in acoustic pressure, and upon modal expansion and spatial averaging, an oscillator equation for the amplitude of a mode shape is arrived. In simplest form the equation for the amplitude $\eta(t)$ is

$$\frac{d^2\eta}{dt^2} + \omega_1^2\eta = (\gamma - 1) \int \frac{\partial \dot{Q}'}{\partial t} \psi dV \quad (1.1)$$

where $\psi(\mathbf{r})$ is spatial distribution of the pressure for the mode and the pressure fluctuation is $p' = \bar{p}\eta\psi(\mathbf{r})$. The decay/growth constant of the oscillator equation can be obtained with the knowledge of the unsteady heat release rate (\dot{Q}'). A detailed description of the stability analysis can be found in (Culick and Kuentzmann, 2006). Much of research has been carried out to obtain the unsteady heat release rate in terms of response function for different types of combustors.

$$\dot{Q}' = \frac{\dot{Q}'}{p'} \cdot p' + \frac{\dot{Q}'}{u'} \cdot u' \quad (1.2)$$

$$\dot{Q}' = R_p \cdot p' + R_u \cdot u' \quad (1.3)$$

where R_p and R_u are known as response function or Flame Transfer Function (FTF).

Fleifil & Annaswamy (1996) developed an analytical model to describe the dynamic response of laminar premixed flame stabilized to the rim of a tube to velocity oscillations. The flame front location is tracked based on the balance between flame velocity and flow velocity, an approach referred to as G-equation. The unsteady heat release is estimated from the surface area fluctuation of the flame front. The obtained unsteady heat release response function is reduced to an n- τ model. As the unsteady heat release rate is available, they went on to estimate the unstable acoustic modes based on the growth rate of the modes, which was validated against an earlier experiment. The flame response function to the velocity oscillations act as a low-pass filter, i.e. the flame response is weak for high frequency velocity oscillations.

Flame transfer function for simple flame configurations such as conical and v-flames in laminar flows were analytically derived based on linearization of G-equation

(Schuller et al., 2003). The flame dynamics is governed by two relevant parameters, a reduced frequency, and the ratio of the flame burning velocity to the mean flow velocity. The gain of the transfer function for v-flame displays amplification in a certain range of frequencies.

Bloxside et al. (1988) approximated the heat release rate as a function of forcing frequency, gutter dimension, mean free stream velocity, acoustic velocity and length of the combustor. The heat release rate model parameters are obtained from the acoustic forcing experiment. The heat release rate model is used in the perturbation equations of mass, momentum and energy and obtained the eigenfrequencies and mode shape. They reported a reasonable match between their predictions and the experimental data from Langhorne and Bloxside (1988).

Another approach involves vortex impingement against combustor wall leads to enhanced mixing and thereby sudden increase in heat release. This sudden increase in heat release is approximated as Dirac source allows good agreement between experiment and the computed pressure fields (Yu et al., 1991).

G-equation approach used in tracking the laminar flame front was extended to turbulent flames attached to bluff body (Dowling, 1999). The flame features such as flame propagating upstream, reattachment and necking (discontinuity in flame surface) were captured using the model. The nonlinear kinematic flame model with linear duct acoustics were used to estimate the self-excited oscillations. They compared results with the Langhorne and Bloxside (1988). The modelling does not include vortex shedding from bluff body which is widely observed in thermoacoustic instability with bluff bodies.

In case of turbulent flows, the velocity field of flow with the bluff bodies is obtained from experiments and then G-equation is used to compute the dynamics of the flame position theoretically (Shanbhogue et al., 2009). Shanbhogue et al. (2009) investigated bluff body stabilized flame-sheet dynamics of a harmonically excited flames, experimentally and computationally. The flame front is captured from the line-of-sight flame luminosity images, recorded using high speed imaging. The amplitude of flame front fluctuation along the length of the combustor is extracted from high-speed images for different velocity forcing amplitudes. Velocity field from PIV data is used in the G-equation to compute the flame position dynamics theoretically.

Acharya et al. (2011) conducted experiments to study the bluff body flame response to the transverse excitations. The approach is similar to that carried out for axial disturbance by (Shanbhogue et al., 2009). Repeatability of the data is better near the flame holder and is uncertain downstream. Here, experiments were conducted simulating both velocity node and antinode at the flame holder location. These two types of oscillations produced significantly different flame responses. The unsteadiness of the flame front decays after a few convective wavelengths. They attempted to fit a velocity model for the measured PIV data. Using the G-equation and the velocity model, the flame location was computed and compared with the measured flame front location.

The calculation of Eigen frequencies for a given geometry using Green function and linearized Galerkin approach can be found in Dowling (1995). A simple analytical model was proposed by Parmentier et al. (2012) to study the azimuthal instabilities in annular combustion chambers. Only pure azimuthal modes are considered and the radial

variation in acoustic parameters are neglected as the annulus width of the chamber is small compared to the diameter of the combustion chamber. The flame is assumed to be acoustically compact and FTF is used to define the response of the flame to the burner acoustic fluctuations. One, two and four burner configurations were solved analytically and stability maps were drawn for varying time delay. Then the one-dimensional model was used to solve a full annular reverse flow helicopter combustion chamber. The results were compared with results obtained from 3D Helmholtz solver (AVSP code). Considering the assumptions and simplicity of the model, good match of the estimations of the model and the 3D simulations were reported.

Linear stability analysis can be used to predict the unstable frequency and cannot predict the amplitude of the limit cycle oscillations which is a result of nonlinear processes in the system. Linear stability analysis cannot identify frequencies of triggered thermoacoustic instabilities which are result of nonlinear dynamics in the system. The nonlinear behaviour of thermoacoustic instability is discussed later in the topic of complex systems approach.

1.1.4.2. *Stochastic Process Approach*

Stochastic sources are added to the acoustic equation to account for the variations observed in the system parameters due to the effect of flow turbulence. Lieuwen & Banaszuk (2005) studied the effect of background noise on thermo-acoustic system parameters. The analysis considers the effects of fluctuations in damping rate, frequency and combustion response. It is found that the effects of noisy damping and frequency upon the combustor's stability limits is quite small and the effects of a noisy

combustion response, particularly of a fluctuating time delay between flow and heat release perturbations, can be quite significant.

Culick et al. (1992) applied time and stochastic averaging to obtain the growth rate of modes in terms of stochastic variables. The equilibrium probability density function of the pressure amplitude is derived and compared with Monte-Carlo simulations. The dimension of the attractor was estimated and discussed the possible occurrence of chaos. Similar treatment is used by Lieuwen (2003) to study the random features of the cycle-to-cycle variations of the pressure oscillations.

Noiray and Schuermans (2013b) used stochastic forcing in addition to unsteady heat release with acoustic equations. The stochastic amplitude and phase equations were derived and based on system identification, four different methods were proposed. The methods were verified with an electro-acoustic feedback experiment mimicking thermo-acoustic coupling in gas turbine combustor. The deterministic variables obtained from these methods are thermoacoustic instability frequency, growth/decay rate, combustion noise strength, and amplitude nonlinearity coefficient. Noiray & Schuermans (2013a) used stochastic acoustic equation mentioned in the preceding paper and applied to annular combustor to explain the continuously switching between standing, clockwise and counter-clockwise travelling waves. In contrast, the deterministic approach cannot predict the switching behaviour between spinning and standing oscillations.

1.1.5. Complex Systems Approach

A complex system is a system with large number of elements interacting with each other and with their environment. The interaction or the relationship between the elements of the system forms the basis of the complex system. The common characteristic of all complex systems is that they display organization without any central planning. Tools used in tackling complex systems involves three main areas: nonlinear dynamics, statistical physics, and network theory (Amaral and Ottino, 2004). Nonlinear dynamics and chaos in deterministic systems are now an integral part of science and engineering. In statistical physics, the advances in the understanding of phase transition and critical phenomenon, led to the two important concepts: scaling and universality (Stanley, 1987). Thirdly, a network is a system of nodes with connecting links. Translating a complex system into complex network helps to identify and understand hidden patterns/behaviours of the system.

Complex systems exhibit distinct behaviours such as nonlinearity, emergence, spontaneous order, adaptation, and feedback loops, etc. (Tranquillo 2019). Thermoacoustic systems exhibit behaviours of complex systems due to the interactions between acoustics, fluid dynamics and combustion (Sujith and Unni, 2020).

1.1.5.1. *Features of Self-Organization*

Self-organization is a development of some form of order/pattern from an initially disordered state. Self-organization arises out of local interaction and does not require a centralized coordination by an external agent. Self-organization is observed in various disciplines of science and technology such as biology (Camazine et al., 2001), chemistry (Mikhailov and Ertl, 2017), robotics (Murata and Kurokawa, 2012),

ecosystems (Sole and Bascompte, 2012), metallurgy (Gentili et al., 2014), electronics (Higuera-Toledano et al., 2013), economics (Leitner and Wall, 2014), astronomy and fluid dynamics (Marov and Kolesnichenko, 2013), etc.

In thermoacoustic systems, George et al. (2018) investigated the self-organizing nature of the transition from a state of combustion noise to thermoacoustic instability via intermittency. They characterized this transition i.e. from a state of disordered and incoherent dynamics to a state of ordered and coherent dynamics, as pattern formation in the turbulent combustor. They analysed the instantaneous fields of local acoustic power production using indicators of pattern formation such as spatial variance and spatial correlation. They showed from the evolution of the indicators of pattern formation, that the dynamics of the spatio-temporal coupling in the thermoacoustic system is a result of pattern formation.

1.1.5.2. *Features of Synchronization*

Synchronization theory has gained interest among the researchers of fluid dynamics. The features of synchronization are observed in fluid-structure interaction resulting in flow-induced vibrations (Gunnoo et al., 2016; Zdravkovich, 1982). The synchronous behaviour was first reported by Christiaan Huygens in his experiment involving two pendulums suspended from a common frame. He noted that the pendulums were moving in unison but in the opposite directions i.e., out of phase, regardless of how the two clocks were started. He deduced that the crucial interaction came from very small movements of the common frame supporting the two clocks. In a recent investigation, Bennett et al. (2002) re-examined the observations of Christiaan Huygens in modern experiments. They varied the coupling strength between the two clocks by the changing

the ratio of pendulum mass to system mass. They observed another state which they called as beating death, commonly known as oscillation death, in which one or both clocks cease to oscillate. Synchronization has found applications in several fields such as ecosystem (Blasius and Tönjes, 2007), chemistry (Miyazaki, 2013), climate (Read and Castrejón-Pita, 2010), varied sub-disciplines in human dynamics (linguistic (Orsucci et al., 2006); motor (Repp and Su, 2013); physiology (Glass, 2001)), pathology (Tass et al., 1998), communications (Kolumban et al., 1997), etc.

Synchronization is classified as mutual and forced synchronization based on the behaviour of frequency of the two oscillators during the transition to the locking of the oscillators (Pikovsky et al., 2001). In mutual synchronization, two self-sustained oscillators interact with each other through the coupling medium. On the other hand, in forced synchronization, the interaction is unidirectional, where one oscillator drives the other self-sustained oscillator without being affected by the self-sustained oscillator. The final frequency during locking of the oscillators is between the natural frequency of the individual oscillators in the case of mutual synchronisation and is the frequency of the driver or forcing frequency in the case of forced synchronization. In both the types, when the difference in the original frequency of the oscillators or detuning is large, the transition happens with suppression of the original frequency and emergence of the final frequency. On the other hand, when the detuning is small, the original frequencies drift towards the final frequency.

Recently, Pawar et al. (2017) applied the synchronization theory to a thermoacoustic system and showed that two non-identical oscillators of thermoacoustic system: acoustic pressure and unsteady heat release rate exhibit features of mutual

synchronization during the transition to thermoacoustic instability via intermittency. They showed that the locking frequency of the thermoacoustic system is in between the original oscillation frequencies of the acoustic pressure and the heat release rate, suggesting the mutual synchronization of the oscillators. They showed also that the transition to thermoacoustic instability exhibited synchronization features such as desynchronization, phase synchronization and generalized synchronization. Mondal et al. (2017) showed the intermittent phase locking of thermoacoustic system during the state of intermittency. In a spatiotemporal study of the intermittency, Mondal et al. (2017) showed the coexistence of regions of synchrony and asynchrony in the phasor plot of a section of a combustor. The regions of synchrony or asynchrony change with time and they related it to the breathing chimera-like state.

Thermoacoustic instability is detrimental to the combustion systems and therefore, requires suppression of thermoacoustic oscillations in the industrial applications. Interesting feature of synchronization behaviour i.e. oscillation death is a potential solution for the suppression of thermoacoustic oscillations. Biwa et al. (2015) demonstrated amplitude death in a representative thermoacoustic system by coupling two thermoacoustic oscillators. The coupling is established in two ways: dissipative coupling and time-delay coupling. The dissipative coupling is achieved by connecting the two thermoacoustic oscillators with a tube containing a needle valve. They showed that the dissipative coupling is moderately effective in achieving amplitude death in case of identical oscillators as the system adjusts to in-phase oscillations. The in-phase oscillations lead to zero pressure drop across the valve resulting in negligible acoustic losses. Therefore, the dissipative coupling requires detuning to achieve the acoustic dissipation at the valves. They showed that the amplitude death occurs more easily

when dissipative coupling is combined with time-delay coupling. The time delay is achieved by varying the length of the coupling tube. Thomas et al. (2018) generated bifurcation plots identifying conditions for amplitude death by mathematically modelling the effect of dissipative and time-delay coupling in coupled thermoacoustic oscillators i.e. Rijke tubes. In an experimental study of coupled thermoacoustic oscillators by Dange et al. (2019), they concluded that the optimum length of coupling tube required to quench the limit cycle oscillations in coupled thermoacoustic systems should be nearly equal to half the wavelength of the acoustic standing wave developed in the system and the optimum diameter should be nearly $1/10^{\text{th}}$ of the system diameter. On the other hand, in forced synchronization, Sirshendu Mondal et al. (2019) showed asynchronous quenching in a representative thermoacoustic system: Rijke tube. They showed that as the forcing frequency is fairly lower than the natural frequency of the system, nearly 80% reduction in amplitude is observed due to the phenomenon of asynchronous quenching.

1.1.5.3. *Complex Network Approach:*

Complex network is a powerful tool to study the features of complex system. The representation of a time series from complex systems as a complex network can provide a better way to visualize hidden patterns in the time series. The features of complex systems such as self-organization, multifractality, etc. are studied using the tools from nonlinear time series analysis (Eser et al., 2014; Tan et al., 2009; Zorick and Mandelkern, 2013). The presence of multiple scales, fractal behaviour etc. can be visualized in terms of connections between the nodes in the network representation. The features of the network can be characterized using the properties of the network. The network measures can be useful in quantifying the information present in the time

series. Complex network theory is used to convert the underlying dynamics in a time series into spatial structures in the complex networks. Time and spatio-temporal evolution of parameters obtained during the transition to thermoacoustic instability are converted to complex networks to study the mechanism causing thermoacoustic instability and device means to suppress the occurrence of thermoacoustic instability.

Algorithms for constructing complex networks called visibility graphs and horizontal visibility graphs, based on the visibility of nodes are presented by Lacasa et al. (2008) and Luque et al. (2009) respectively. Murugesan et al. (2014) proposed threshold grouping method to convert a time series to complex networks. They applied the method on model time series such as chaotic time series of Henon map, periodic time series, random time series and to an experimental obtained time series exhibiting intermittency. The method is able to capture the network specific properties such as scale freeness, small world effects and the presence of hubs.

Application of complex network in the dynamics of thermoacoustic oscillations reveals the existence of the power-law distribution and small-world-like behaviour in the system (Okuno et al., 2015). Murugesan et al. (2015) showed that the combustion noise is scale free using time series of acoustic pressure. They converted the time series into complex networks using visibility graph algorithm and showed that the degree distribution exhibits power-law distribution. They studied the evolution of degree distribution from combustion noise to thermoacoustic instability. The degree distribution changes from power-law distribution to a single characteristic degree during the transition from combustion noise to thermoacoustic instability. Further, Murugesan and Sujith computed the network properties such as clustering coefficient,

characteristic path length, network diameter and global efficiency for the system undergoing transition from combustion noise to thermoacoustic instability. They showed that these network properties capture the system dynamics well before the rise in pressure amplitude levels in the combustor. They suggested that these network properties can be used as early warning signals to detect the onset of impending thermoacoustic instabilities. Extending the work of Murugesan and Sujith, Godavarthi et al. (2017) constructed the topology of complex networks and computed the network properties with networks constructed from recurrence matrix. They studied the topology of the complex network and network properties of the system dynamics transitioning through combustion noise, intermittency before thermoacoustic instability, thermoacoustic instability, intermittency after thermoacoustic instability and lean blow out. They showed that the network properties are different for time series corresponding to combustion noise, dynamics before lean blow out, and white noise. They concluded that the properties of the network constructed from recurrence matrix can be used as an early warning measure for predicting impending thermoacoustic instability as well as blow out.

The location of critical regions in a thermoacoustic system can help in devising optimal control strategies to mitigate thermoacoustic instability. Unni et al. (2018) identified critical region of the reactive flow field during the transition from stable operation to thermoacoustic instability via intermittency. They constructed a network from the velocity field of the reactive flow using Pearson correlation coefficient. They found using network centrality measures, that the bluff body wake is the critical region during combustion noise and the critical region shifts to top of the bluff body as the system transitions to thermoacoustic instability through intermittency.

Krishnan et al. (2019) showed that the production of acoustic power happens in a spatially incoherent manner for combustion noise and in contrast, happens in a spatially coherent manner for thermoacoustic instability. In the transition from combustion noise to thermoacoustic instability via intermittency, the spatial pattern of the acoustic power transitions from the incoherence to the coherence through nucleation, coalescence and increase in size to form large clusters. They showed the occurrence of this phenomenon using network measures such as the link density, the number of components and the size of the largest component to quantify the spatiotemporal dynamics of acoustic power sources in a turbulent combustor.

Introduction of micro-jets into the sources of thermoacoustic instability is a potential method in the suppression of the instability (Murat Altay et al., 2010; Uhm and Acharya, 2004; Zhou et al., 2020). Murayama & Gotoda (2019) studied the effect of micro-jets in the suppression of thermoacoustic instability using tools from complex network and synchronization theories. They conducted experiments in a swirl stabilized combustor with a steady injection of secondary air. They showed that synchronization index captures the attenuation of mutual coupling between the acoustic pressure and the unsteady heat release rate. Krishnan et al. (2019) presented a novel method using micro-jets to mitigate thermoacoustic instability. They identified the critical regions using complex network theory and targeted the critical regions with the micro-jets to suppress the thermoacoustic instability. They constructed weighted spatial correlation networks from the velocity field obtained from high-speed PIV. Then they used three network measures strength of a node, weighted clustering coefficient and weighted closeness centrality to identify the critical region. They conducted thermoacoustic experiments with micro-jets positioned in the combustor targeting various regions of

the combustor. They showed that the micro-jets targeting the critical regions are able to mitigate thermoacoustic instability in the combustor.

1.1.5.4. *Features of Nonlinearity*

Linear system satisfies the property of homogeneity and additivity. In a linear system, when an input is multiplied by a factor produces an output with the same factor multiplied, and the property is known as homogeneity. Likewise, sum of two input signal supplied to a linear system produces an output which is sum of the corresponding output signals, and the property is known as additivity. Linear systems are relatively easier to analyse mathematically. A system that fails in satisfying one or both the properties is called as nonlinear system. Despite the tractability of linear approach, most real-world systems are nonlinear.

Nonlinear behaviour is observed in thermoacoustic system and is evident from the occurrence of limit cycle oscillations. As the oscillations grow exponentially to high amplitudes, the nonlinearities in relevant processes of the system become significant, resulting in a balance between the acoustic power production and the acoustic damping or losses in the system. This balance leads to saturation of amplitude of the oscillations known as limit cycle oscillations (Culick and Kuentzmann, 2006). Thermoacoustic system comprising laminar flame combustor, exhibits features of nonlinear dynamics such as periodic, quasi-periodic, frequency locked, period-2, and chaotic oscillations in the time series of pressure (Kabiraj et al., 2012). The nonlinear behaviour of the thermoacoustic system is dominantly due to the nonlinearities in the combustion process and its interaction with acoustics (Dowling, 1997).

Subcritical Hopf bifurcation is a characteristic feature of nonlinear process in the system. Subcritical Hopf bifurcation contains a bistable zone wherein two stable states coexist i.e. a steady state and an oscillatory state as shown in Figure 1.8 (Strogatz, 2018). The bistable zone of the bifurcation leads to phenomenon such as triggering and hysteresis. Triggering is a phenomenon of requiring a finite amplitude of perturbation to transition the system dynamics from steady state to oscillatory state. Subcritical bifurcation is shown to occur in thermoacoustic systems. Hysteresis is the different dynamical trajectory taken by the system during the reverse transition i.e. from oscillatory state to steady state. The subcritical Hopf bifurcation is observed clearly in a prototypical thermoacoustic system, a horizontal Rijke tube (Gopalakrishnan and other Rijke tube papers from his reference).

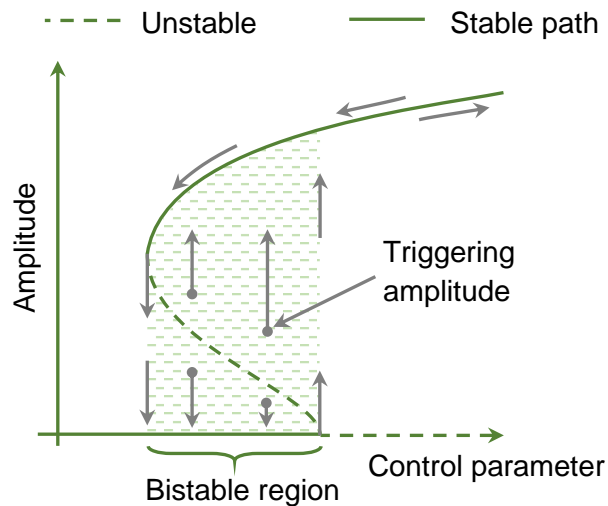


Figure 1.8 : Subcritical Hopf bifurcation.

Gotoda et al. (2014) proposed an online method of detecting thermoacoustic instability occurring prior to lean blowout in a premixed gas-turbine model combustor. They showed that the translation error, which is characterized by quantifying the degree of parallelism of trajectories in the phase space, can be used as a control variable to prevent lean blowout.

Gotoda et al. (2012) characterized the dynamics of thermoacoustic instability near lean blowout in a lean premixed gas-turbine model combustor using nonlinear time series analysis. They showed that the dynamic behaviour of thermoacoustic instability near lean blowout exhibits a self-affine structure and is ascribed to fractional Brownian motion. They suggested that the nonlinear time series analysis is capable of characterizing complexities in thermoacoustic instability prior to lean blowout. Nair & Sujith (2014b) applied multifractal theory to predict an impending thermoacoustic instability. They demonstrated with experimental results that measures such as Hurst exponent can act as early warning signals to impending instability. Combustion noise is a deterministic noise resulting from the nonlinear interaction between turbulence, combustion and chamber acoustics.

1.1.5.4.1. Intermittency

One of the characteristic nonlinear dynamical states observed during the transition to thermoacoustic instability is intermittency (Domen et al., 2015; Ebi, Doll, et al., 2018; Ebi, Denisov, et al., 2018; Gotoda et al., 2014, 2017; Karlis et al., 2019; Kheirkhah et al., 2016; Nair et al., 2013, 2014a; Nair and Sujith, 2014a; Pawar et al., 2015, 2017; Pawar and Sujith, 2018a, 2018b; Unni et al., 2018; Unni and Sujith, 2017; Wilhite et al., 2016). Intermittency occurs as bursts of high-amplitude periodic oscillations occurring at irregular intervals amidst low-amplitude aperiodic oscillations. Kabiraj & Sujith (2012) observed bursts of chaotic oscillations of acoustic pressure in a laboratory laminar combustor and related the observation with the phenomenon ‘intermittency’ from literature of nonlinear dynamics. Nair et al. (2014a) observed that intermittency presages the state of limit-cycle oscillation in two turbulent combustors with flame stabilization mechanisms such as bluff body stabilized and swirl stabilized. In their

study, the transition to thermoacoustic instability from combustion noise occurs by increasing the Reynolds number in a quasi-static manner. They quantified the intermittency route to limit cycle oscillations using recurrence quantification analysis and showed that the recurrence quantification measures can be used as precursors to an impending thermoacoustic instability.

Ebi et al. (2018) showed in a swirl stabilized combustor that the transition to thermoacoustic instability happens through intermittency with increasing equivalence ratio. They explained that the occurrence of subcritical bifurcation and the saturation of the amplitude of acoustic pressure is a result of a drift of phase between heat release rate and acoustic pressure oscillations as function of amplitude of acoustic pressure rather than the balance between gain of flame transfer function and acoustic damping. Ebi et al. (2018) studied the dynamics of flow field and the flame during intermittency of a swirl stabilized combustor. From the OH PLIF images of the flame, they concluded that the burning area fluctuations is the physical mechanism causing the heat release rate oscillations. They observed also that the flame is attached to the centre body throughout the intermittent oscillations of acoustic pressure. Karlis et al. (2019) examined the thermoacoustic characteristics of hydrogen-enriched methane blends in a swirl-stabilized model gas turbine combustor. They conducted experiments by increasing the hydrogen concentration in the methane blend maintaining the global equivalence ratio and repeated it for three different equivalence ratios. From those experiments, they showed that the amplitude of pressure oscillations obtained during the dynamic transitions from quiescent state to limit cycle oscillations through intermittent bursts of oscillations, collapses to a curve representative of subcritical bifurcation when plotted against the extinction strain rate. Pawar & Sujith (2018b) have

provided a review of the recent developments in the understanding of transition to thermoacoustic instability through intermittency.

1.1.5.4.2. Rate dependent transition

Another nonlinear dynamical aspect of recent interest in thermoacoustic instability is rate induced tipping or R tipping. Wieczorek et al. (2011) and Ashwin et al. (2012) identified R-tipping in a model of the climate system. They showed that beyond a critical rate of change of control parameter, the system tips at a value of control parameter which does not correspond to a quasi-static bifurcation or noise-induced bifurcation. The presence of noise in the system lowers the critical rate of change of control parameter corresponding to R-tipping (Mannella et al., 1987). Tipping gets delayed or occurs earlier depending on the system, by varying the control parameter with time (Baer et al., 1989; Bonciolini et al., 2018, 2019; Majumdar et al., 2013; Mandel and Erneux, 1984, 1987). Recently, Tony et al. (2017) showed the occurrence of preconditioned rate induced tipping in a Rijke tube, a prototypical thermoacoustic system. Heydarlaki et al. (2019) studied the changes in the dynamical states of a combustion chamber during transient increase in the combustor wall temperature for a given operating condition. Similarly, in a micro combustor, Li et al. (2009) observed buzzing and whistling sound while operating the combustor under cold wall conditions, and on the contrary, the thermoacoustic instability is avoided by operating the micro combustor under hot wall conditions.

1.2. INTERIM SUMMARY AND MOTIVATION

Bluff body flame holders are used in ramjets and afterburners to stabilize flame in the high-speed air stream. These combustors typically use liquid fuel injection, and the inlet

temperature to afterburners is high as they are used at the exhaust of the gas turbines. These combustion systems are prone to transverse mode thermoacoustic instability. On the other hand, lean-burn swirl stabilized combustors are used in industrial gas turbines to satisfy the requirements of emission norms. Several investigations are reported in literature on the lean-burn swirl stabilized combustors due to its susceptibility to thermoacoustic instability. There is no thermoacoustic study in the literature particularly self-excited experiments, simulating a typical afterburner involving high inlet temperatures, liquid fuel injection, and flow Reynolds number typical of afterburner. The existing countable articles on the subject pertains to 1950s (Elias, 1959; Rogers and Marble, 1956) and hardly any literature is available in the recent decades on the self-excited transverse thermoacoustic instability with bluff body stabilized flames. Recently, interesting developments have happened in the understanding of the transition of combustors from the state of combustion noise to the state of thermoacoustic instability with the subject being looked at from the perspective of nonlinear dynamical systems and complex systems approach (Sujith and Unni, 2020).

Ashwin et al. (2012) and Wieczorek et al. (2011) identified Rate-dependent tipping or R-tipping in a theoretical model of the climate system. They showed the existence of a critical rate of change of control parameter beyond which the system tips. They showed also that the value of control parameter corresponding to R-tipping, does not correspond to a quasi-static bifurcation or noise-induced bifurcation. In the context of afterburners, military gas turbine engines are designed to respond faster, in order to quickly achieve the maximum thrust. This requirement leads to a higher rate of change of inlet parameters to the gas turbine combustion systems. Then the question to be answered is,

will R-tipping occur in combustion systems of gas turbine engines? If R-tipping occurs, will the tipping follow the intermittency route to thermoacoustic instability?

Intermittency is reported to occur in laboratory combustors with gaseous fuel injection and with inlet air at room temperature (Nair et al., 2014b; Pawar et al., 2015). Will intermittency occur in highly turbulent combustors such as the present model afterburner with liquid fuel injection and elevated air temperature at the inlet of the model afterburner? What happens to the coupling strength and phase relationship between the p' and \dot{q}' during the transition to thermoacoustic instability through intermittency?

Vortex shedding from bluff bodies are shown to be a mechanism causing transverse mode thermoacoustic instability. In acoustically forced experiments, the wrinkling/roll-up of flame in the vortex is assumed to be the reason for increase in the amplitude of unsteady heat release rate (Shin et al., 2011). There is no conclusive spatial analysis available in literature on the vortex shedding dynamics during transverse mode thermoacoustic instability that is meant to understand the spatial region responsible for the generation of acoustic power. So, the succeeding question is what regions are responsible for the generation of acoustic power for a vortex shedding mechanism from a bluff body stabilized flames? In the present work, we attempt to answer these related to transverse mode thermoacoustic instability.

1.3. OBJECTIVE OF THIS THESIS

The aim of the present thesis is to study the transition of a model afterburner from the state of combustion noise to the state of self-excited, transverse mode, thermoacoustic

instability. Secondly, to study the mechanism causing the transverse mode thermoacoustic instability in a model afterburner.

1. We identify an experimental afterburner configuration that operates in a state of transverse mode thermoacoustic instability. We obtain a screeching afterburner by studying different flame holder and fuel injector configurations. The flame holder parameters such as width and number; and the fuel injector parameters such as orifice size, orientation of the jet with respect to flow direction, and number of orifices will be studied.
2. We study the rate-dependent transition of the model afterburner from the state of combustion noise to the state of transverse mode thermoacoustic instability. We characterize the state of intermittency observed during the rate dependent transition by analysing the time series of acoustic pressure. We study the operating conditions of the afterburner during the onset of transverse mode thermoacoustic instability.
3. We study the coupled interaction between p' and \dot{q}' using measurements of global unsteady heat release rate and acoustic pressure. We investigate the coupling strength between the oscillators by computing wavelet coherence and cross-correlation coefficient between probability of recurrence of p' and \dot{q}' . We characterize different dynamical states of the coupled interaction using tools from synchronization studies of thermoacoustic instability.
4. We capture the flame dynamics during transverse mode thermoacoustic instability using planar measurements of unsteady heat release rate using OH* chemiluminescence. We identify the regions of sources and dampers of acoustic power by plotting the Rayleigh index of the imaged field. We analyse

the phasor plot obtained between p' and \dot{q}' , and study the mechanism behind the formation of pattern in the phasor field.

1.4. OVERVIEW OF THIS THESIS

We conducted experiments in a model afterburner to address the questions raised in the motivation section of the thesis and the objectives planned in the thesis. In **Chapter 2**, we describe the experimental setup of a model afterburner, air supply facility, controls for studying rate dependent transition, and instrumentation. The air supply facility uses a kerosene burner to simulate the elevated inlet temperature of the afterburner. We also describe the experimental procedure to operate the kerosene burner (pre-heater) and the model afterburner from ignition to the final operating conditions of a given experiment.

We describe in **Chapter 3**, the observation of rate dependent transition to transverse thermoacoustic instability via intermittency in the model afterburner intermittency, with respect to increasing rate of change of Reynolds number. The onset of burst occurs earlier, i.e., bursts occurring at a lower Reynolds number as the rate of change of Reynolds number is increased. The amplitude of bursts during intermittency is higher than that of the limit cycle oscillations. We characterize the rate dependent transition to thermoacoustic instability using phase space reconstruction and recurrence plots.

We obtained the global unsteady heat release rate using photomultiplier tube and high-speed imaging of the flame dynamics at the wake of the flame holder during thermoacoustic instability. In **Chapter 4**, we study the coupled interaction between acoustic pressure and global unsteady heat release rate using tools from synchronization theory such as wavelet coherence, probability of recurrence and cross correlation of

probability of recurrence. We observe that the coupling between p' and \dot{q}' itself transition from the state of no coupling during combustion noise to state of strong coupling during thermoacoustic instability through intermittent coupling with increasing coherence in the alignment of phasors. The cross correlation of probability of recurrence shows a steep rise during the transition indicating a change in the coupling strength from weak to strong coupling. The CPR suggests a locking behaviour after the transition to strong coupling, irrespective of variations in the p'_{rms} .

We observe in the high-speed images that the flame in the wakes of the top and bottom flame holders roll-up periodically in asymmetric manner. The air streams between the flame holders respond as jets to the acoustic velocity perturbations and flap in/out of the adjacent wakes. We compute the Rayleigh index and show that though the mechanism is vortex shedding, the vortex roll-up itself does not generate acoustic energy. We compute the propagation velocity of the intensity fluctuations and show that the pattern observed in the phasor plot is due to the propagation time taken by the intensity fluctuations to reach different regions from the wake of the flame holders.

We conclude in **Chapter 5**, based on the findings in the present thesis. We bring out the possible implications of the rate dependent transition to thermoacoustic instability in the testing and operation of a gas turbine combustion system. In our spatio-temporal analysis of flame dynamics, we conclude that the suppression techniques devised for disrupting the acoustic sources, cannot be misled by the vortex-flame roll up and requires a thorough investigation before implementing such techniques.

CHAPTER 2

EXPERIMENTAL SETUP AND INSTRUMENTATION

2.1. EXPERIMENTAL SETUP

We established an experimental afterburner facility simulating typical gas-turbine afterburner operating conditions for studying the transition to thermoacoustic instability. The air supply to the afterburner rig is from a pressurized air reservoir acting as a blow-down supply. The air from the reservoir passes through air filter, pressure regulator, globe valve, thermal mass flow meter, kerosene burner (preheater), and plenum to reach the afterburner as shown in Figure 2.1, in the same order. The pressure regulator maintains a constant downstream pressure, as the reservoir pressure decreases while discharging the air. Then the remotely operated globe valve is adjusted to maintain the preheater pressure to a required value.

The preheater is used to simulate the hot gas condition at the inlet of the experimental setup. The preheater burns kerosene and can raise the air temperature up to 1200 K at the inlet to the afterburner. The kerosene supply for both the preheater and the afterburner is from a fuel tank which is pressurized with high pressure nitrogen. The preheater has an exhaust nozzle which is choked and controls the mass flow rate to the afterburner. For the required air mass flow rate range of 0.3 – 0.45 kg/s, the operating pressure range of the preheater is varied between 3 and 3.7 bar. Nevertheless, the afterburner operates between 1.2 and 1.3 bar, depending on the amount of heat addition in the afterburner. As the mass flow rate is controlled by the choked nozzle at the

preheater exit, the mass flow rate through the model afterburner is not altered by the amount of heat addition in it.

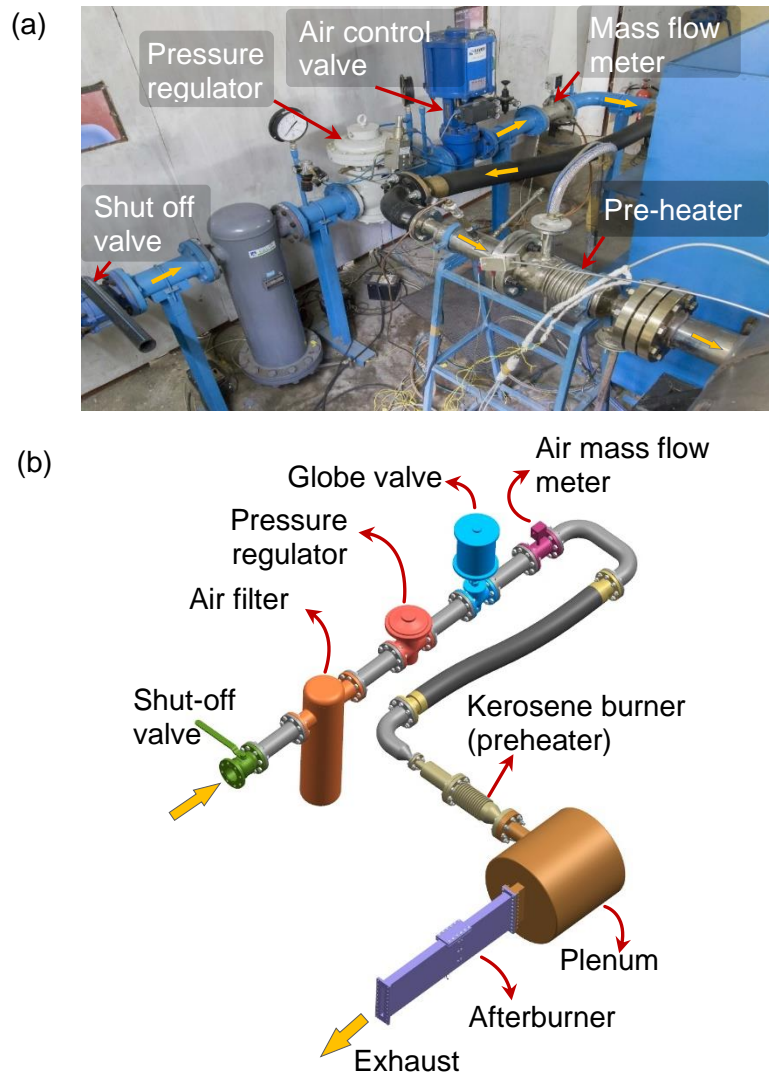


Figure 2.1: (a) Picture of air supply facility which can simulate afterburner inlet conditions. (b) Schematic of the air supply facility. The air supply facility is a blow-down facility with a kerosene burner (preheater) connected upstream of the afterburner through a plenum.

2.2. AFTERBURNER GEOMETRY

The afterburner is a constant area, rectangular duct with flow path dimensions of $240 \times 25 \times 1,200 \text{ mm}^3$. The fuel injectors and the trailing edge of the flame holders are located axially at 450 and 585 mm, respectively, from the inlet of the afterburner as

shown in Figure 2.2. Three flame holders are distributed along the height with equal distance between them. Three fuel tubes and three spark plugs are positioned in-line with the flame holders. The fuel tubes spray fuel to the respective flame holders and the corresponding spark plug ignites the fuel-air mixture. Each of the fuel tubes contains four plain orifice injectors of 0.5 mm diameter, oriented in the transverse direction with respect to the air flow. The air flow enters the afterburner through the plenum, which acts as a de-coupler to maintain an open acoustic boundary ($p' = 0$). The plenum is a constant-area circular duct with a diameter of 600 mm and a length of 600 mm. The other end of the afterburner is open to the atmosphere, simulating an acoustically open-open boundary condition.

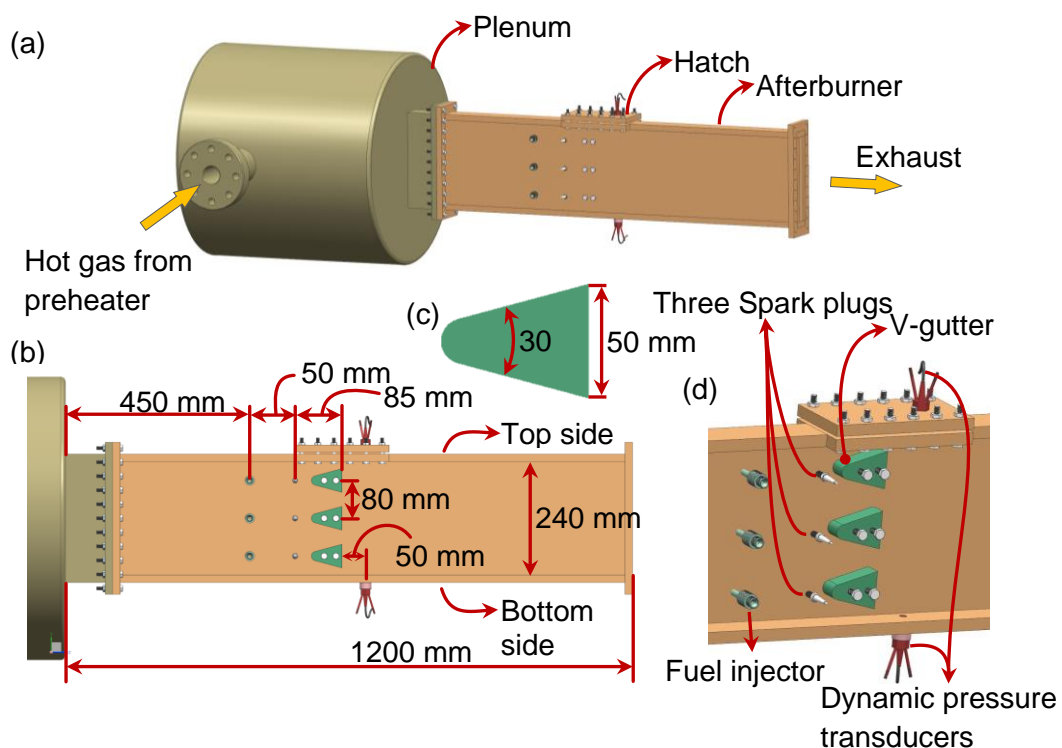


Figure 2.2: (a) The schematic of the afterburner used in the present study. (b) The afterburner contains three sets of flame holder, fuel injector and spark plug, and are arranged as shown. (c) Dimensions of the flame holder. (d) Zoomed-in view of the flame holder, fuel injector, spark plug, and dynamic pressure transducer.

We designed another test section with optical access (quartz glass) on one side of the test section for recording the flame dynamics using high-speed camera and global unsteady heat release rate using PMT. The optical window covers the full test section height with a window size of 240 x 240 mm. The test section with optical access is shown in Figure 2.3.

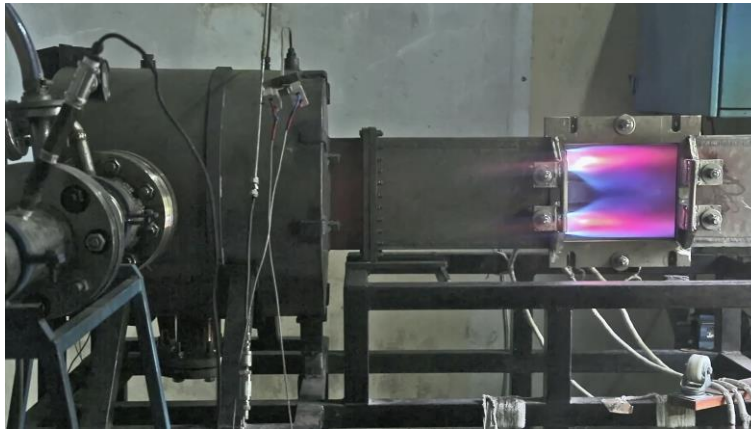


Figure 2.3 : Test section with optical access on one side of the test section covering full test-section height.

2.2.1. Other geometries experimented to obtain transverse thermoacoustic instability

Initially, we designed the test section with optical access for regions corresponding to flame location, fuel injection and spray atomization. Such an arrangement required side plates of the test section to be fixed using flanges with bolt-nut fittings as shown in Figure 2.4. We have experimented with different flame holder and fuel injector arrangement such as number of fuel injectors, fuel injector orientation, flame holder width and number of flame holders, in order to identify the configuration which can screech. Later, we realized that it is the high acoustic damping of the setup which adversely affected the onset of transverse thermoacoustic instability. Therefore, we

fabricated the test section used for the present study as a single piece with all the sides welded together as depicted in Figure 2.2.

We measured the exponential decay rate under no flow and room temperature condition with help of two loud speakers as sound source positioned at the exit of the test section. We excited the loud speaks using an amplifier with signal from oscilloscope. First, we excited the speakers with random noise signal and recorded the acoustic response of the test section using microphone at one of the provisions for transducers. The acquired time series is transformed to frequency domain to identify the dominant mode of the test section. Next, we excited the speakers with sinusoidal signal pertaining to the dominant frequency and monitor the acoustic response for pressure oscillations with constant amplitude. Once the constant amplitude pressure oscillations are set in the test section, we abruptly turned off the input signal to the oscilloscope and recorded the exponential decay of the amplitude of pressure oscillations in the test section. The preceding steps are repeated several times to obtain an averaged decay rate. The exponential decay rate of test section with many flanged joints (refer Figure 2.4) is 59 s^{-1} and for the fully welded test section (refer Figure 2.2), it is 25 s^{-1} which is 58% lower than the test section with many flanges. We observed transverse thermoacoustic instability in the fully welded test section which we used for studying rate-dependent transition to thermoacoustic instability.

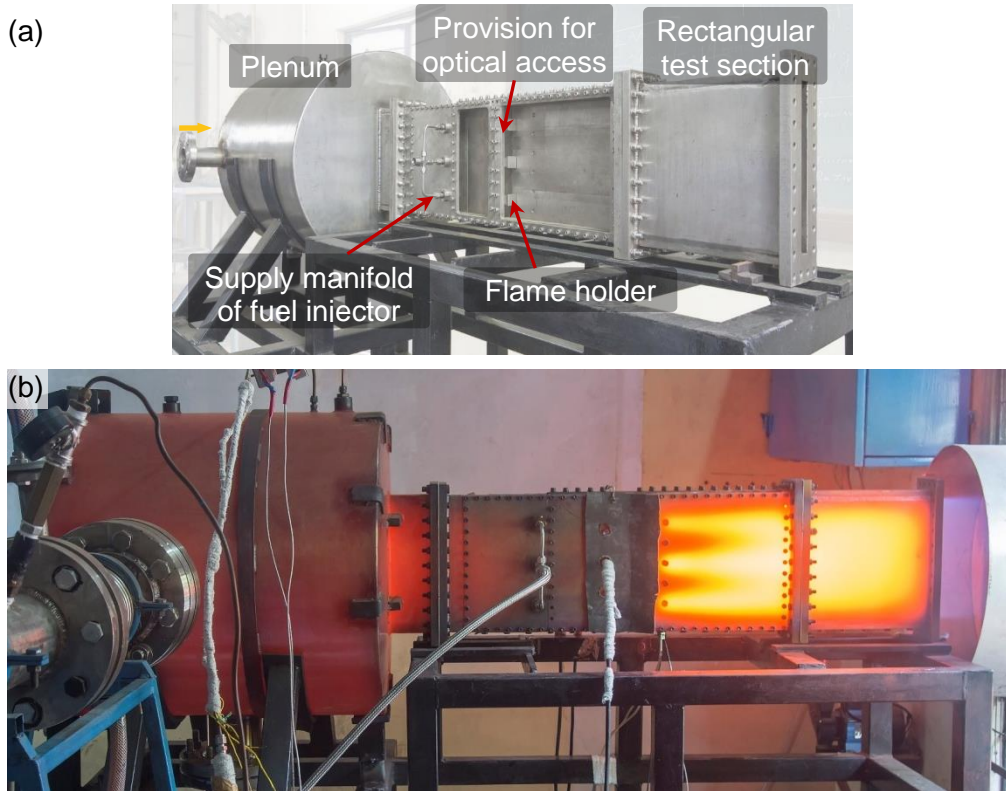


Figure 2.4 : (a) Initial test section with flanged side plates did not encounter transverse thermoacoustic instability. (b) Picture of test section with many flanges during afterburning with three-flame-holder configuration. The red-hot appearance in the picture is due to metal heating by the flame inside the test section.

2.3. CONTROLS FOR THE STUDY OF RATE-DEPENDENT TRANSITION

We needed to open the valve using a computer in order to open the valve at a desired constant rate. We created a LabView program with graphical interface such that the valve opening can be changed as desired using a slider option or set a rate of valve opening upto a threshold valve. The results of the program though generated a constant-rate of change of valve opening but did not have constant-rate of change of air flow rate, refer Figure 2.5. Therefore, We calibrated the valve for air flow rate against valve opening. The calibration table is build into the program in order to maintain a constant air flow rate.

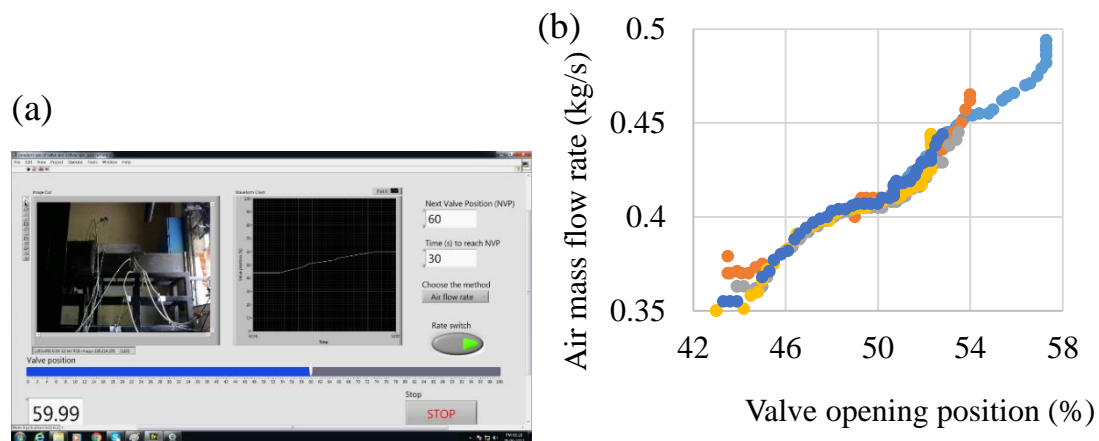


Figure 2.5 : (a) LabView interface. (b) calibration curve for air flow rate vs valve opening for the globe valve. The plotted curves are obtained over multiple trials of valve opening.

2.4. INSTRUMENTATION

The mass flow rate through the experimental setup is measured using Sierra Instruments Flat-Trak model 780s mass flow meter. The range of mass flow meter is up to 1 kg/s with an accuracy of $\pm 1\%$ of the reading and a repeatability of $\pm 0.2\%$ FSR (Full Scale Reading). The fuel (kerosene) mass flow rate to the preheater and the afterburner were measured using Broil oval gear flow meter with a range of 0 – 60 lph and 0 – 120 lph, respectively, with an accuracy of $\pm 0.5\%$ of the reading. The inlet pressure and temperature to the afterburner are measured in the plenum using a static pressure transducer: Omega-PX329-050AV, and K-type thermocouple, respectively. The range of static pressure transducer is 0 – 3.5 bar (absolute) with an accuracy of 0.25% BFLS (Best Fit Straight Line). Two dynamic pressure transducers, to measure acoustic pressure, are installed flush mount on top and bottom sides of the afterburner at 50 mm downstream of the flame holders as shown in Figure 2.2b. The acoustic pressure transducer used is Kulite EWCTV 312M (water cooled) with a range of 0 – 50 psi (absolute), an accuracy of $\pm 0.1\%$ FSR BFLS, a bandwidth of 30 kHz and a repeatability of $\pm 0.5\%$ FSR (max.).

We captured flame dynamics using high-speed imaging of OH* radicals in the flame region which is shown in Figure 2.6. We acquired data only from transducer 1 (refer Figure 2.6) during the high-speed imaging. A high-speed CMOS camera (Phantom V 12.1) is used to capture the OH* chemiluminescence radiated by the reacting mixture. The camera is fitted with a Carl Zeiss lens of 50 mm focal length and an aperture of $f/2.0$. A bandpass optical filter from Opto Lamallae having a centre wavelength of 308 nm ($10\pm$ nm FWHM) is mounted in front of the lens to capture only the radiation from OH* radicals. The high-speed camera captures a region of 160 x 160 mm², with a resolution of 640 pixels x 640 pixels, at a frame rate of 14,000 fps, and with an exposure time of 70 μ s. A photomultiplier tube (PMT) module fitted with an OH* filter with a centre wavelength of 308 nm and 12 nm FWHM, captures the global unsteady heat release rate (\dot{q}'). The PMT module has a field of view of 70 degrees which encompasses half of the optical window as shown in Figure 2.6. The analog voltage signal from the pressure transducer and PMT is sampled using National Instruments (NI 9220), 16-bit analog to digital converter with a maximum of 100 kHz sampling rate per channel.

2.4.1. Location of pressure transducers in the test section

We measured the acoustic field set up upstream of the flame holder in the constant area test section. We have installed seven pressure transducers upstream of flame holder (numbered as 2 to 8 in Figure 2.6), at the bottom side of the test section, starting from the leading edge of the flame holder. The pressure transducers upstream of flame holder are installed with a spacing of 50mm between them, measuring acoustic pressure up to a distance of 300mm from the leading edge of flame holder, in the upstream direction. One pressure transducer is installed on the top side of the test section (numbered as 9

in Figure 2.6) and upstream of the flame holder. Two more pressure transducers are installed downstream of flame holder one at the top and the other at the bottom side located 50mm downstream of trailing edge of flame holder (numbered as 1 and 10 in Figure 2.6). In the study of rate dependent transition, only transducer 1 is used to acquire pressure in the test section. Apart from the measurement of acoustic pressure, we captured flame dynamics using high-speed imaging of OH* radicals in the flame region and global unsteady heat release rate using PMT. The regions of imaging are marked in Figure 2.6.

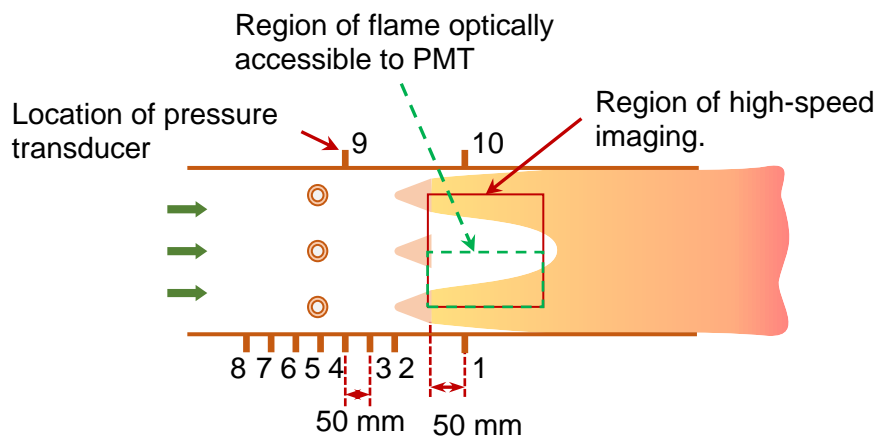


Figure 2.6: Locations of the pressure transducers, region of high-speed imaging and region accessible to PMT are shown in the schematic of the model afterburner.

2.5. EXPERIMENTAL PROCEDURE

At the start of the experiment, we open the valves to allow a small quantity of air to pass through the preheater along with LPG and kerosene fuel. Then we power a spark plug which ignites the LPG-air mixture, in turn, lighting up the kerosene-air mixture. The spark plug is powered by 15kV/500 W continuous supply ignition transformer. A few seconds later, we shut-off the LPG supply using a solenoid valve. As the kerosene-air mixture is ignited, we increase the air flow rate and the kerosene flow rate to 0.2 kg/s

and 22 lph ($\phi_{ph} = 0.36$), respectively. The preheater flame is stable for air flow rates higher than 0.2 kg/s, for which air flow rates, the nozzle of the preheater is choked.

After 5 minutes of settling time, we ignite the afterburner using two spark plugs that are close to the top and bottom sides of the setup, refer to Figure 2.2. Those two spark plugs ignite the fuel-air mixture in the wakes of respective flame holders. We do not ignite the fuel-air mixture in the wake of the middle flame holder as screech is observed only with flames sustained by the top and bottom flame holders, and in the presence of the middle flame holder without sustaining flame. The afterburner is ignited at an air and fuel flow rates of 0.28 kg/s and 25 lph ($\phi_{ab} = 0.55$), respectively. Once the afterburner ignites, we set the fuel flow rate of the preheater and the afterburner to a given experimental setting and keep it constant. After this, we increase the air flow rate at an approximately constant rate using a computer-controlled valve up to 0.45 kg/s to study the rate dependent transition in thermoacoustic instability.

We vary the air flow rate approximately in a linear manner by the following procedure. We operate a globe valve to maintain the operating pressure of the preheater. The air flow rate through the preheater is calibrated against the percentage opening of the valve for a constant fuel flow rate to the preheater and with combustion in the preheater. Then a profile of valve opening is arrived based on the calibration data for a given fuel flow rate of interest, in order to achieve a linear variation of air flow rate with time. The pre-determined profile of valve opening is maintained through LabView software from the computer.

CHAPTER 3

RATE DEPENDENT TRANSITION TO THERMOACOUSTIC INSTABILITY VIA INTERMITTENCY

Gas turbine engines for military applications are designed to respond faster, in order to quickly achieve the maximum thrust. This requirement leads to a higher rate of change of inlet parameters to the gas turbine combustion systems. Then the question to be answered is, will R-tipping occur in turbulent combustors similar to those used in aircraft gas turbine engines? If R-tipping occurs, will the tipping follow the intermittency route to thermoacoustic instability? We present here experimental evidence of R-tipping in turbulent combustion system of a typical gas turbine afterburner. We conducted R-tipping experiments in the afterburner by varying the rate of change of air flow rate, in turn varying the rate of change of Reynolds number. For the quasi-static change of Reynolds number, the system does not transition to thermoacoustic instability and remains in the state of combustion noise. By increasing the Reynolds number at higher rate and maintaining all other operating conditions of the afterburner same, the system tips to thermoacoustic instability. We show for the first time that the transition to thermoacoustic instability happens via intermittency depending on the rate of change of control parameter.

In our experiments, as We increased the Reynolds number to 74,400 at a certain rate with the flame sustained in the afterburner, we observed the excitation of transverse

mode thermoacoustic instability in the afterburner. While increasing the Reynolds number, we fixed the fuel flow rate of the preheater and the afterburner to 26 lph and 46 lph, respectively. The equivalence ratio of the afterburner at the onset of screech (ϕ_s) is 0.65. The dominant frequency in the amplitude spectrum of pressure fluctuations is 1,434 Hz with spectral amplitude of 7,007 Pa, as shown in Figure 3.1a. The pressure fluctuations are measured using the dynamic pressure transducer and sampled at 50 kHz. The amplitude spectrum of the pressure fluctuations is estimated with 10,000 samples providing a frequency resolution of 6 Hz. The phase difference between the pressure signals from the two pressure transducers installed on the top and the bottom sides of the afterburner (Figure 2.2) is nearly 165° (i.e. close to 180°). The phase difference is obtained based on the maximum cross correlation between the two pressure signals as shown in Figure 3.1b. The observed thermoacoustic instability is identified as the first transverse mode and has a dominant oscillation frequency of 1434 Hz, which is generally known as screech.

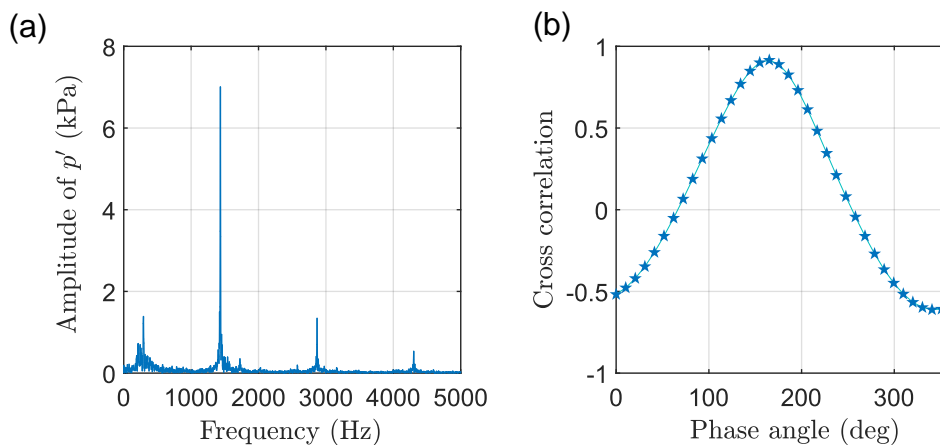


Figure 3.1 : (a) The amplitude spectrum of pressure fluctuations (b) Cross correlation of the pressure signals obtained from the top and the bottom sides of the rectangular afterburner.

3.1. RATE INDUCED TIPPING OF SCREECH

In the afterburner, we increased the Reynolds number from 72,500 to 97,700 in 350 s as shown in Figure 3.2a, maintaining a constant fuel flow rate of 22 lph to the preheater and 41 lph to the afterburner. We did not observe screech. On the contrary, when we increased the Reynolds number faster, i.e., from 70,600 to 86,300 in 13.6 s with the same fuel flow rates, we observed screech as shown in Figure 3.2b. The average rates of change of Reynolds number (\dot{Re}_{avg}) for the mentioned experiments correspond to 121.5 s^{-1} and $1,143.1 \text{ s}^{-1}$. The average rate of change of Reynolds number is calculated as $\dot{Re}_{avg} = (Re_{\dot{m}_a=0.42} - Re_{\dot{m}_a=0.34}) / (t_{\dot{m}_a=0.42} - t_{\dot{m}_a=0.34})$, where t is time (s); the air mass flow rate between 0.34 kg/s and 0.42 kg/s is increased at constant rate approximately. The afterburner becomes thermoacoustically unstable depending on the rate of change of Reynolds number, even if the afterburner is quasi-statically stable (slow change of Reynolds number). This phenomenon is known as rate dependent transition (also known as rate induced tipping or R-tipping).

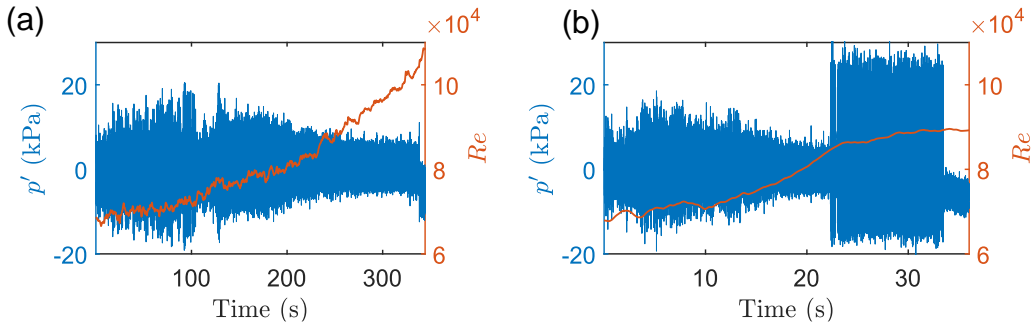


Figure 3.2 : The plot of acoustic pressure and the Reynolds number corresponding to the rate of change of Reynolds number (\dot{Re}_{avg}) of (a) 121.5 s^{-1} (screech did not occur), and (b) $1,143.1 \text{ s}^{-1}$ (screech occurred). The fuel flow rate of the preheater and the afterburner for this experiment is 22 lph and 41 lph, respectively.

3.2. RATE DEPENDENT TRANSITION OF SCREECH VIA INTERMITTENCY

We show for the first time that the rate dependent transition to screech in afterburner happening through intermittency. We conducted experiments with different rates of change of Reynolds number, while maintaining constant fuel flow rates to the preheater of 29 lph and the afterburner of 41 lph. In Figure 3.3, we show the time series of acoustic pressure obtained from these experiments, wherein the plots are arranged with increasing rate of change of Reynolds number. At a slow change of Reynolds number ($\dot{Re}_{avg} = 102.9 \text{ s}^{-1}$), shown in Figure 3.3a, we notice the occurrence of a few bursts at lower Reynolds numbers, and a sustained periodic oscillation at higher Reynolds numbers, which can be seen towards the end of the same time series. As we increase the rate of change of Reynolds number ($\dot{Re}_{avg} = 143.3 \text{ s}^{-1}$), the bursts occur more frequently as shown in Figure 3.3b. With further increase in the rate of change of Reynolds number, we notice that the sustained oscillations at higher Reynolds numbers, which is seen towards the end of a given time series, persist over a wider range of Reynolds numbers. These sustained oscillations increase its occurrence to a wider range of Reynolds numbers, by merging with the bursts preceding them i.e., the sustained oscillations start at a lower Reynolds number. The sustained oscillations continue to increase its range of occurrence with increasing the rate of change of Reynolds number, resulting in limit-cycle oscillations (i.e., the state of screech), refer to Figure 3.3(a-f). The state of afterburner transitions to screech as we increase the rate of change of Reynolds number for the same operating conditions. We would like to note that, for the mentioned fuel flow rate to the preheater and the afterburner, and even at the lowest rate of change of Reynolds number ($\dot{Re}_{avg} = 102.9 \text{ s}^{-1}$), the acoustic pressure of the

afterburner exhibits the presence of a few bursts (Figure 3.3a). On the contrary, at lower fuel flow rates to the preheater and the afterburner, and with nearly same rate of change of Reynolds number, we did not observe intermittency and the afterburner was in the state of combustion noise (Figure 3.2a). Therefore, for the current fuel flow rate setting, the afterburner requires further reduction in the rate of change of Reynolds number to maintain the system dynamics in the state of combustion noise.

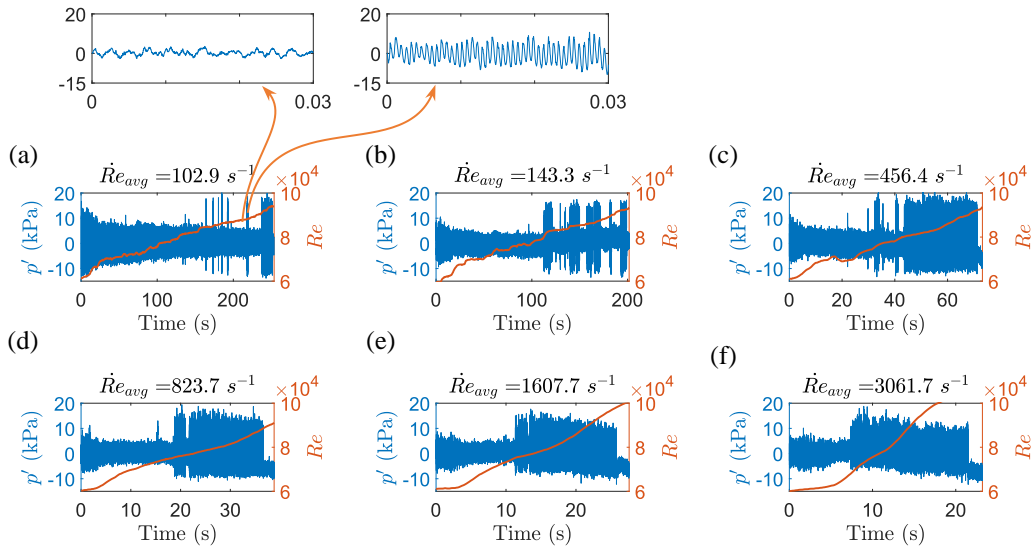


Figure 3.3 : Time series of acoustic pressure and the corresponding Reynolds number is plotted for increasing rate of change of Reynolds number from (a) to (f). A magnified view of aperiodic oscillations and periodic oscillations during bursts is shown in (a). The fuel flow rate of the preheater and the afterburner for this experiment is 29 lph and 41 lph, respectively.

3.3. ANALYSIS OF INTERMITTENCY

We find different methods for characterizing intermittency in the literature (Grebogi et al., 1987; Hirsch et al., 1982; Pomeau and Manneville, 1980; Xiao et al., 2009). A few statistical methods that are applied to characterize the state of intermittency are probability distribution of duration of aperiodic oscillations, mean duration of aperiodic oscillations, return map, and recurrence analysis (Nair et al., 2014b; Pawar et

al., 2015). These methods are applied to intermittency that are observed when the control parameter is changed in a quasi-static manner. In those experiments, the control parameter is fixed and the acoustic pressure is acquired for sufficiently longer duration to satisfy statistical stationarity. However, these methods are not suitable to our experiment as we measure the acoustic pressure for a short duration, which is limited by the time taken to traverse a given range of Reynolds number corresponding to a particular rate of change of Reynolds number. Therefore, we analysed intermittency using recurrence plots, probability density function (PDF) of the amplitude of pressure, variation of the amplitude of bursts, variation of the number of bursts of periodic oscillations, and the inlet conditions corresponding to onset of bursts, with respect to different rates of change of Reynolds number.

3.3.1. Analysis of intermittency using recurrence plot

Periodic phenomenon is a characteristic feature of thermoacoustic instability in most of the combustion systems; therefore, the recurrence of the system to a previous state is expected in the phase space. As the representation of phase portrait is limited to three-dimensional space, the evolution of a system in a high-dimensional phase space plotted in three-dimensional space may not be accurate. In most experiments, tracking all of the physical parameters affecting the system behaviour is difficult and is constrained to measuring a few parameters. In such a scenario, the dynamics of the thermoacoustic system can be visualized and quantified by reconstructing the phase space from the time series of a single dynamic variable i.e., measured acoustic pressure fluctuations in our experiments. The phase space reconstruction from a single variable is known as delay embedding theorem proposed by Takens [55]. In this method, a state of the dynamical system is constructed as a vector from a set of delayed values of the measured time

series. The evolution of such a vector reconstructs the phase space of the system. The elements of the vector signify the independent system parameters and the number of elements is the dimension of the system. In order to construct the vector and thereby the phase space of the system, we need to obtain the optimum time delay (τ) between the elements of the vector and the minimum embedding dimension (d_o). We obtain the optimum time delay and embedding dimension using average mutual information [56] and false nearest neighbourhood method [57], respectively. A detailed explanation and methodology for reconstructing the phase space is provided in Refs [17, 58]. The delay vector (\mathbf{p}'_i) is of the form shown below

$$\mathbf{p}'_i = [p'(t), p'(t + \tau), p'(t + 2\tau), \dots, p'(t + (d - 1)\tau)] \quad (3.1)$$

where $i = 1, 2, \dots, N_o - d_o\tau$

The phase portraits of the aperiodic oscillations, intermittency and periodic oscillations of pressure time series are shown in Figure 3.4. During aperiodic oscillations, the evolution of the system is bound to a small region in the phase space and exhibit a disorder behaviour (Figure 3.4a). On the other hand, during periodic oscillations, the system evolves in a ring like structure in the phase space with a time scale equal to the period of oscillations (Figure 3.4c). During intermittency, the evolution of the system fills both the regions of the aperiodic oscillations and the periodic oscillations in the phase space (Figure 3.4b).

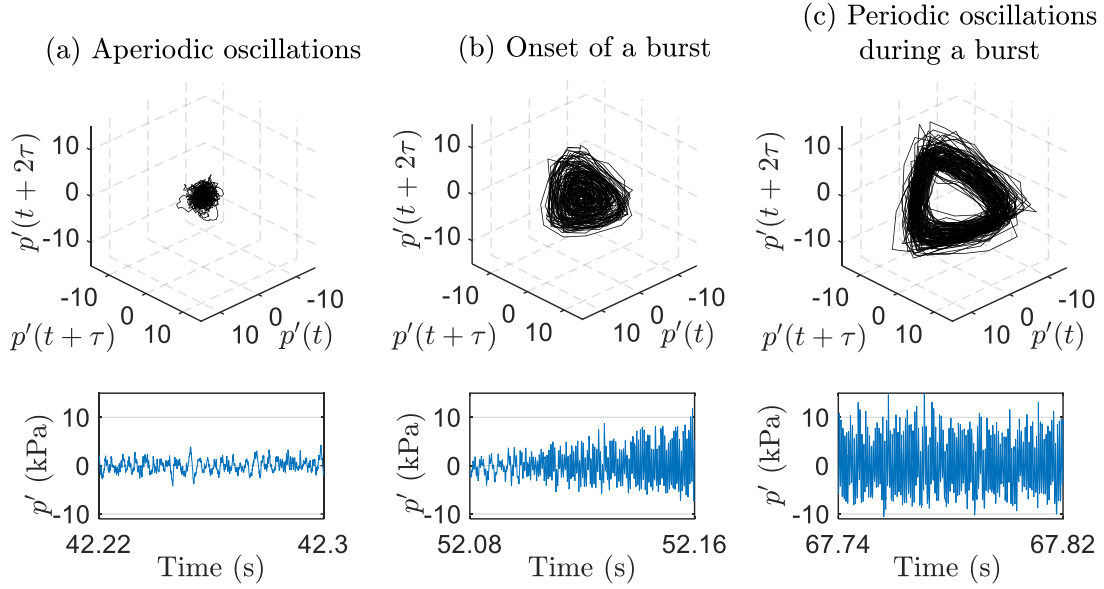


Figure 3.4 : Phase portrait of different dynamical states of the acoustic pressure for the rate of change of Reynolds number, $\dot{Re}_{avg} = 456.4 \text{ s}^{-1}$ obtained for 80 ms. (a) Aperiodic oscillations between bursts ($\tau = 15$, $d_o = 11$), (b) Oscillations at the onset of a burst ($\tau = 4$, $d_o = 11$) and (c) periodic oscillations during a burst ($\tau = 4$, $d_o = 11$).

Further, the recurrence behaviour of the phase space trajectory is characterized using a method based on recurrence plot (RP). Here, a distance matrix is formed by the Euclidean distance calculation for every state of the phase space trajectory to every other state of it. For practical purposes, a state is considered to be recurring, if the state is within a threshold distance (ϵ) from the reference state. Thus, a recurrence matrix is created, which is a two-dimensional matrix with 1's (black in RP) and 0's (white in RP): 1 representing the recurrence of the phase space trajectory to a given state and 0 representing the divergence of the trajectory with respect to the given state. We obtain the recurrence matrix using the following formula

$$R_{ij} = \Theta(\epsilon - \|\mathbf{p}'_i - \mathbf{p}'_j\|) \quad (3.2)$$

where $i = 1, 2, \dots, N_o - d_o\tau$ and Θ is the Heaviside step function.

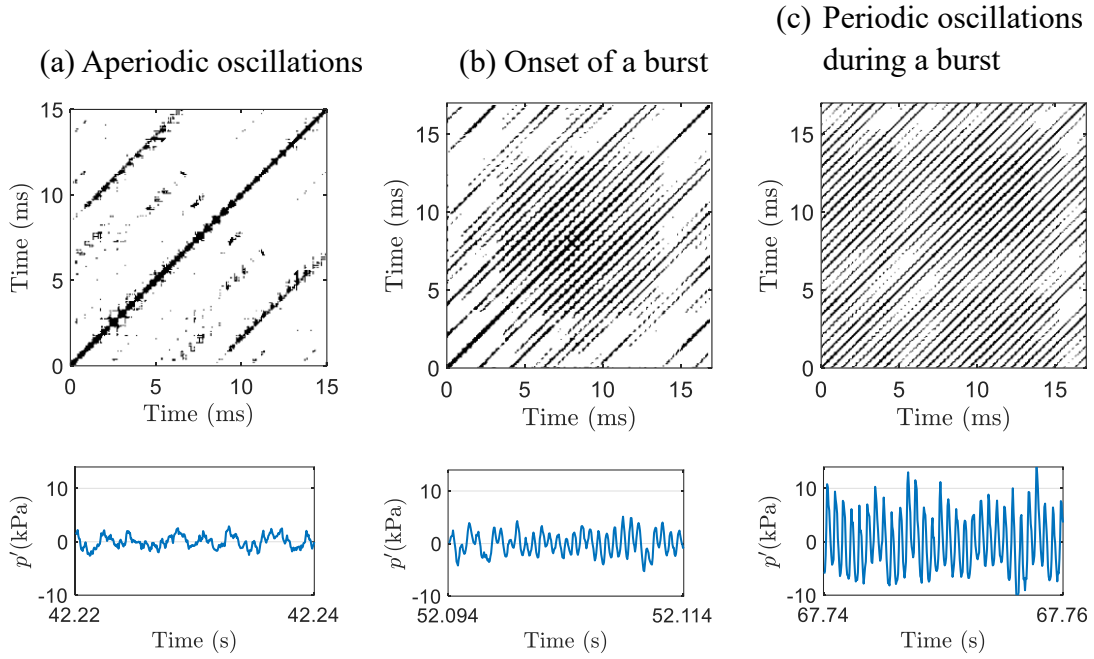


Figure 3.5 : Recurrence plot (RP) of the time series of acoustic pressure of the three different dynamical states with $\bar{Re}_{avg} = 456.4 \text{ s}^{-1}$ plotted for duration of 20 ms : (a) aperiodic oscillations ($\tau = 8$, $d_o = 11$, $\epsilon = 35\%$), (b) Onset of a burst ($\tau = 5$, $d_o = 11$, $\epsilon = 35\%$) and (c) periodic oscillation during burst ($\tau = 4$, $d_o = 11$, $\epsilon = 35\%$).

In Figure 3.5, we plot the recurrence matrix obtained for a pressure time series in three different regions: aperiodic oscillations, onset of burst, and periodic oscillations. We down sampled the pressure time series by a factor of three, to reduce the recurrence matrix size for plotting and visualization. During aperiodic oscillations, the RP does not have a distinct pattern. At the onset of the burst, parallel diagonal lines of short length appear as streaks and are random. During the periodic oscillations, continuous parallel diagonal lines appear and the distance between the diagonal lines correspond to the time period of the oscillations.

The recurrence quantification measure such as Recurrence Rate (RR) is used as an early warning measure for an impending thermoacoustic instability [23, 30]. The recurrence rate represents the fraction of the 1's (black points) present in the recurrence matrix.

The recurrence rate is obtained using the following formula:

$$RR = \frac{1}{N_1^2} \sum_{i,j=1}^{N_1} R_{ij} \quad (3.3)$$

where $N_1 = N_o - d_o\tau$

A mean recurrence rate is obtained for the pressure time series corresponding to the air flow rate between 0.34 and 0.42 kg/s for each of the rate of change of air flow rate. The recurrence rate is obtained for the pressure time series with a sliding window of 7500 samples. Then a mean recurrence rate is obtained from the recurrence rates corresponding to all of the windows. The mean recurrence rate is plotted in Figure 3.6 for each of the rate of change of air flow rate. For combustion noise, the evolution of the system is within a small bound, so the recurrence rate is high; as the system transitions to periodic oscillations, the state of the system moves away from the small bound resulting in lesser recurrence states as compared to combustion noise. We estimated the recurrence rate to check if this measure will work even for rate induced bifurcation of combustors. We show in Figure 3.6, that the recurrence rate is high for low rate of change of air flow rate i.e., for the time series with few bursts, and decreases as the rate of change of air flow rate is increased, till the limit-cycle oscillations. A threshold of recurrence rate can be set depending on a particular combustor and forewarn the operator to reduce the rate of change of parameter about the impending thermoacoustic instability. The trend is similar to that observed in the quasi-static experiments of Refs. [23, 30]. Therefore, the recurrence rate can be used as an early warning measure even for the rate induced bifurcation of the combustors.

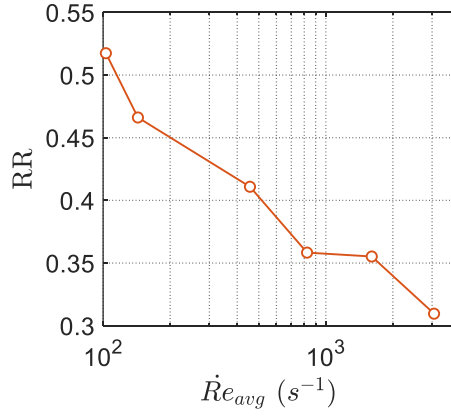


Figure 3.6 : The variation of the mean recurrence rate corresponding to the rate of change of Reynolds number.

3.3.2. Probability distribution of the amplitude of pressure

The afterburner undergoes a transition from the state of combustion noise to thermoacoustic instability through intermittency. The state of intermittency transitions through varying degrees, manifested in the time series of pressure as an increasing proportion of the high-amplitude periodic oscillations with respect to the low-amplitude aperiodic oscillations. Therefore, to examine the probability of occurrence of different states in the time series of pressure, we obtained the probability density function of the amplitude of time series of pressure fluctuations by the following procedure. We filtered the time series of pressure in the frequency band between 1,200 and 1,700 Hz, to filter out the underlying low-amplitude aperiodic fluctuations from the bursts of periodic oscillations. We chose the frequency band of the filter considering the variation of frequency of the periodic oscillations at different rates of change of Reynolds number. We obtained the amplitude of the filtered pressure time series using Hilbert transform. One such instantaneous amplitude, corresponding to $\dot{Re}_{avg} = 143.3 s^{-1}$ is plotted in Figure 3.7a and we can see the rise and fall of amplitude during the bursts.

We plotted the probability density function (PDF) of the amplitude of the time series of pressure fluctuations corresponding to each of the rate of change of Reynolds number (\dot{Re}_{avg}), as shown in Figure 3.7b. We observe a bimodal distribution of the PDF with two peaks corresponding to the amplitude of the combustion noise and the bursts of high-amplitude periodic oscillations. For the PDF corresponding to the low rate of change of Reynolds number ($\dot{Re}_{avg} = 102.9 \text{ s}^{-1}$), the major portion of the area under the distribution is concentrated at low amplitude of pressure, suggesting the predominant state as low-amplitude aperiodic oscillations. Similarly, for the PDF corresponding to the high rate of change of Reynolds number ($\dot{Re}_{avg} = 3,061.7 \text{ s}^{-1}$), the major portion of the area under the distribution is concentrated at high amplitude of pressure, suggesting the predominant state as high-amplitude periodic oscillations. For the PDFs corresponding to the rate of change of Reynolds number between $\dot{Re}_{avg} = 102.9 \text{ s}^{-1}$ and $\dot{Re}_{avg} = 3,061.7 \text{ s}^{-1}$, the major area under the distribution gradually shifts from the amplitude corresponding to combustion noise to that of the periodic oscillations with increasing rate of change of Reynolds number indicating the transition through intermittency.

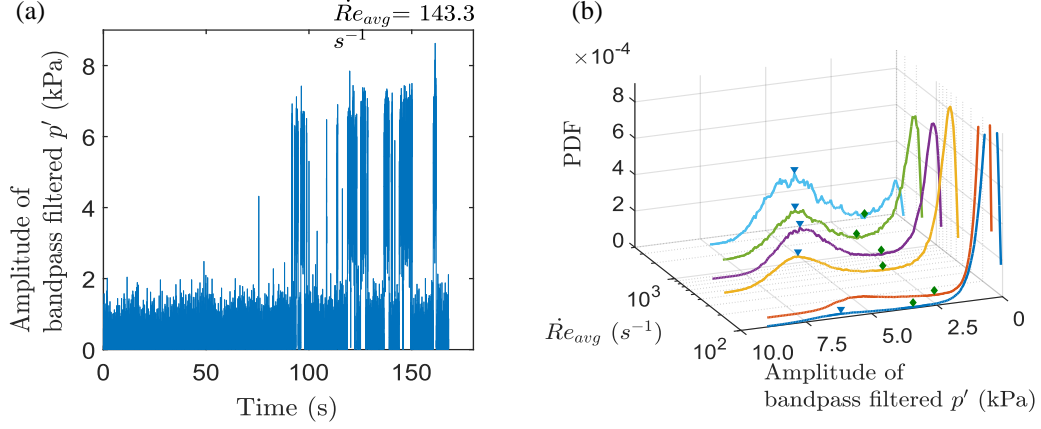


Figure 3.7: (a) The amplitude of acoustic pressure which is band pass filtered, corresponding to $\dot{Re}_{avg} = 143.3 \text{ s}^{-1}$. (b) The PDF of amplitude of acoustic pressure for different rates of change of Reynolds number (\dot{Re}_{avg}).

3.3.3. Variation of the amplitude of bursts

The instantaneous amplitude of bursts varies among the bursts as each burst occurs at a different Reynolds number for a given rate of change of Reynolds number. This is in contrast to the amplitude of bursts observed in quasi-static experiments (Nair et al., 2014b; Pawar et al., 2015), where the inlet conditions are maintained constant. Therefore, to study the variation of amplitude of bursts with respect to different rates of change of Reynolds number, we isolate the bursts in each time series of pressure, from the low-amplitude aperiodic oscillations that occur between the bursts, using a threshold. We, then, average the amplitude of the isolated bursts for a given rate of change of Reynolds number and study its variation at different rate of change of Reynolds number.

We find in literature that the bursts are identified as a region above a threshold amplitude in the pressure time series (Hammer et al., 1994; Platt et al., 1994). In our case, we define a threshold amplitude using the PDF of the amplitude of pressure, refer

to Figure 3.7b. We choose the threshold amplitude for each of the PDF, as the amplitude of pressure corresponding to the minimum probability between the two peaks, marked as \blacklozenge in Figure 3.7b. We, then, calculate the average of the amplitude of the pressure that are above the chosen threshold. The estimated average amplitude represents the average amplitude of the bursts of periodic oscillations for each of the rate of change of Reynolds number and are plotted in Figure 3.8. We show in Figure 3.8, that the average amplitude of bursts of periodic oscillations decreases with increasing rate of change of Reynolds number except that corresponding to $\dot{Re}_{avg} = 143.3 \text{ s}^{-1}$. The decreasing trend of the average amplitude of bursts is supported by the decreasing amplitude of pressure corresponding to the maximum probability, marked as \blacktriangledown in Figure 3.7b, with increasing rate of change of Reynolds number. Also, we have shown in Figure 3.3 that with increasing the rate of change of Reynolds number the system approaches the state of limit cycle oscillations. Therefore, the amplitude of the bursts is higher than the amplitude of the limit cycle oscillations. The observed amplitude variation is in contrast to the conventional understanding of increasing amplitude of pressure oscillations with increase in control parameter (Chakravarthy et al., 2007). Also, Pawar *et al.* (2015) showed in their experiments under quasi-static conditions that the maximum amplitude of bursts is higher than that of the limit cycle oscillations by varying the location of the flame holder. Therefore, the phenomenon of high-amplitude bursts needs further investigation to understand the mechanism causing it. In the meanwhile, we caution the engineers that the amplitude of the bursts of periodic oscillations during intermittency can be more detrimental than that of the limit cycle oscillations.

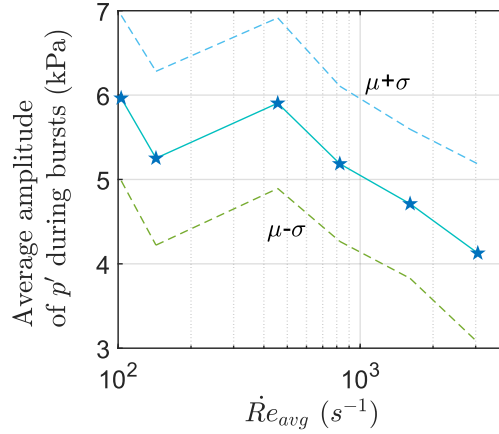


Figure 3.8 : Plot of the average amplitude (μ) of bursts of periodic oscillations and the corresponding standard deviation (σ) of the amplitude distribution for different rates of change of Reynolds number (\dot{Re}_{avg}).

3.3.4. Variation of the number of bursts

In our study of rate dependent transition, the variation of the number of bursts may not be explicit from the time series of pressure fluctuations approaching limit cycle oscillations, therefore we count the number of bursts to study the proximity of the system dynamics to thermoacoustic instability. We used the same threshold mentioned in the preceding paragraph, to count the number of times the time series of pressure crosses the threshold, which is the number of bursts. The variation of the number of bursts is plotted in Figure 3.9 corresponding to each of the rate of change of Reynolds number. We show in Figure 3.9, that as the rate of change of Reynolds number is increased, the number of bursts exhibit an increasing trend as more bursts start to appear in the time series. With further increase in the rate of change of Reynolds number, the number of bursts in the signal decreases as the proportion of aperiodic oscillations in the pressure time series decreases continually and the bursts of periodic oscillations merge together till limit cycle oscillations. At limit cycle oscillations, the number of bursts should be one and therefore, the decreasing number of bursts in Figure 3.9

signifies the proximity of the system dynamics to the limit cycle oscillations, i.e., thermoacoustic instability. Additionally, we conducted experiments to study rate dependent transitions in the afterburner with six different fuel flow rate settings in the preheater and the afterburner. We observed rate dependent transition to screech via intermittency in all of the six different experimental conditions and the number of bursts follow a similar trend.

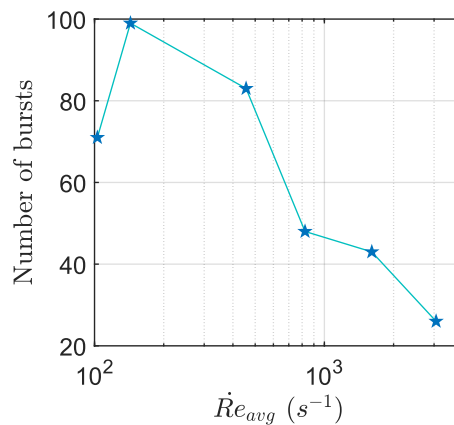


Figure 3.9 : The number of bursts in the time series of pressure is plotted for different rates of change of Reynolds number (\dot{Re}_{avg}).

3.3.5. Promotion of rate dependent transition

As we increase the rate of change of air flow rate (consequently Reynolds number) in different experiments, we notice that the onset of a burst of periodic oscillations occurs at a lower air flow rate. We conducted experiments with different pre-heater and afterburner fuel flow rates for different rate of change of air flow rate. The preheater fuel flow rates set were 23, 26 and 29 lph; for each of the preheater fuel flow rates, afterburner fuel flow rates were set to 36, 41 and 46 lph. We obtained experimentally the air flow rate at which a burst of periodic oscillations onsets for different rate of change of air flow rate with each of the nine fuel flow rate combinations of the preheater and the afterburner. The air flow rate at which burst of periodic oscillations onsets is

plotted in Figure 3.10 as three 3d plots, one for each of the preheater fuel flow rates. In the plots, the rate of change of air flow rate tending to zero represents quasi-static condition and a higher rate represents a steep rise in the air flow rate. In the Figure 3.10, for each of the preheater and the afterburner fuel flow rates, the burst onsets at a lower air flow rate with increasing rate of change of air flow rate. The trend of decreasing air flow rate at which burst onsets is highlighted in Figure 3.10 with a greyscale surface plot which is a linear fit to the experimental data points.

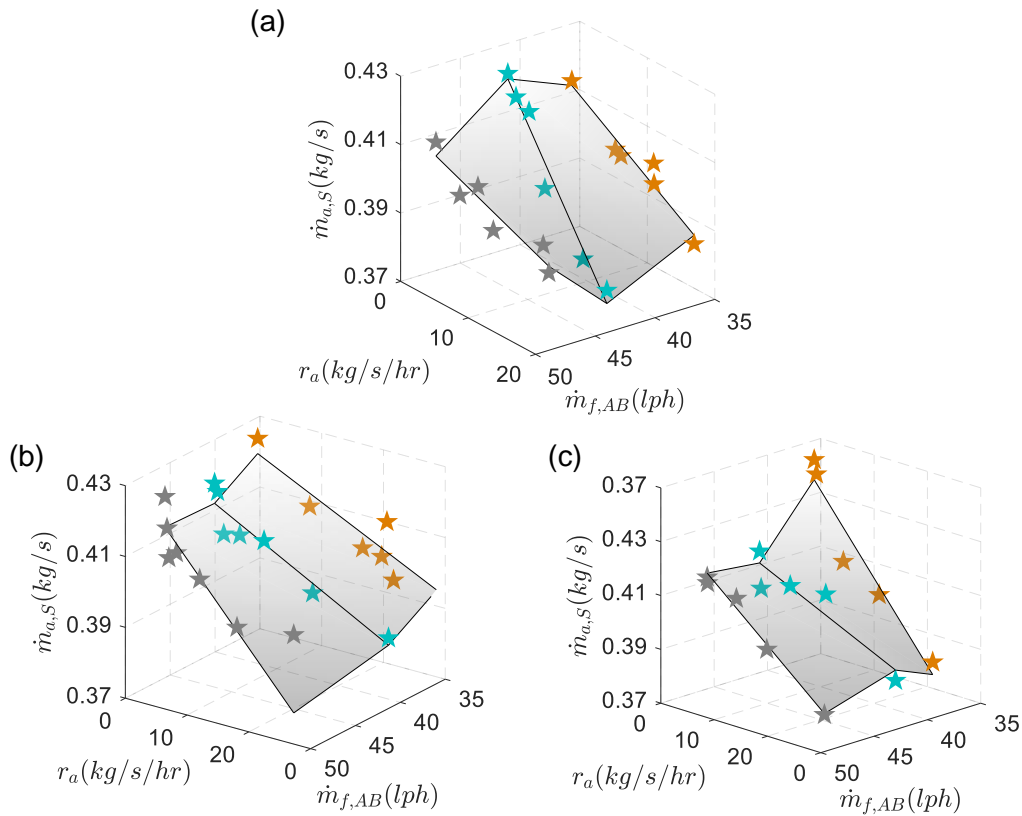


Figure 3.10 : The onset of burst of periodic oscillations depends on the rate of change of air flow rate. The air flow rate corresponding to the onset of a burst of periodic oscillations is plotted for different preheater and afterburner fuel flow rates: (a) 23 lph (b) 26 lph and (c) 29 lph. Rate of change of air flow rate (r_a), mass flow rate of air corresponding to onset of screech ($\dot{m}_{a,s}$), mass flow rate of fuel in the model afterburner ($\dot{m}_{f,AB}$).

The air flow rate corresponding to the onset of burst is converted to corresponding Reynolds number (Re_s) for the operating condition with fuel flow rate of 26 lph for

preheater and 46 lph for afterburner. Similar to rate of change of air flow rate, the rate of change of Reynolds number close to zero represents quasi-static condition and a higher rate represents a steep rise in the Reynolds number.

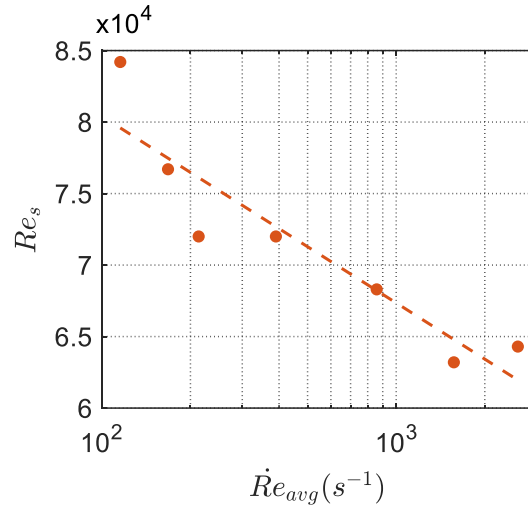


Figure 3.11 : The Reynolds number corresponding to the onset of a burst of periodic oscillations for different rates of change of Reynolds number.

We, then, obtained the Re_s corresponding to the $\dot{Re}_{avg} = 1 s^{-1}$, ($Re_{s,1}$), by extrapolation, for each of the operating conditions corresponding to the preheater fuel flow rate of 26 lph and with three afterburner fuel flow rates of 36, 41, and 46 lph. $\dot{Re}_{avg} = 1 s^{-1}$ is two orders lower compared to the lowest of the experimentally achieved \dot{Re}_{avg} and therefore, $\dot{Re}_{avg} = 1 s^{-1}$ is assumed to represent quasi-static variation of Reynolds number. $Re_s - Re_{s,1}$ represents the extent of promotion of the Reynolds number corresponding to the onset of burst, from the reference value of $Re_{s,1}$ (near quasi-static condition), as the rate of change of Reynolds number is increased. We plotted in Figure 3.12a, $Re_s - Re_{s,1}$ for different rates of change of Reynolds number and for different fuel flow rates to the afterburner. The extent of promotion of the Reynolds number corresponding to the onset of burst ($Re_s - Re_{s,1}$) collapses to a single curve, varying only with the rate of change of Reynolds number and does not depend

on the fuel flow rate to the afterburner. The equivalence ratio (ϕ_s) corresponding to the onset of burst gets delayed, i.e., the bursts onset at a higher equivalence ratio with increase in the rate of change of equivalence ratio. Similar to the promotion of the Re_s , the amount of delay in equivalence ratio ($\phi_s - \phi_{s,1}$) is plotted in Figure 3.12b and does not depend on the fuel flow rate to the afterburner.

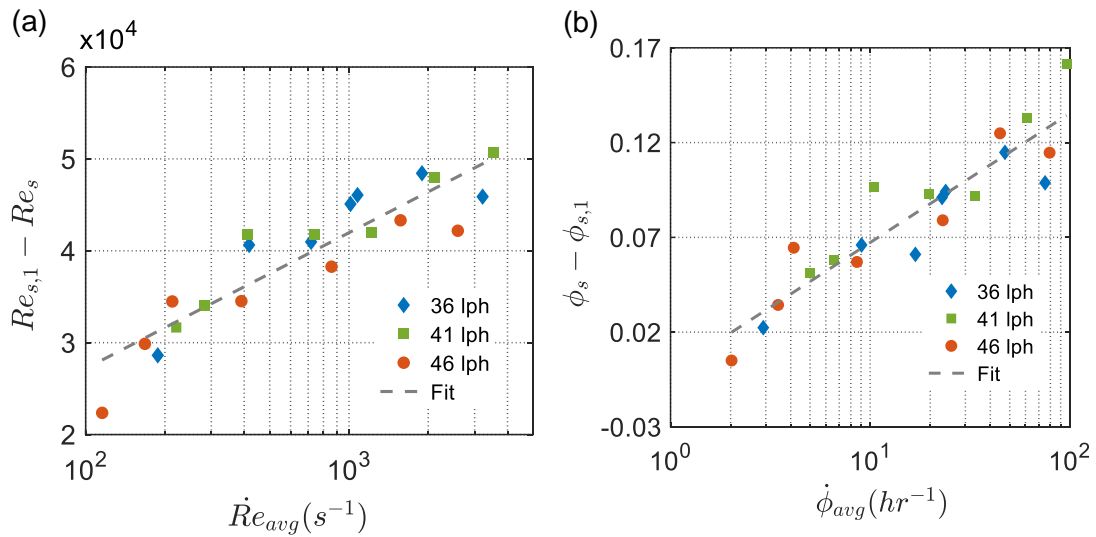


Figure 3.12 : (a) The promotion of Reynolds number corresponding to the onset of a burst of periodic oscillations for different fuel flow rates in the afterburner. (b) The corresponding plot in terms of delay in equivalence ratio.

We examined the frequency of the periodic oscillations for different rates of change of Reynolds number as the equivalence ratio corresponding to the onset of burst differs. For a given rate of change of Reynolds number, we segmented the time series of acoustic pressure with a window size of 5,000 samples and obtained the dominant frequency in each window. The dominant frequency of pressure oscillations is plotted with time in Figure 3.13a, for the time series of pressure fluctuations corresponding to $\dot{Re}_{avg} = 213.3 s^{-1}$. The amplitude spectrum of the pressure fluctuations is broadband during the low-amplitude pressure oscillations and the corresponding dominant frequency is approximately 320 Hz (Figure 3.13a). The dominant frequency during

bursts of periodic oscillations is approximately 1,490 Hz. The frequency of bursts of periodic oscillations for the time series of pressure corresponding to $\dot{Re}_{avg} = 213.3 \text{ s}^{-1}$ varies from 1,490 to 1,435 Hz, refer to Figure 3.13a. The frequency of bursts of periodic oscillations decreases with increase in Reynolds number for a given rate of change of Reynolds number. As the Reynolds number is increased with a constant fuel flow rate to the preheater and the afterburner, the overall fuel-air ratio decreases; consequently, the gas temperature decreases. Therefore, the frequency of bursts of periodic oscillations decreases with decrease in gas temperature. We plotted in Figure 3.13b, the maximum of the dominant frequency observed in the pressure time series for each of the rate of change of Reynolds number. As the rate of change of Reynolds number is increased, we observe an increase in the maximum oscillation frequency, refer to Figure 3.13b. The increase in the maximum oscillation frequency corroborates with the higher equivalence ratio corresponding to the onset of bursts with increasing rate of change of Reynolds number.

Thus, the rate of change of Reynolds number affects the screech onset conditions and the higher rate of change of Reynolds number widens the thermoacoustic stability map in terms of range of inlet conditions and the frequency of the oscillation. Therefore, in gas turbine combustors which undergo rapid variation of inlet conditions, the rate of change of Reynolds number or the equivalence ratio should be a parameter to obtain a reliable thermoacoustic stability map of the combustors.

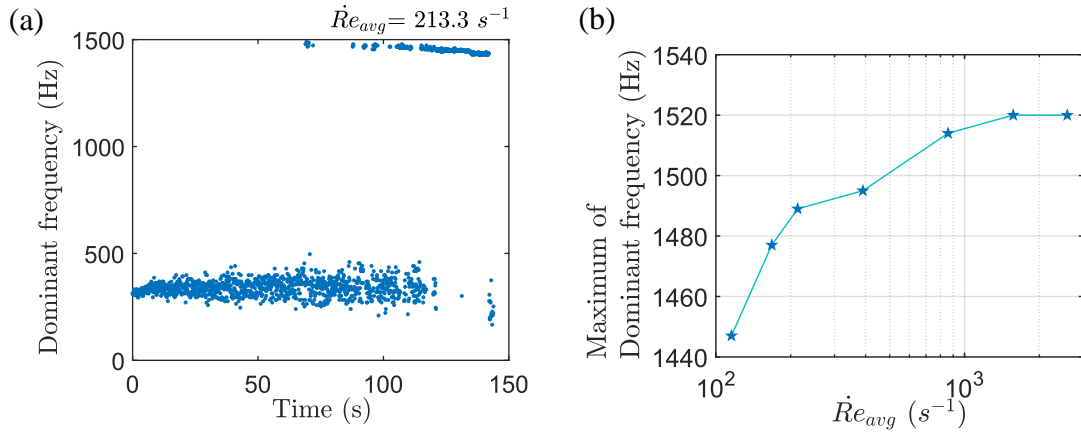


Figure 3.13 : (a) The variation of frequency of periodic oscillations in the time series of pressure for a given rate of change of Reynolds number. (b) The maximum dominant frequency of periodic oscillations for different rates of change of Reynolds number.

3.4. SUMMARY

In this study, we investigate experimentally, the rate dependent transition to screech in an afterburner rig. We showed that the onset of screech is dependent on the rate at which the Reynolds number is increased. We show for the first time that the afterburner transitions from combustion noise to thermoacoustic instability via intermittency, as the rate of change of Reynolds number is increased. We analysed the rate dependent transition to screech by studying the variation of the amplitude of bursts, variation of the number of bursts of periodic oscillations, and the inlet conditions corresponding to the onset of bursts. In the analysis, we observe that the amplitude of bursts is higher than that of the limit cycle oscillations.

In the analysis of the number of bursts during intermittency, we chose a threshold to identify the bursts, based on the probability density function of the amplitude of pressure. The time series of pressure is noisy and discerning the number of bursts is difficult particularly for the time series obtained close to limit cycle oscillation. We

captured the trend in the number of bursts, using the method based on probability density function. The decreasing trend at higher rate of change of Reynolds number signifies the proximity of the system dynamics to the sustained oscillations i.e., thermoacoustic instability.

We observed that the onset of bursts occurs earlier, i.e., bursts occurring at a lower Reynolds number, as the rate of change of Reynolds number is increased. The maximum frequency of the periodic oscillations increases with increasing rate of change of Reynolds number. Therefore, the region of stable operation of a combustor in the stability map reduces with a higher rate of change of inlet parameters.

CHAPTER 4

FLAME DYNAMICS DURING TRANSVERSE THERMOACOUSTIC INSTABILITY

Flame dynamics during thermoacoustic instability is one of the primary areas of investigation in the study of mechanism causing thermoacoustic instability. In the 1950's, self-excited thermoacoustic experiments with bluff body flame holders revealed that alternate vortex shedding from the two shear layers of the bluff body is the mechanism causing transverse thermoacoustic instability (Elias, 1959; Rogers, 1956). Since then, there are hardly any experimental studies of self-excited transverse thermoacoustic instability in bluff-body-stabilized combustors, even though advanced optical diagnostic and processing tools are available to date. We investigated the flame dynamics during self-excited transverse thermoacoustic instability in a combustor with flame stabilized by bluff body flame holders and liquid fuel injection representative of a gas turbine afterburner.

4.1. GLOBAL FLAME DYNAMICS DURING THERMOACOUSTIC INSTABILITY

We conducted experiments to obtain screech by increasing the air flow rate at a finite rate and the corresponding average rate of change of Reynolds number is 335 s^{-1} . We obtained the global heat release rate using photomultiplier tube (PMT) for the lower half of the test section corresponding to the flame dynamics of the bottom flame holder (region marked in Figure 2.6). We show in Figure 4.1(a) the time series of acoustic

pressure (p') and unsteady heat release rate (\dot{q}'). We have marked in Figure 4.1(a) three blue lines each representing different dynamical state of the system with increasing levels of coupling strength between p' and \dot{q}' . These three regions correspond to different flow Reynolds number while the Reynolds number is varied at a certain rate. We have arranged the Figure 4.1 in three columns (columns I, II & III) with plots corresponding to the three dynamical states of the system. The rows of Figure 4.1 contains row (b): zoomed in view of the time series of p' and \dot{q}' for a duration of 50 ms (50 ms for the sake of viewing the oscillations), row (c): amplitude spectrum of p' and \dot{q}' obtained for a duration of 100 ms, row (d): amplitude scalogram of p' , row (e): amplitude scalogram of \dot{q}' , and row (f): wavelet coherence between p' and \dot{q}' .

We obtained the scalograms using continuous wavelet transform with analytic Morse wavelet ($\gamma = 3$, $\beta = 20$), (J M Lilly and Olhede, 2012; Jonathan M Lilly, 2017). The continuous wavelet transform is a time-frequency transform most appropriate for signals with time varying amplitude spectrum. The continuous wavelet transform is given by:

$$W(s, t_0) = \int_{-\infty}^{\infty} x(t) \Psi_{s,t_0}^*(t) dt \quad (4.1)$$

where $x(t)$ is the signal and $\Psi_{s,t_0}^*(t)$ represents the complex conjugate of the mother wavelet function $\Psi_{s,t_0}(t)$. The mother wavelet is given by $\Psi_{s,t_0}(t) = \frac{1}{\sqrt{s}} \Psi_0\left(\frac{t-t_0}{s}\right)$, where s is the time scale that determines the width of Ψ_0 and t_0 is the time shift of the wavelet function.

In the present scalogram analysis, Morse wavelet is used and it is a two-parameter wavelet function. The Fourier transform of the Morse wavelet is given by (J M Lilly and Olhede, 2012):

$$\Psi_{\beta,\gamma}(\omega) = U(\omega)a_{\beta,\gamma}\omega^\beta e^{-\omega^\gamma} \quad (4.2)$$

where $U(\omega)$ is the unit step, $a_{\beta,\gamma}$ is a normalizing constant, and γ characterizes the symmetry of the Morse wavelet. The skewness of the Morse wavelet is equal to 0 when gamma is equal to 3.

We obtained the correlation in the time-frequency domain of signals between p' and q' by computing the cross-wavelet transform using analytic Morlet wavelet. The common spectral power can be understood from the magnitude-squared wavelet coherence which is derived from the cross-wavelet transform (Grinsted et al., 2004; Issartel et al., 2015). The phase information between the signals can be obtained from the complex-valued cross-wavelet transform. The magnitude-squared wavelet coherence of two time series l and m is given by:

$$W_{lm}(s, t_0) = \frac{|W_l^*(s, t_0)W_m(s, t_0)|^2}{|W_l(s, t_0)|^2|W_m(s, t_0)|^2} \quad (4.3)$$

where $W_l(s, t_0)$ and $W_m(s, t_0)$ denote the continuous wavelet transforms of l and m at scales s and positions t_0 . The superscript $*$ is the complex conjugate.

Morlet wavelet can be thought of as a sine wave modulated by a Gaussian. The complex Morlet wavelet is given by (Torrence and Compo, 1998):

$$\Psi_0(\eta) = \frac{1}{\sqrt[4]{\pi}} \left(e^{-\frac{\eta^2}{2}} \right) e^{i\omega_0 t} \quad (4.4)$$

where ω_0 is the wavenumber and η is a non-dimensional time parameter.

We observe bursts of periodic oscillations in the p' and mostly aperiodic oscillations without distinct bursts of periodic oscillations in the \dot{q}' in Figure 4.1(b, I). The amplitude spectrum of p' and \dot{q}' among the three dynamical states of the system have a dominant frequency with increasing amplitude (Figure 4.1(c, I – III)) and the dominant frequency is approximately 1300 Hz. The bursts of periodic oscillations are evident from the amplitude scalograms of p' with patches of high-amplitudes regions (Figure 4.1(d, I)) observed between frequency of 1000 and 2000 Hz. The bursts increase in amplitude and sustain for longer duration (Figure 4.1(d, II)) becoming a sustained high-amplitude periodic oscillation (Figure 4.1(d, I – III)) of p' . Although, we observe a similar trend of increasing number of patches of high-amplitude regions (bursts) in the scalogram of unsteady heat release rate (Figure 4.1(e, I – III)), the patches do not merge (Figure 4.1(e, III)) as observed for the acoustic pressure for the present operating conditions of the afterburner.

The common spectral power between p' and \dot{q}' in the frequency domain is interpreted using the contour plot of the magnitude-squared wavelet coherence. The phase relationship between p' and \dot{q}' for highly correlated regions is plotted as phasors in Figure 4.1f. We observe few patches of highly correlated regions between frequency of 1000 and 2000 Hz with changing phase values among those patches in Figure 4.1f. As the flow Reynolds number increases, the patches of highly correlated regions increase in number and the phasors align from left to right (refer Figure 4.1(f, II)). In

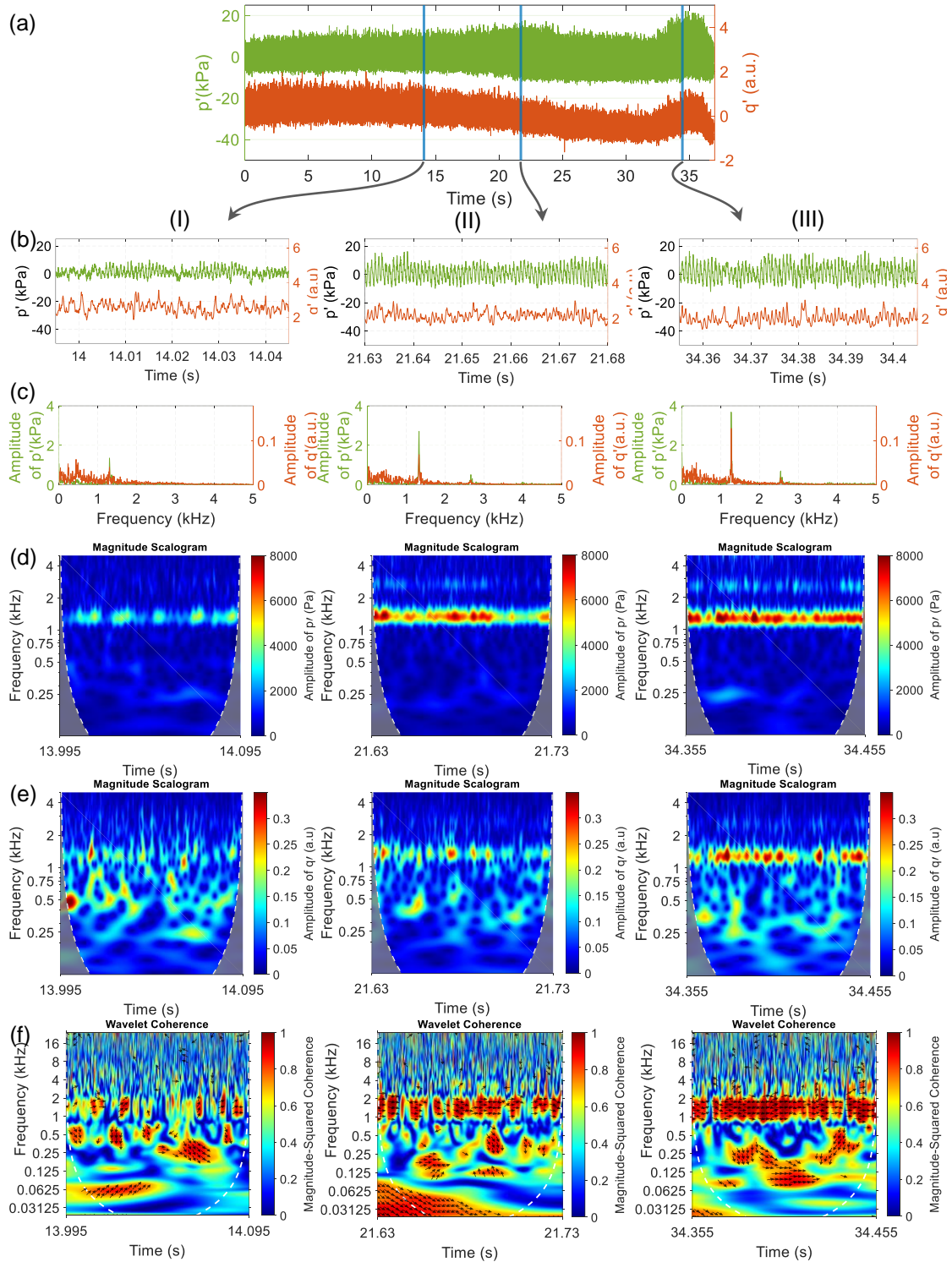


Figure 4.1 : (a) Time series of acoustic pressure and global heat release rate corresponding to flame dynamics of bottom flame holder. (b) Zoomed-in view of the time series for a duration of 50 ms (c) Amplitude spectrum of pressure and unsteady heat release rate obtained for a duration of 100 ms. (d), (e), and (f) correspond to amplitude scalogram of pressure, amplitude scalogram of and unsteady heat release rate, and wavelet coherence between acoustic pressure and unsteady heat release rate, respectively.

Figure 4.1(f, III), the highly correlated regions become nearly continuous with time and the phasors are coherent aligning to the right side in the mentioned frequency range. The increasing number of correlated regions in the mentioned frequency range suggests that the coupling between p' and \dot{q}' itself transitions from the state of no coupling during combustion noise to state of strong coupling during thermoacoustic instability through intermittent coupling with increasing coherence in the alignment of phasors. To illustrate it clearly, we plotted in Figure 4.2, the mean and standard deviation of the relative phase between p' and \dot{q}' corresponding to the dominant frequency of 1270 Hz and with wavelet coherence greater than 0.75, obtained for every two second data of p' and \dot{q}' . The coherence in the alignment of phasors can be inferred from the reduction in the standard deviation (error bars in Figure 4.2) of the relative phase between p' and \dot{q}' during the transition to sustained periodic oscillations.

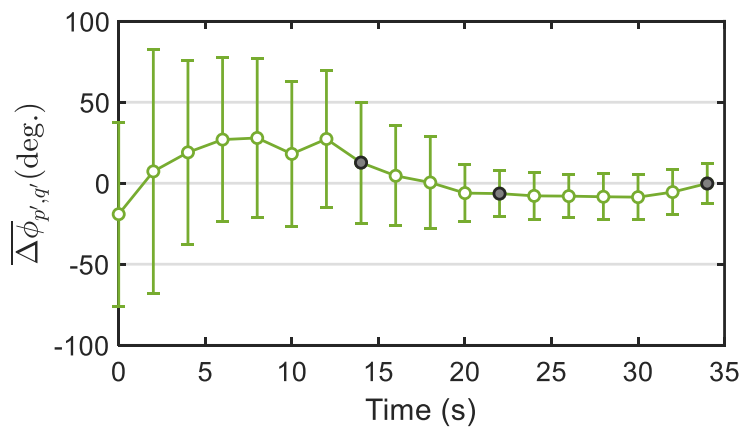


Figure 4.2 : Mean and standard deviation of relative phase between p' and \dot{q}' corresponding to dominant frequency of 1270 Hz and with wavelet coherence greater than 0.75 obtained for every two second data of p' and \dot{q}' . The back dots correspond to the three dynamical states used in Figure 4.1.

A recurrence-plot-based measure called probability of recurrence ($P(\tau)$) is used in the study of synchronization of p' and \dot{q}' (Pawar et al., 2017; Romano et al., 2005). The

probability that the system returns to the neighbourhood of a point on the trajectory in RP after a time τ , is given by $P(\tau)$.

$$P(\tau) = \frac{\sum_{i=1}^{N-\tau} R_{i,i+\tau}}{N - \tau} \quad (4.5)$$

In a closed loop trajectory, the plot of $P(\tau)$ will have multiple peaks at time lags corresponding to the multiples of time period of the closed loop trajectory. Values of time lags between the multiples of time period of a closed loop trajectory will have lower $P(\tau)$ as the trajectory would not have recurred to a given point on the trajectory for those time lags. In the scenario of phase synchronized oscillators, the peaks of $P(\tau)$ of different oscillators would coincide and are said to be in phase synchronization. That is, the recurrence of the trajectory to a given point on the trajectory of different oscillators happen at the same time lags. Pearson's coefficient or cross correlation coefficient of the $P(\tau)$ of two oscillators (CPR) is an indicator of the level of alignment of the time lags corresponding to the peak probabilities (Romano et al., 2005).

$$\text{CPR} = \frac{\langle \bar{P}_1(\tau > \tau_c) \bar{P}_2(\tau > \tau_c) \rangle}{\sigma_1 \sigma_2} \quad (4.6)$$

where \bar{P}_1 and \bar{P}_2 are the mean subtracted values of $P_1(\tau)$ and $P_2(\tau)$, respectively, and σ_1 and σ_2 are the standard deviations of $P_1(\tau)$ and $P_2(\tau)$, respectively. We modify the CPR definition used by Romano et. al. (2005) and Goswami et. al. (2012), to remove the effect of neighbourhood points of a given point on the trajectory and retain the recurring points of the trajectory. $\tau < \tau_c$ represents the time lag corresponding to the

neighbourhood of a given point and the point itself on the RPs. τ_c is selected based on the choice of the cut-off threshold (ϵ) used in the RPs.

Probability of recurrence, $P(\tau)$ of p' and q' are estimated for the three dynamical states of the system (Figure 4.1a) and are plotted in Figure 4.3 along with a repeat plot of the time series of p' and q' , and location of the three dynamical states. The RPs corresponding to the $P(\tau)$ of p' and q' are plotted in Figure 4.3. The RP of p' in Figure 4.3b-I has broken lines that are aligned parallel to the main diagonal line indicating existence of recurring trajectories in the phase space. The $P(\tau)$ of p' in Figure 4.3b-III shows regularly spaced peaks with peak values much less than 1. The RP and $P(\tau)$ of p' indicate bursts of periodic oscillations and is evident in the zoomed-in time series shown in Figure 4.1b-I. On the other hand, the RP of q' does not show a pattern with lines aligned to the main diagonal line. Consequently, the $P(\tau)$ of q' does not show peak probabilities of recurrence at regular intervals of time lag. The CPR between p' and q' is 0.25 and indicates a weak coupling between p' and q' . The RP of p' of the next two dynamical states Figure 4.3(c-I, d-I) have long lines aligned to the main diagonal line indicating periodic oscillations and consequently the $P(\tau)$ plots show peak probabilities approaching 1. The difference in the dynamical behaviour comes from the q' with the appearance of peak probabilities at apparently regular intervals in the $P(\tau)$ plots (refer Figure 4.3(c-III, d-III)). The CPR between p' and q' for the mentioned two dynamical states is 0.64 and 0.88, suggesting a strong coupling between p' and q' .

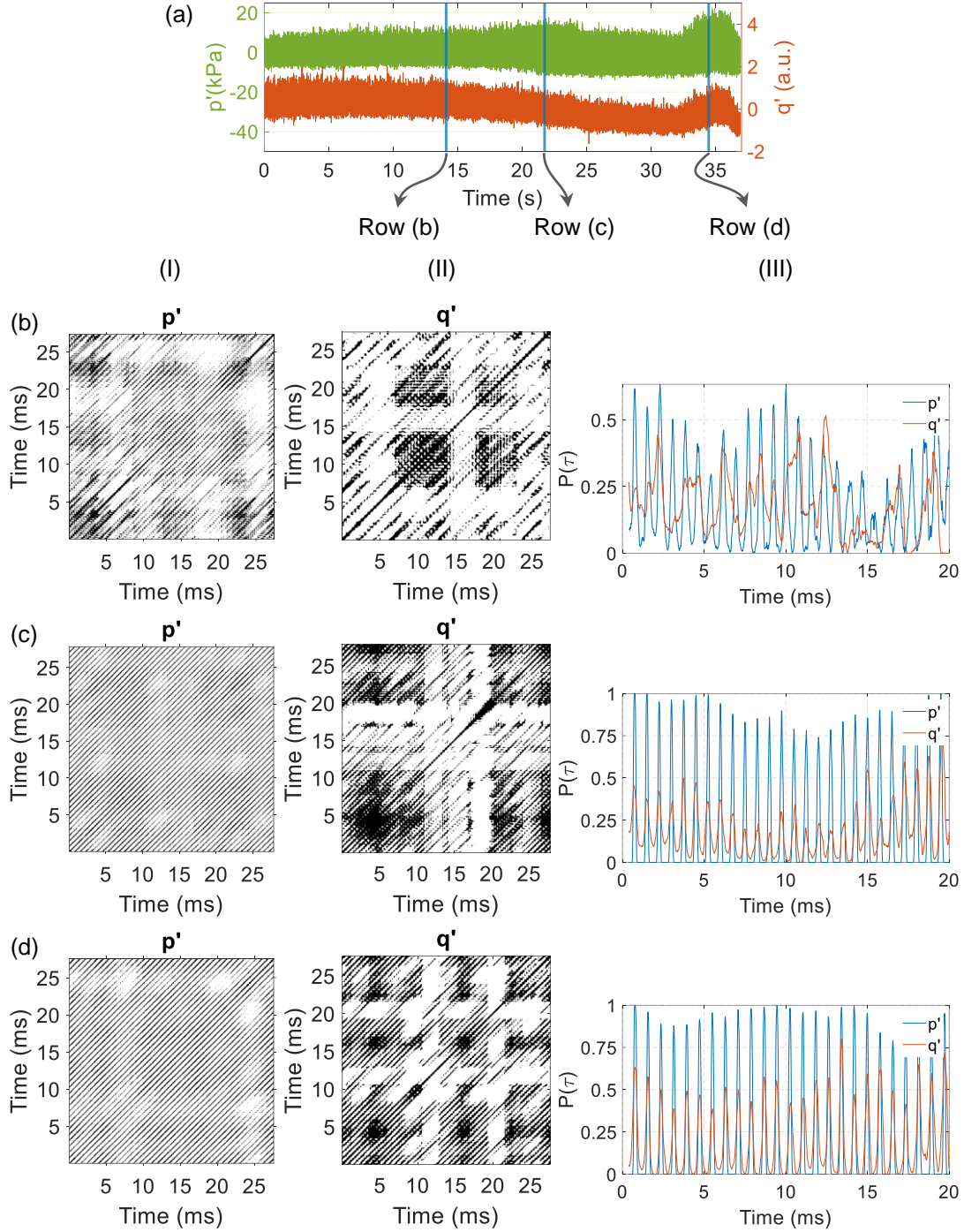


Figure 4.3 : (a) Time series of acoustic pressure and global heat release rate corresponding to flame dynamics of bottom flame holder. Columns (I) – (III) represent RPs of p' and q' , and $P(\tau)$, respectively, corresponding to the dynamical states marked in (a) as Row (b), Row (c) and Row (d). The parameter's values used in RPs of p' and q' are $d_o = 12$, $\epsilon = 20\%$ and $d_o = 12$, $\epsilon = 20\%$, respectively.

We plotted the variation of CPR at different time instances as the Reynolds number is increased at rate of 335 s^{-1} (refer, Figure 4.4). We observe that the CPR shows a steep

rise during the transition indicating a change in coupling strength from weak to strong coupling. In contrast, the rms of p' increases gradually even before the shift in the coupling strength occurs in the CPR.

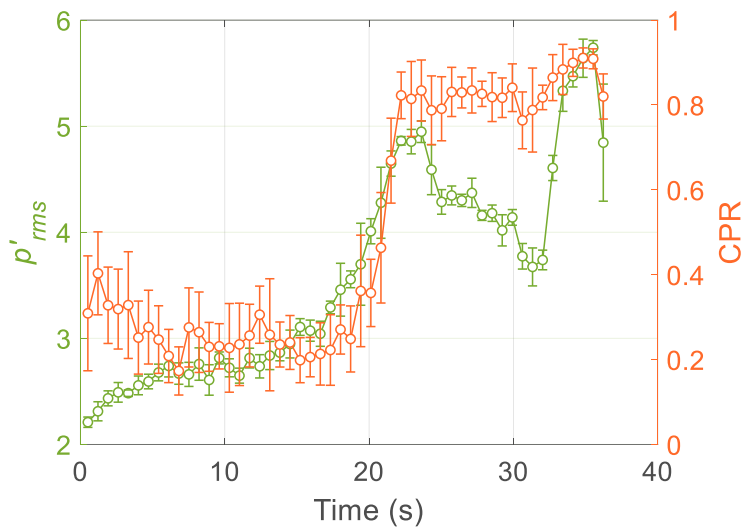


Figure 4.4 : The variation of CPR shows a step increase in coupling strength compared to the variation in rms of p' .

4.2. MECHANISM CAUSING TRANSVERSE THERMOACOUSTIC INSTABILITY

We obtained high-speed images (14k fps) of the flame dynamics during thermoacoustic instability for a region shown in Figure 2.6. We show the interaction of flames between multiple flame holders using high speed imaging of emissions from OH^* radicals in Figure 4.5. The images are phase averaged over 100 images corresponding to minimum, zero (during positive slope of the cycle), maximum, and zero (during negative slope of the cycle) of the p' measured at the bottom wall of the test section. We describe the flame dynamics corresponding to the top flame holder in the following sentences. We observe in Figure 4.5, Frame I, that the fuel-air mixture in the recirculation zone of the top flame holder ignites and the intensity of the OH^* emission

is higher. In Frame II, the reacting mixture in the recirculation zone of the top flame holder is drawn towards the wake of the middle flame holder. In Frame III, we observe that the reacting mixture curls as that entrained into a vortex. At the same time, we observe that the flame extinguishes in the recirculation zone of the top flame holder. In Frame 4, the flame front restores the flame surface consuming the roll-up and the reacting mixture gets convected downstream along with the flow. In the same frame, the mixture in the near wake reignites and the cycle repeats. A similar dynamics of flame is observed in the wake of bottom flame holder only that they roll-up in an asymmetric manner with respect to the flame dynamics corresponding to the top flame holder.

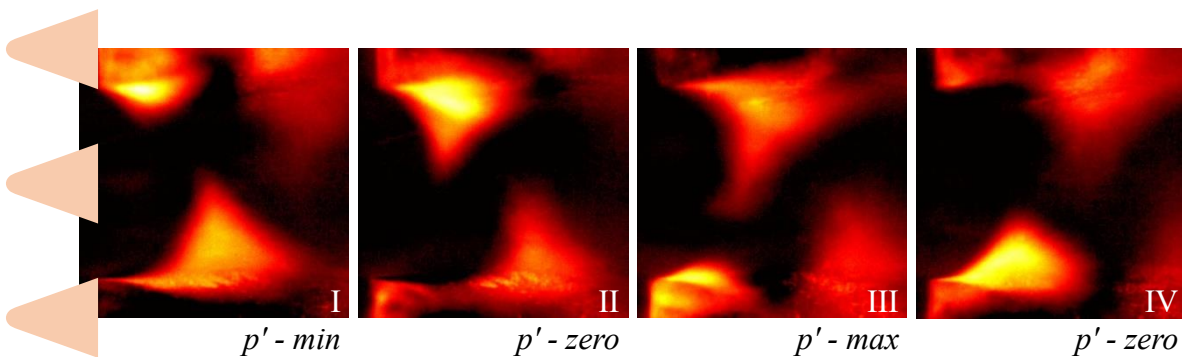


Figure 4.5 : Frames I – IV are phase averaged images corresponding to minimum, zero (positive slope), maximum, and zero (negative slope) of the p' measured at the bottom wall of the test section, respectively.

We hypothesise that the stream of fuel-air mixture issued out of the passage between top and middle flame holders (denoted as stream-1 in Figure 4.7a) flaps and rolls up alternatingly in the wakes of top and middle flame holder as shown schematically in Figure 4.7. The flapping of the stream-1 is induced by the acoustic velocity oscillation in the transverse direction. We mapped the sequence of events in the flame dynamics with respect to the oscillations of pressure in Figure 4.5. In order to understand the sequence of events in the flame dynamics and the flapping of the streams with respect

to the oscillation of the transverse acoustic velocity (u_y'), we derive the acoustic relationship between p' and u_y' and thereby relate the flapping of the streams with the u_y' in the following paragraphs.

For a closed-closed acoustic boundary in the vertical direction of the test section, the p' is given by

$$p' = A(x) \cos(k_y y) \cos(\omega t) \quad (4.7)$$

And the transverse acoustic velocity is given by

$$u_y' = \frac{k_y A(x)}{\rho \omega} \sin(k_y y) \sin(\omega t) \quad (4.8)$$

where $A(x)$ is the amplitude variation of acoustic pressure in the x -direction, k_y is the wave number in the y -direction, and ρ is density of air.

Therefore p' leads u_y' by a phase of $\pi/2$ in time. The relationship between p' and u_y' at the bottom wall of the test section is derived based on Equation (4.7) and Equation (4.8), and is shown in Figure 4.6.

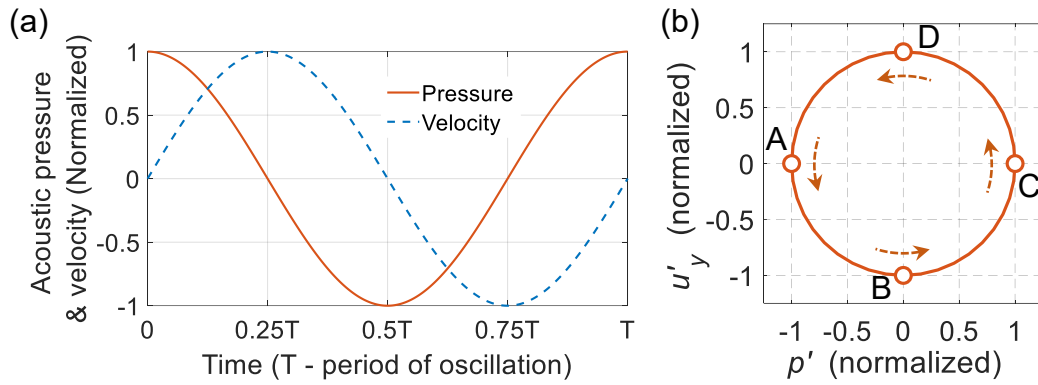


Figure 4.6 : (a) Relationship between p' at the bottom side of the test section and u_y' in time. (b) Phase portrait of the p' and u_y' . The positive velocity is taken in the direction pointing towards top side from bottom side of the test section.

The significant features of the relationship between p' and u_y' are described in Table 4.1.

Table 4.1 : Relationship between p' at the bottom wall of test section and u_y'

Figure 4.6b	$p'_{bottom\ wall\ (y=0)}$	u_y'	Figure 4.5
Point A	Minimum	Zero — approached from positive velocity cycle	Frame I
Point B	Zero	Minimum (i.e. maximum magnitude of velocity in the negative y-direction)	Frame II
Point C	Maximum	Zero — approached from negative velocity cycle	Frame III
Point D	Zero	Maximum	Frame IV

The roll-up of fuel-air mixture (stream-1) into the combustion products at the wake of top flame holder happens at the end of positive cycle of velocity oscillation (refer Figure 4.7a & Figure 4.5-I) which corresponds to minimum p' and zero u_y' . The positive direction is taken as the direction pointing from bottom to top. On the other hand, the roll-up of fuel-air mixture (stream-1) into the wake of middle flame holder happens at

the end of negative cycle of velocity oscillation (refer Figure 4.7b & Figure 4.5-III) which corresponds to maximum p' and zero u_y' .

Similarly, the stream of fuel-air mixture issued out of the passage between middle and bottom flame holders (denoted as stream-2 in Figure 4.7a) flaps in phase with the stream-1. The in-phase flapping of two streams is induced by the in-phase oscillation of u_y' along the height of the test section for a first transverse mode. The asymmetric roll up of flame is due to the asymmetric placement of flames with respect to the streams. In the positive cycle of velocity oscillation, the stream-1 rolls into the wake containing combustion products and the stream-2 in phase with stream-1, rolls away from the bottom flame holder and into the wake of middle flame holder as shown in Figure 4.7, resulting in asymmetric flame structure.

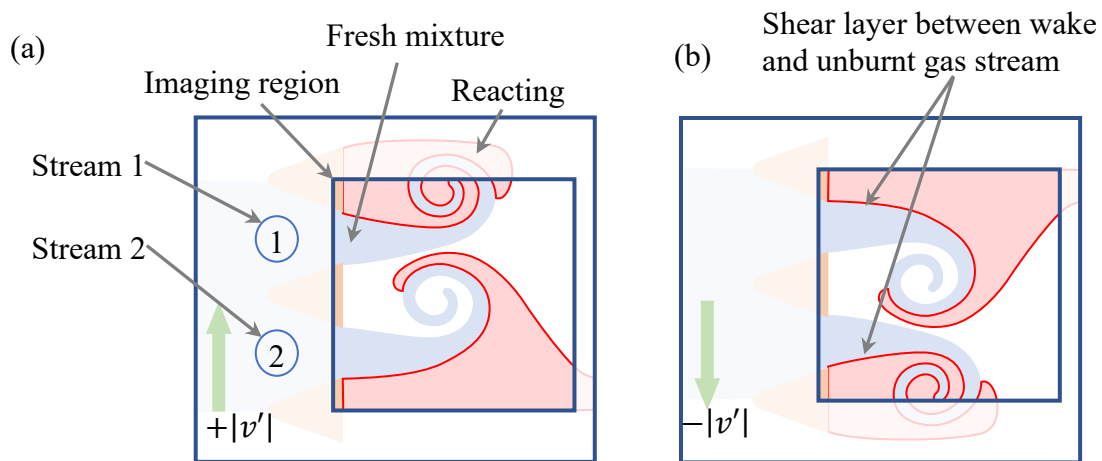


Figure 4.7 : Conceptual sketch describing the in-phase flapping of stream-1 and stream-2 with respect to acoustic velocity direction, resulting in asymmetric flame structure. Flame structure during (a) positive transverse velocity (b) negative transverse velocity.

To understand the phase relationship between p' and local \dot{q}' , we derived time series of unsteady heat release rate from the high-speed images corresponding to the bottom flame holder. The high-speed images are obtained during sustained thermoacoustic

instability. We summed the intensity values of a line of 320 x 10 pixels (vertical lines in Figure 4.10a) from each frame to obtain a time series representing the local \dot{q}' corresponding to different axial locations of 25, 50, 75, 100, 125 and 150 mm from the flame holder trailing edge. We plotted the time series of \dot{q}'_{bottom} and \dot{q}'_{top} obtained at an axial location of 25 mm, along with p' at the bottom wall of the test section in Figure 4.8a. The time series of the mentioned variables are filtered between 1000 and 1500 Hz and are plotted in Figure 4.8b to graphically show the phase relationship among the variables. In Figure 4.8b, the \dot{q}'_{bottom} and \dot{q}'_{top} are oscillating out of phase to each other, and \dot{q}'_{bottom} and p' are oscillating approximately in phase.

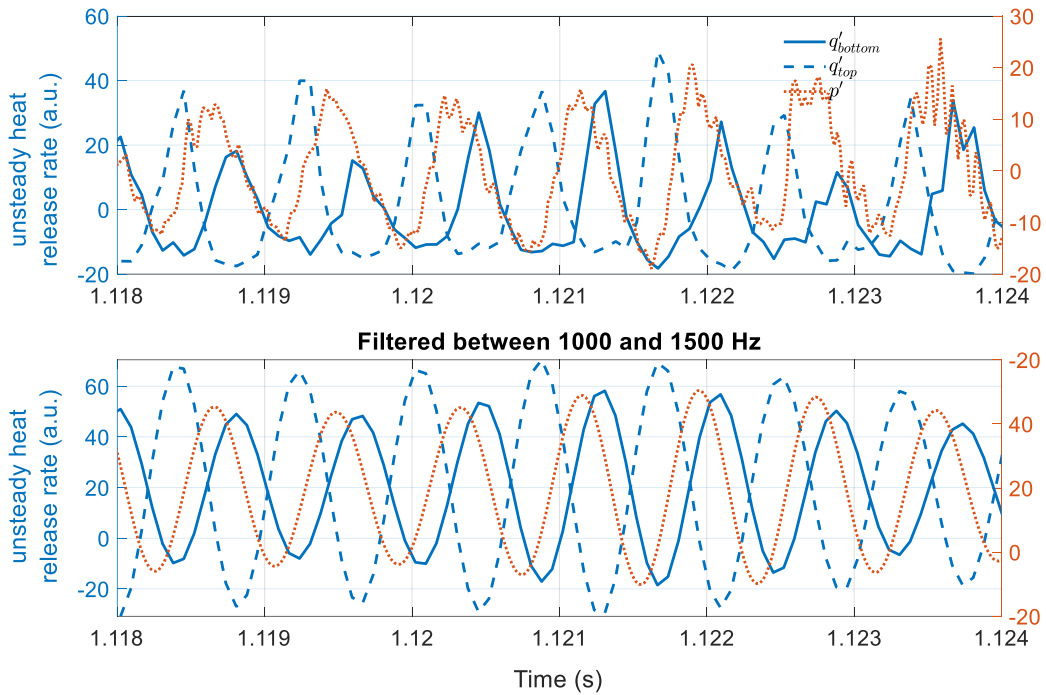


Figure 4.8: Time series of unsteady heat release rate between top and bottom flame holder obtained from high-speed images (at 25 mm) along with acoustic pressure.

The amplitude spectrum of the time series of p' , \dot{q}'_{top} , and \dot{q}'_{bottom} is shown in Figure 4.9. The dominant frequency of oscillations is 1207 Hz and is same for all of the mentioned variables. The roll-up of the shear layer corresponding to the top flame

holder is generally observed to curl more than the roll-up corresponding to the bottom flame holder. The difference in the extent of roll corresponding to the top and bottom flame holder is reflected in the magnitude of oscillation of \dot{q}'_{top} and \dot{q}'_{bottom} (\dot{q}' at 25 mm from trailing edge of flame holder).

The correlation and phase between the p' and local \dot{q}' are interpreted using the wavelet coherence plots in Figure 4.10 (b) – (g). The near field of the flame holder \dot{q}' is highly correlated with p' between the frequency range of 1000 and 2000 Hz and the correlation is continuous in time (refer Figure 4.10 (b)). Whereas, the correlation reduces with downstream distance from the flame holder. Such loss in correlation appears with lower magnitude of wavelet coherence and intermittently correlated regions in the wavelet coherence plots (apparent in Figure 4.10 (g)). The phasor angle of the correlated region in the mentioned frequency range is approximately 35° for $x = 25$ mm and are aligned in time. The phasors in the correlated region rotate anti-clockwise with downstream distance from the flame holder (refer Figure 4.10 (b) – (g)). The signals become out of phase at about a downstream distance of 85 mm.

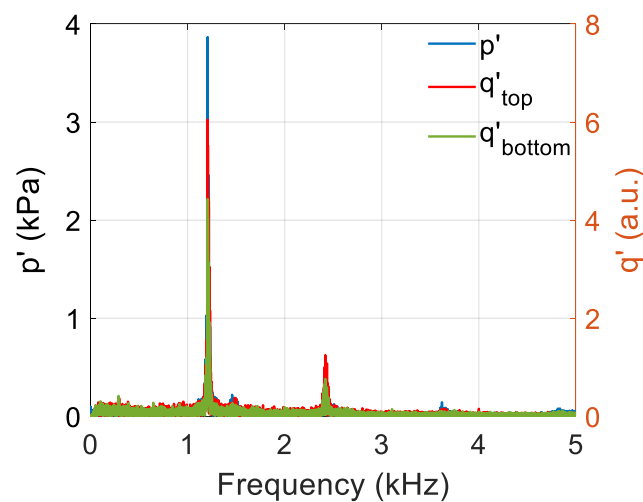


Figure 4.9 : Amplitude spectrum of acoustic pressure, \dot{q}'_{top} and \dot{q}'_{bottom} .

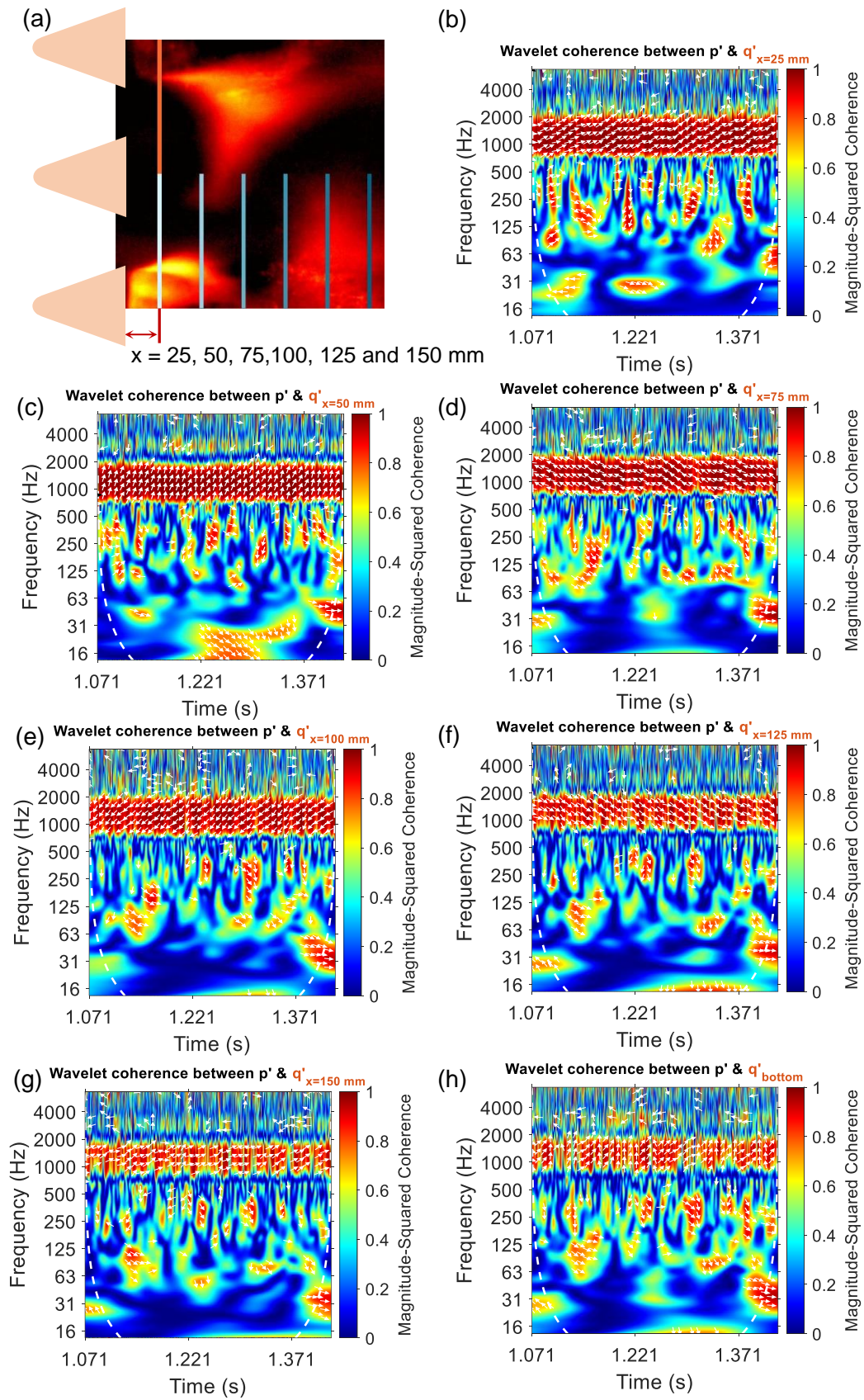


Figure 4.10 : (a) Schematic depicting the axial locations where time series of local \dot{q}' is derived from high-speed images. (b) – (g) Correlation and phase between p' and local \dot{q}' shown using wavelet coherence plots

4.3. SPATIO-TEMPORAL ANALYSIS OF FLAME DYNAMICS:

We converted the spatio-temporal variation of unsteady heat release rate to spatio-temporal variation of the amplitude and phase corresponding to the oscillations of the \dot{q}' . We constructed the time series of \dot{q}' corresponding to each pixel of the high-speed images and converted it to instantaneous amplitude and phase using Hilbert transform. The phase of time series of \dot{q}' of each pixel is subtracted from the phase of acoustic pressure measured at the bottom side of the test section. We then averaged over time the spatio-temporal variation of amplitude and phase of unsteady heat release rate to obtain a time-averaged amplitude and phase (phasors) distribution of \dot{q}' (refer Figure 4.11). In shaded regions of Figure 4.11, we observe aperiodic fluctuations in the local heat release rate, due to absence of flame in the wake of the middle flame holder.

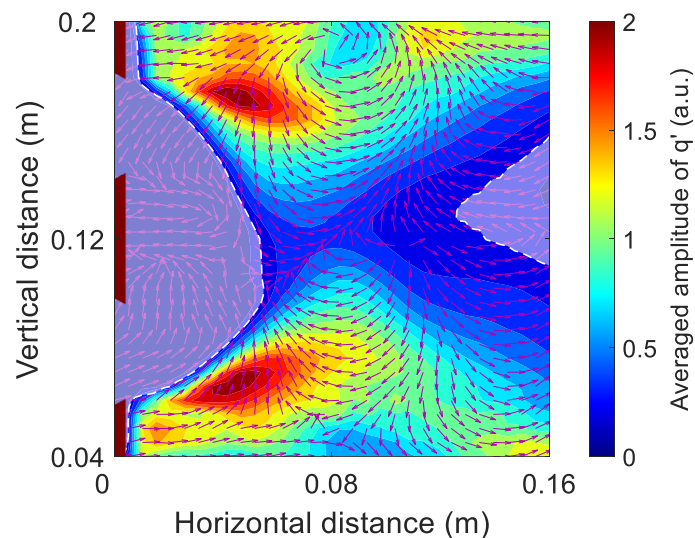


Figure 4.11 : Time-averaged amplitude and phase of unsteady heat release rate obtained during thermoacoustic instability. The amplitude and phase angle are plotted as contour and vectors, respectively. The shaded region denotes the region without flame.

We observe the highest amplitude of \dot{q}' at the oscillating shear layer downstream of separation point of the flame holder (red patches in Figure 4.11), and not necessarily at the location of flame roll-up which is observed downstream of middle flame holder. In

the sequence of images of OH* emissions (Figure 4.5), higher values of intensity are observed at the mentioned shear layer rather than at the location of roll-up of flame. We observed phasors from the bottom and top half of the image point in opposite directions in the corresponding locations. The phasors in opposite directions indicate the out-of-phase oscillation of \dot{q}' between the bottom and top half of the test section.

According to Rayleigh criterion, driving of thermoacoustic instability occurs when the phase difference between acoustic pressure and unsteady heat release rate ranges between $-\pi / 2$ and $+\pi / 2$, which correspond to phasors pointing in the positive x-direction. In Figure 4.11, the phasors in the wake of the bottom flame holder points in the positive x-direction suggesting acoustic driving and gradually rotates to the negative x-direction as we move downstream in the flow direction to the region of flame roll-up. To understand the regions of acoustic power generation, we plotted contours of Rayleigh index along with the phase difference between \dot{q}' and p' in Figure 4.12a. We computed Rayleigh index correcting for the variation of acoustic pressure along the height corresponding to the first transverse mode. The normalized variation of amplitude of p' and the variation of phase along the height of the imaging region ranging from 0.04 to 0.2 m, is shown in Figure 4.12b & Figure 4.12c, respectively. We find it interesting that the region of flame roll-up has a damping effect on the thermoacoustic instability as suggested by the negative Rayleigh index (blue patches in Figure 4.12a) and is also indicated by the vectors of phase difference pointing in the negative x-direction. The near wake of the bottom flame holder act as source of acoustic energy as the ignition of fuel-air mixture in the wake occurs at the pressure maximum. Though the area and flame intensity of the damping region (flame roll up region) is comparable to that of the wake of the bottom flame holder (acoustic source), it is the proximity of

the damping region close to the nodal line of the first transverse mode, that decreases the Rayleigh index to a lower value for the mentioned region. Therefore, the net Rayleigh index is positive and drives the thermoacoustic instability. As the flame roll-up convects downstream, it becomes in-phase with the next positive cycle of pressure oscillation and shows a positive Rayleigh index in Figure 4.12a (phasors pointing in the positive x-direction).

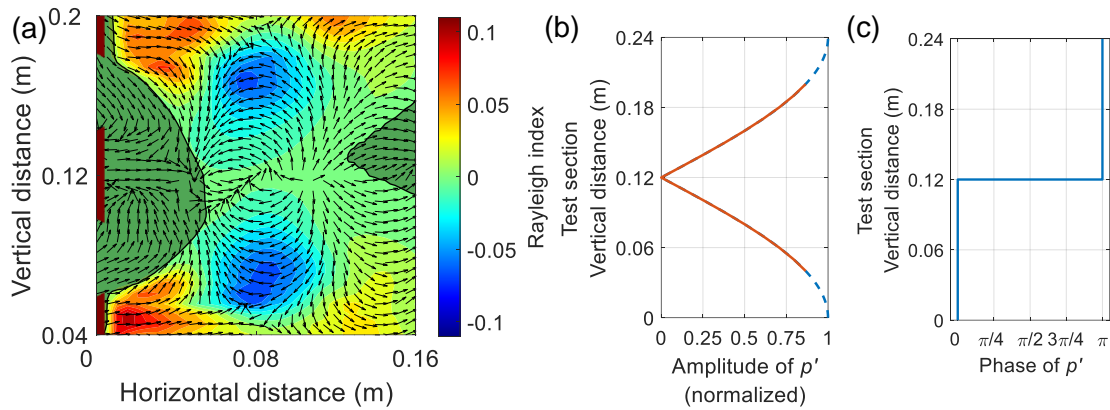


Figure 4.12 : (a) Rayleigh index obtained over a time period of integration of 2 seconds and is plotted as contours. The vectors denote the phase difference between the unsteady heat release rate and the acoustic pressure. (b) Variation of amplitude of p' along the height of the test section for the first transverse mode. The dotted line is in the region of the test section that is outside the imaging region. (c) And corresponding phase of p' along the height of the test section

4.4. PROPAGATION SPEED OF INTENSITY FLUCTUATIONS:

We explain the basis of the patterns observed in the phasor field (refer phasors of Figure 4.12a) using the computed propagation speed of intensity fluctuations of OH* emissions. We explain in this section about the propagation speed of intensity fluctuations of OH* emissions and the computation method. We reiterate here from Section 4.2, the salient features of the flame dynamics during thermoacoustic instability. We observe in the high-speed images of the flame that a periodic rise in the

intensity of OH* emissions in the shear layer of the top flame holder because of periodic ignition and extinction of flame at the wake of the flame holder (refer Figure 4.5). The high-intensity emissions from the shear layer propagates toward the wake of middle flame holder and then the emissions travel downstream. The generation and propagation of the emissions happen periodically during thermoacoustic instability (refer Figure 4.5).

We compute the propagation speed of the intensity fluctuations corresponding to each pixel, based on the spatial variation of phase of intensity fluctuations. The propagation speed mentioned here is similar to that of wave propagation speed also known as phase speed. For example, the propagation speed of acoustic wave is known as sound speed. In the present case, it is the fluctuations of intensity of OH* emissions generated at the shear layer and the same propagates downstream. The propagation speed of fluctuations can be computed from the relation $u_x = \frac{2\pi f_0}{d\phi/dx}$, f_0 is the frequency of oscillation of the disturbance, $d\phi/dx$ is the gradient of phase variation in space. Emerson et al. (2013) studied the response of bluff body stabilized flames subjected to transverse acoustic waves. They showed that the transverse acoustic waves excite vortical structures that convect downstream. They used the mentioned relation to estimate the propagation speed of wrinkles in the flame edge which are perturbed by the vortical structures. They found that the wrinkles in the flame propagate downstream at nearly constant speed. We extend the relation to 2D field of intensity fluctuations with gradients of phase defined in two directions ($d\phi/dx, d\phi/dy$) and the corresponding propagation velocity in the two directions (u_x, u_y). Such a velocity field provides the local propagation speed of the intensity fluctuations and helps us to understand the trajectory of the OH* emissions in the spatial domain.

We compute the propagation speed of the intensity fluctuations of OH* emissions obtained from the high-speed images of the flame dynamics during thermoacoustic instability. We compute the instantaneous phasor field by applying Hilbert transform to the time series of the intensity fluctuations corresponding to each pixel of the images. We filter the time series of the intensity fluctuations for the frequencies between 600 and 2000 Hz before using Hilbert transform in order to obtain the phase corresponding to dominant oscillation frequency. For computing the propagation speed using the relation mentioned in the previous paragraph, the gradients of the phase are approximated using first order discretization in space and averaged over time to compute the propagation speed corresponding to each pixel. Magnitude of the computed propagation velocity is plotted as contours in Figure 4.13, overlaid with propagation direction as vectors. We observe that the magnitude of propagation velocity of intensity fluctuations reaches a maximum of 390 m/s (a small patch) in the flame roll-up region as seen in Figure 4.13. The estimated velocity of unburnt mixture at the trailing edge of the flame holder is 420 m/s and the corresponding sound speed is 575 m/s. The maximum propagation speed is in the order of the flow speed of unburnt mixture.

The intensity fluctuations propagate at different speeds and at different directions in the spatial domain depending on its location in the domain. The propagation speed of intensity fluctuations should not be confused with the velocity of the flow. The distribution of propagation speed of intensity fluctuations is specific to the underlying instantaneous flow field during thermoacoustic instability.

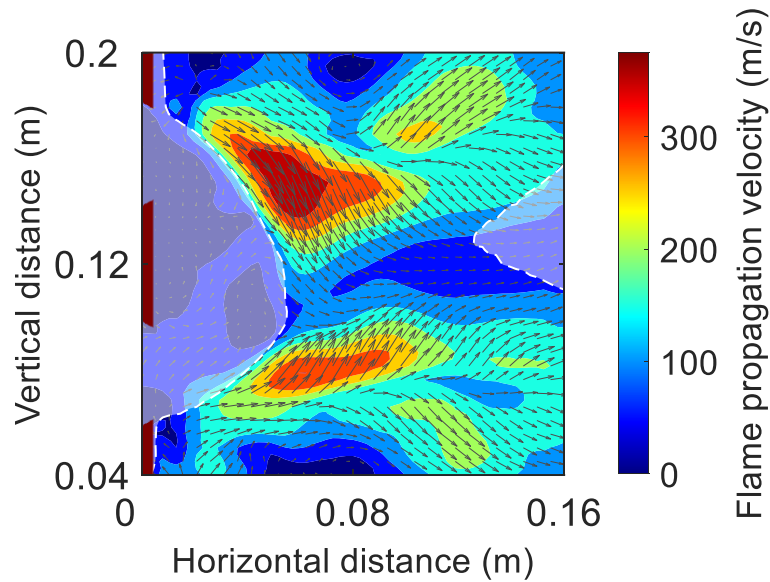


Figure 4.13 : Magnitude of propagation velocity of intensity fluctuations is plotted as contours overlaid with propagation velocity vectors.

We compute streamlines using the field of propagation velocity of intensity fluctuations starting at different locations in the spatial domain and is shown in Figure 4.14. We observe two vortex-like structures downstream of top and bottom flame holders. They show circular motion of intensity fluctuations and suggest a probable vortex in the underlying flow field. We observe two seemingly unstable manifolds about which the intensity fluctuations propagate in diverging directions (marked with red line in Figure 4.14). We find vectors pointing in all directions, suggesting the source of intensity fluctuation at the immediate downstream of the top flame holder (marked with pink circle in Figure 4.14).

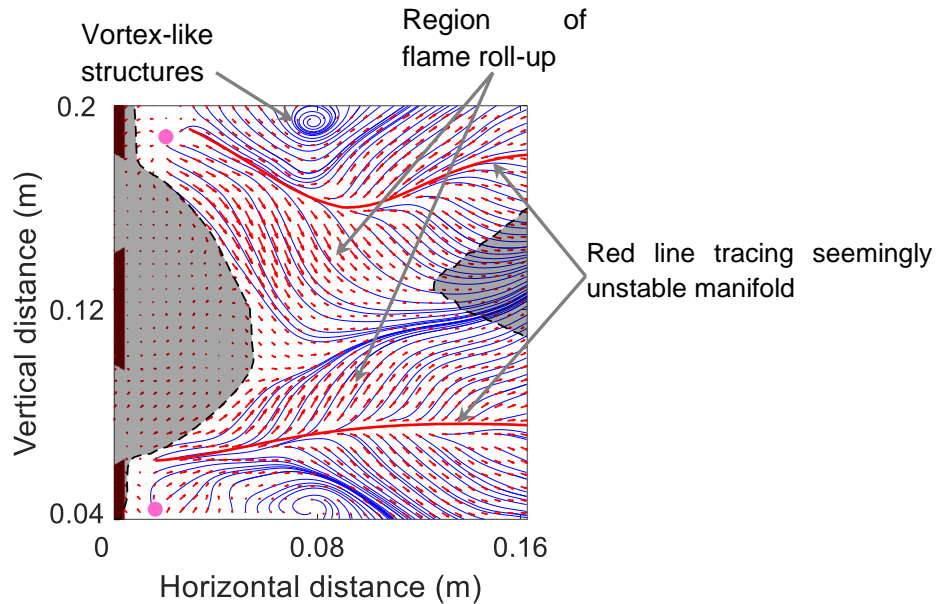


Figure 4.14 : Stream lines drawn using the vectors of propagation velocity of intensity fluctuations.

To understand the patterns observed in the phasor field (refer Figure 4.11 reproduced in Figure 4.15b), we identified four location corresponding to different phasor orientations (refer B1 – B4 in Figure 4.15b) and traced them back to the vicinity of the flame holder (refer A1 – A4 in Figure 4.15b) through the streamlines passing through the identified points. The streamlines were computed using the field of propagation velocity of the intensity fluctuations (refer Figure 4.15a). We computed the time taken by the intensity fluctuations to propagate from points A# to points B# by integrating the velocity along the path. The time taken for each path in terms of time period of oscillation are $0.27T$, $0.45T$, $0.79T$ and $1.0T$, refer Figure 4.15a. The same paths are plotted over the time-averaged phasors in Figure 4.15b. The phase of intensity fluctuations at the wake of the bottom flame holder is approximately zero. The phase of intensity fluctuations in the region of B1, B2, B3, and B4 is approximately $\pi / 2$, π , $3\pi / 2$ and 2π , respectively (refer phasor orientations at those locations in Figure 4.15b). The propagation time taken by the intensity fluctuations and the corresponding phase values at the end points of the paths indicate that the patterns of

the phasor plot is dominantly due to the propagation of the intensity fluctuations starting at the vicinity of the flame holders and propagating downstream. A phase vector starting at the immediate wake of the bottom flame holder rotates along the path of a streamlines, as the intensity fluctuations convect along with the flow. The rotation of phasor due to convection of the intensity fluctuations creates regions of in-phase and out-of-phase relation between intensity fluctuations and acoustic pressure, as shown in contour plot of Rayleigh index (Figure 4.12). Therefore, the prime region of source of acoustic power is the wake of the flame holders and region of flame roll-up merely acts as damping source in this flame dynamics due to propagation time taken by the intensity fluctuations to reach the roll-up region.

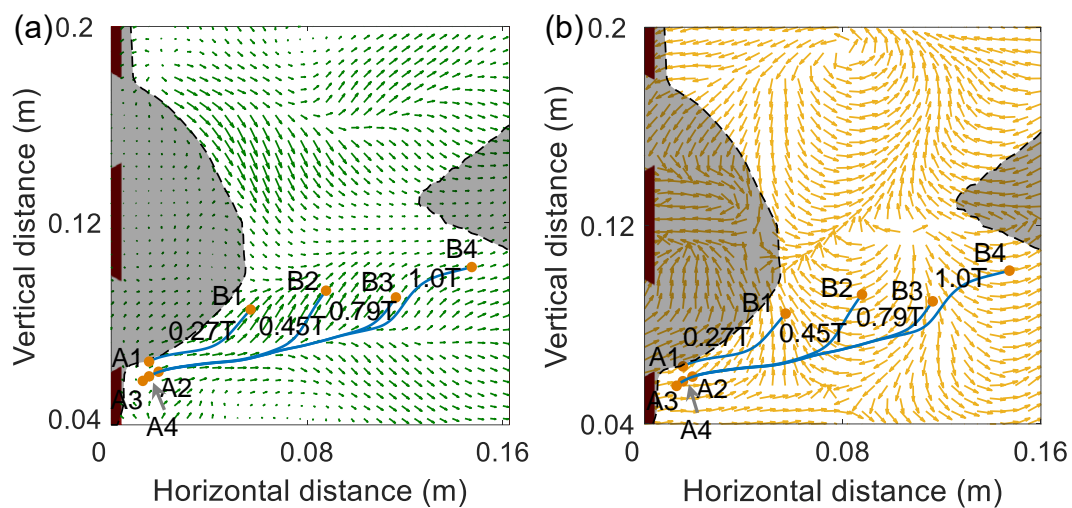


Figure 4.15 : Paths traced by intensity fluctuations starting from four points in the vicinity of the bottom flame holder and reaching different regions of the pattern formed by the phasor plot. The streamline paths are overlaid on the vectors of (a) propagation velocity of intensity fluctuations, (b) phasors obtained between intensity fluctuations and acoustic pressure.

4.5. SUMMARY

We measured global unsteady heat release rate using PMT and corresponding p' during the transition to thermoacoustic instability. As the Reynolds number is increased at a

rate of 335 s^{-1} , the acoustic pressure transitions to sustained oscillations via bursts of periodic oscillations. The plots of wavelet coherence obtained between p' and \dot{q}' provides information on the common spectral power which is an indicator of coupling strength and the phase relationship between them (known as phasors). We observe that the coupling strength transitions from weak to strong coupling during the transition to thermoacoustic instability via bursts of high coupling strength. We observe that the bursts of high coupling strength do not have the phasors aligned among them. As the number of bursts of high coupling strength increases, we observe an increase in the alignment of the phasors and eventually all of the phasors align, in the present case, to the right side. Secondly, we observe the state of bursts of high coupling strength persists even after the acoustic pressure transitioned from a state of bursts of oscillations to a state of sustained oscillations. The transition dynamics of unsteady heat release rate appears to be different from that of the acoustic pressure and does not vary proportional to the acoustic pressure. The increase in the cross-correlation coefficient between the probabilities of recurrence ($P(\tau)$) of p' and \dot{q}' can dominantly be attributed to the changing dynamics of \dot{q}' which is evident in the plots of $P(\tau)$. The p' attains a state of periodic oscillations (as observed in RPs and $P(\tau)$ plots) at a lower Reynolds number than the \dot{q}' and therefore, much of the increase in the cross-correlation coefficient between the $P(\tau)$ of p' and \dot{q}' is because of the coupling of \dot{q}' with p' .

We captured the flame dynamics during the transverse mode thermoacoustic instability using high-speed camera. The flames sustained by the recirculation zones of the top and bottom flame holders get convected downstream and roll up periodically in an out-of-phase manner. The production of acoustic energy occurs at the recirculation zone of the flame holders due to periodic extinction and ignition of the mixture in the recirculation

zone. The region of flame roll-up in the vortex acts as an acoustic damper due to the convection time taken by the ignited mixture at the recirculation zone to reach the region of flame roll up. A phasor field is obtained for the unsteady heat release rate and the pattern observed in the phasor field is shown to be due to different time taken by the reacting mixture to convect to different regions in the test section.

CHAPTER 5

CONCLUSIONS AND SCOPE FOR FUTURE WORK

Combustors with bluff body stabilized flames are used in gas turbine afterburners and ramjets. In such combustors, thermoacoustic instability particularly transverse mode instability is a cause of concern. On the other hand, existing literature on the subject pertains to 1950s and hardly any literature is available in the recent decades on the self-excited transverse thermoacoustic instability with bluff body stabilized flames. The subject of thermoacoustic instability studied in other types of combustors has advanced significantly over the period with the advent of laser diagnostics and computational tools. Interesting developments have happened in the understanding of fundamental behaviour of thermoacoustic instability with the subject being looked at from the perspective of nonlinear dynamical systems and complex systems approach. Therefore, we set up experiments to simulate self-excited transverse thermoacoustic instability and looked at it with latest tools.

The attributes of rate-induced tipping or R-tipping have been studied for a long time in climate sciences in the context of global warming and its catastrophic consequences which is being accelerated with the increased rate of pollutant emissions. Recently, Wieczorek et al. (2011) and Ashwin et al. (2012) identified R-tipping in a model of the climate system. They defined the rate induced tipping as a means of tipping and showed it in a theoretical modelling of the climate system. In our experiments, we observed the onset of thermoacoustic instability to be erratic for the same operating conditions. Later when we introduced a means to control the variation of the control parameter at a fixed

rate, we observed that the onset of thermoacoustic instability depended on the rate of change of Reynolds number. The transition to thermoacoustic instability from combustion noise is characterized with the rate of change of Reynolds number as a parameter and the transition happens via intermittency with increasing rate of change of Reynolds number. We infer from our experiments that the region of stable operation of a combustor in the stability map reduces with a higher rate of change of inlet parameters. From our results, it appears that engine throttling rate should be a parameter in obtaining thermoacoustic stability map of combustors. In defining a safe operating boundary of a combustor with respect to thermoacoustic instability, we suggest that the engine has to be subjected to highest throttling rate anticipated to ensure the absence of thermoacoustic instability in the combustor. Further, a designer can extend the safe operating boundary by defining a critical rate of throttling, below which it is safe to operate the engine at these extended regions of the stability map.

How does the flame dynamics couple with acoustic field in the flame zone? the question is one of the largely studied aspect of thermoacoustic instability. We measured global unsteady heat release rate using PMT and corresponding p' during thermoacoustic instability. We infer from the contour plots of magnitude-squared wavelet coherence the dynamics of coupling strength between p' and \dot{q}' . We observe that the bursts of high coupling strength do not have the phasors aligned among them. As the number of bursts of high coupling strength increases, we observe an increase in the alignment of the phasors and eventually all of the phasors align, in the present case, to the right side. Secondly, we observe the state of bursts of high coupling strength persists even after the acoustic pressure transitioned from a state of bursts of oscillations to a state of sustained oscillations. The dynamics of unsteady heat release rate does not vary

proportional to the acoustic pressure. Such an observation raises question on the validity of experiments of forced responses of flame to explain the transition dynamics of self-excited thermoacoustic instability. We also observe a steep raise in a statistical measure called cross correlation of probability of recurrence during the transition to thermoacoustic instability, whereas the RMS of p' shows a gradual increase with increasing Reynolds number. The CPR suggests a locking behaviour after the transition to strong coupling, irrespective of variations in the p'_{rms} .

Further, we captured the flame dynamics using high-speed camera. We observe that alternate vortex shedding and the associated dynamics of unsteady heat release rate is responsible for the sustenance of transverse thermoacoustic instability. Though the mechanism is the vortex shedding, we show that the vortex roll-up itself does not generate acoustic energy. It is the flame ignition and extinction at the immediate wake of the flame holder that drives the thermoacoustic instability. The suppression techniques devised for disrupting the acoustic sources, cannot be misled by the vortex-flame roll up and requires a thorough investigation before implementing such techniques. Also, we show that the patterns of the phasor field are a result of convection of reacting particles from the immediate wake to different zones of the combustor. Such an understanding can improve the modelling of the unsteady heat release rate of the thermoacoustic system.

5.1. SCOPE FOR FUTURE WORK

We reported for the first time the rate dependent transition in a practical combustion system. The model afterburner which best captures the gas turbine afterburner in both the geometry as well as operating conditions. Such a model afterburner exhibits

nonlinear dynamics such as rate dependent transition to thermoacoustic instability and intermittency. We expect that the typical afterburner has several other nonlinear dynamical features which are yet to be uncovered in the transition to thermoacoustic instability, particularly the aspects of synchronization theory and complex network approach.

We captured the flame dynamics using high-speed camera during limit cycle oscillations and there is plenty of scope for studying the flame dynamics during the transition to thermoacoustic instability. We observed in the analysis of $P(\tau)$ during weak coupling, the p' showed a high probability of recurrence, whereas the \dot{q}' was closer to a chaotic behaviour. During the transition from weak to strong coupling, the major difference was observed in the $P(\tau)$ plots of \dot{q}' rather than in the p' . High-speed imaging during such states will help to explain the mechanism of the transition to thermoacoustic instability along with the analysis based on synchronization theory and complex networks.

We show the effect of fuel injection direction on the occurrence of thermoacoustic instability in Appendix 'A'. It requires further investigation during thermoacoustic instability to understand the mechanism causing it and that the suppression during inline injection is due to spray's response to acoustic field or is it due to the change in the fuel distribution at the location of the flame.

APPENDIX ‘A’

ACOUSTIC FIELD IN THE MODEL AFTERBURNER AND EFFECT OF ORIENTATION OF FUEL INJECTION ON TRANSVERSE THERMOACOUSTIC INSTABILITY

A. 1. ACOUSTIC FIELD IN THE MODEL AFTERBURNER

We observed that the thermoacoustic instability is a transverse mode instability with out-of-phase oscillation of pressures measured in transducers 1 and 10, shown in Figure 2.6. Also, we observe that the acoustic field upstream of the flame holders retain the transverse mode pressure variation with out-of-phase oscillation of pressure measured in transducers 4 and 9, shown in Figure 2.6.

We plotted the variation of amplitude and phase of acoustic pressure along the length of the test section upstream of the flame holders in Figure A.1. The transducer at the leading edge of the flame holders is taken as the origin for the axial direction and the remaining transducers are denoted with respect to this origin. The region of measurement of acoustic pressure upstream of flame holders contains fuel injectors and the acoustic medium is a heterogenous mixture of air, fuel droplets and fuel vapour.

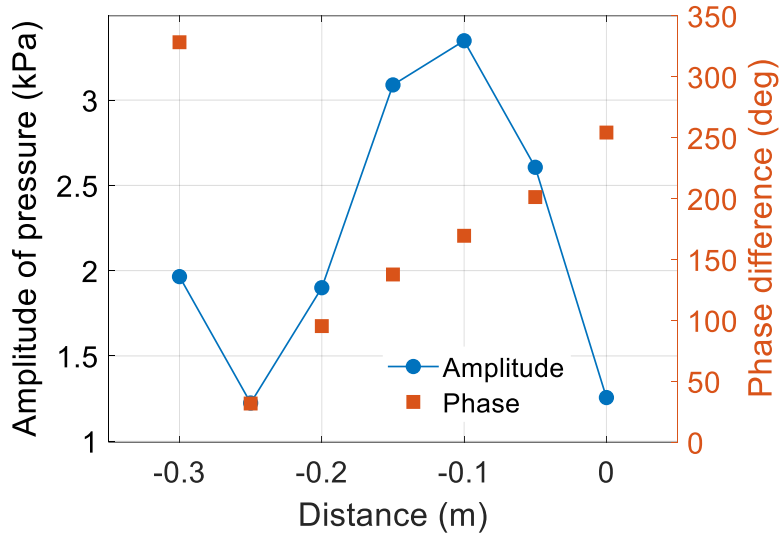


Figure A.1 : Variation of amplitude and phase of acoustic pressure obtained in the region upstream of flame holders corresponding to the transducers numbered as 2 to 8 in Figure 2.6.

We observed that the phase of the acoustic pressure along the length of the test section upstream of flame holder has a positive slope indicating the acoustic field dominated by left-running acoustic waves. Such an acoustic field suggests that the sound is being radiated from right to left which is expected as the flame is the source of sound, radiating towards the plenum connected upstream of the test section. We observed that the amplitude variation of acoustic pressure indicates a partially reflecting longitudinal mode set up upstream of the flame holder with a ratio of $|\hat{p}_{max}| / |\hat{p}_{min}| \sim 2.73$. Therefore, the acoustic field upstream of flame holder is a two-dimensional field with pressure variation in the longitudinal and transverse direction. The two-dimensional acoustic field is of the form as shown in Equation (A.1).

$$p' = (Ae^{ik_x x} + Be^{-ik_x x})(Ce^{ik_y y} + De^{-ik_y y})e^{i\omega t} \quad (\text{A.1})$$

where, k_x and k_y are the wave numbers corresponding to the horizontal and vertical direction with respect to the test section, respectively. For a hard wall boundary condition at $y = 0$ and $y = 0.24$ m, the test section creates a closed-closed acoustic boundary in the height direction. The corresponding wave length of the first transverse mode is $\lambda_y = 0.48$ m and $k_y = 13.1$ m⁻¹. The closed-closed boundary in the height direction, reduces the amplitude equation of the pressure to that shown in Equation (A.2).

$$\hat{p} = A(e^{ik_x x} + R e^{-ik_x x}) \cos(13.1y) \quad (\text{A.2})$$

where, R is the reflection coefficient at the inlet of the test section. At $y = 0$ corresponding to the bottom wall of the test section, the amplitude of acoustic pressure is of the form shown in Equation (A.3) and resembles the acoustic pressure variation of a pure longitudinal mode. The complex constants in Equation (A.3) is then re-written with amplitude and phase of those constants in Equation (A.4). Therefore, the constants a , $|R|$, k_x and $\Delta\phi$ in Equation (A.4) can be obtained by fitting the amplitude equation of an impedance tube to the amplitude distribution obtained from experiments. The amplitude equation of an impedance tube is given in Equation (A.5).

$$\hat{p}_{y=0} = A(e^{ik_x x} + R e^{-ik_x x}) \quad (\text{A.3})$$

$$\hat{p}_{y=0} = a(e^{ik_x x} + |R|e^{-i(k_x x - \Delta\phi)}) \quad (\text{A.4})$$

$$|\hat{p}|^2 = a^2[1 + |R|^2 + 2|R| * \cos(2k_x x - \Delta\phi)] \quad (\text{A.5})$$

where, a , $|R|$, $\Delta\phi$ and $k_x = 2\pi/\lambda_x$ are amplitude of travelling wave, magnitude of reflection coefficient at the boundary, phase difference and wave number of acoustic pressure field set up in an impedance tube, respectively. We fitted the amplitude equation of impedance tube to the amplitude distribution of acoustic pressure obtained from the experiment as shown in Figure A.2. The constants obtained from the curve fit are provided in Table A.1.

Table A.1 : Constants obtained from curve fit to the amplitude distribution of acoustic pressure.

a	2189 Pa
$ R $	0.53
$\Delta\phi$	-2.59 radians
λ_x	0.55 m

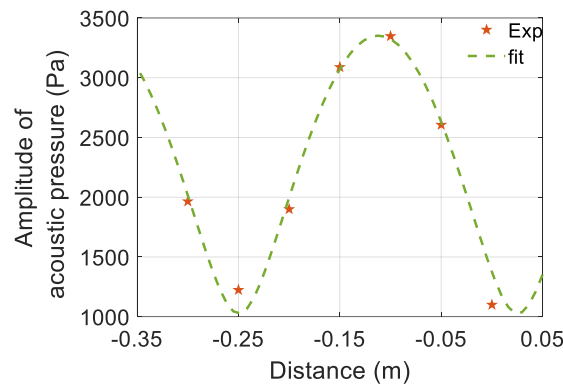


Figure A.2 : Fit of the amplitude equation of impedance tube to the amplitude distribution of acoustic pressure obtained from the experiment.

We speculate that the low value of reflection coefficient for an open-end acoustic boundary, is due to the acoustic leakage through the gaps in the flange connecting the plenum and the test section. We calculated the frequency components in the x and y

direction, and the speed of sound using the Equations (A.6), (A.7) and (A.8), respectively and the calculated values are provided in Table A.2.

$$f_x^2 + f_y^2 = f^2 \quad (\text{A.6})$$

$$f_x = \frac{f}{\sqrt{1 + (\lambda_x/\lambda_y)^2}} \quad (\text{A.7})$$

$$c = \frac{2\pi f}{\sqrt{k_x^2 + k_y^2}} \quad (\text{A.8})$$

where, f_x and f_y are frequency components in the vertical and longitudinal direction, c is the average speed of sound and f is frequency of oscillation of acoustic pressure.

Table A.2 : Frequency components and sound speed.

f	1471 Hz (From experiment)
f_x	967 Hz
f_y	1108 Hz
c	532 m/s

The final form of the acoustic pressure in the region upstream of flame holders is provided in Equation (A.9).

$$\hat{p} = 2189(e^{11.4ix} + 0.53e^{-i(11.4x+2.6)}) \cos(13.1y) \quad (\text{A.9})$$

We further calculated the magnitude of acoustic velocity from the linearized momentum equation which are provided in Equation (A.10) and (A.11).

$$\hat{u}_x = \frac{-1}{i\bar{\rho}\omega} \frac{\partial \hat{p}}{\partial x} \quad (\text{A.10})$$

$$\hat{u}_y = \frac{-1}{i\bar{\rho}\omega} \frac{\partial \hat{p}}{\partial y} \quad (\text{A.11})$$

$$\hat{u}_x = -4.42(e^{11.4ix} - 0.53e^{-i(11.4x+2.6)}) \cos(13.1y) \quad (\text{A.12})$$

$$\hat{u}_y = -5.07i(e^{11.4ix} + 0.53e^{-i(11.4x+2.6)}) \sin(13.1y) \quad (\text{A.13})$$

We plotted the magnitude of longitudinal velocity in Figure A.3a obtained using Equation (A.12) for the region upstream of flame holders. The origin of the longitudinal axis corresponds to the leading edge of the flame holders and the inlet of the constant area test section is at a distance of 0.52 m upstream of the leading edge of the flame holders. We observed that the magnitude of longitudinal velocity is not uniform in the vertical axis contrary to that expected in a pure longitudinal mode and reaches zero velocity in the mid-height of the test section. The magnitude of longitudinal oscillation velocity reaches a maximum of 35 m/s at the top and bottom walls of the test section. We observe in Equation (A.12) for longitudinal velocity having a cosine dependence in the vertical direction and therefore, has an out-of-phase relationship of longitudinal velocity at the top and bottom half of the test section.

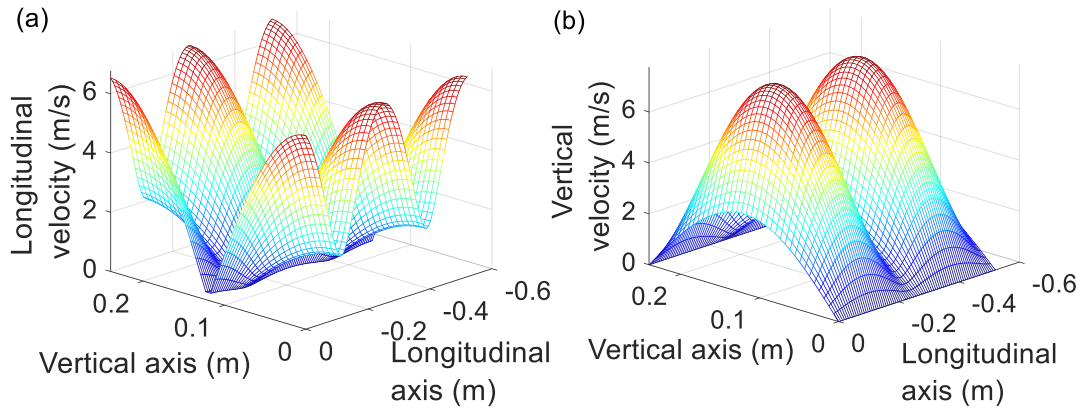


Figure A.3 : Longitudinal oscillation velocity field in the region upstream of flame holders.

We plotted the magnitude of vertical velocity in Figure A.3b obtained using Equation (A.13) for the region upstream of flame holders. As observed in the longitudinal velocity field, the vertical velocity field shows variation in the longitudinal direction and reaches zero velocity at the top and bottom walls of the test section. The region upstream of flame holders have complex acoustic velocity field with maximum vertical velocity at the mid-height of the test section and maximum longitudinal velocity at the top and bottom walls of the test section. We plotted vectors of instantaneous acoustic velocity in Figure A.4 and the whole pattern moves to the left with increasing time. The cross-stream fuel sprays are positioned at an axial location of 130 mm upstream of flame holders and are marked as three dots in Figure A.4. The cross-stream sprays are exposed to magnitudes of oscillation velocity as high as 8 m/s, is a potential source of equivalence ratio fluctuations.

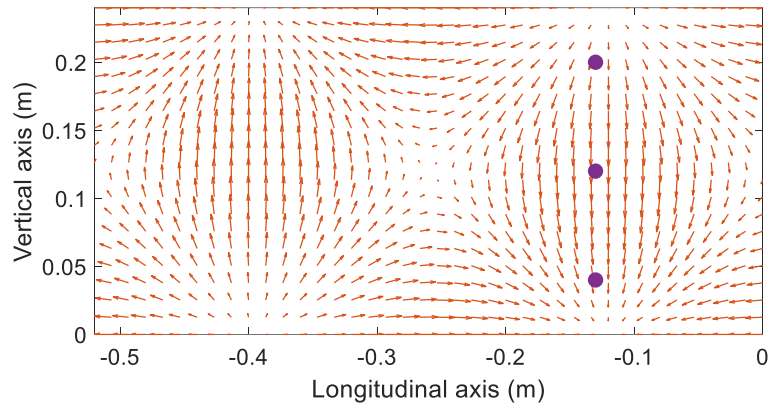


Figure A.4 : Instantaneous plot of vectors of acoustic velocity in the region upstream of flame holders. The velocity pattern moves with time. Three dots represent the location of fuel injectors. The origin in the longitudinal axis represents the leading edge of flame holders.

A. 2. EFFECT OF ORIENTATION OF FUEL INJECTORS ON TRANSVERSE THERMOACOUSTIC INSTABILITY

We conducted experiments by changing the direction of fuel injection of all the injectors in the test setup and studied the effect on transverse thermoacoustic instability. A schematic of the fuel injector orientations in the test setup is shown in Figure A.5 All of the test results report till this point were results of experiments conducted with transverse fuel injection which is chosen to simulate the fuel injection orientation typically used in gas turbine afterburner. The p' is measured at the bottom wall of the test section (transducer 1) as shown in Figure 2.6. We increased the Reynolds number at a rate of 235 s^{-1} with fuel flow rates of preheater and afterburner maintained at 26 and 41 lph, respectively.

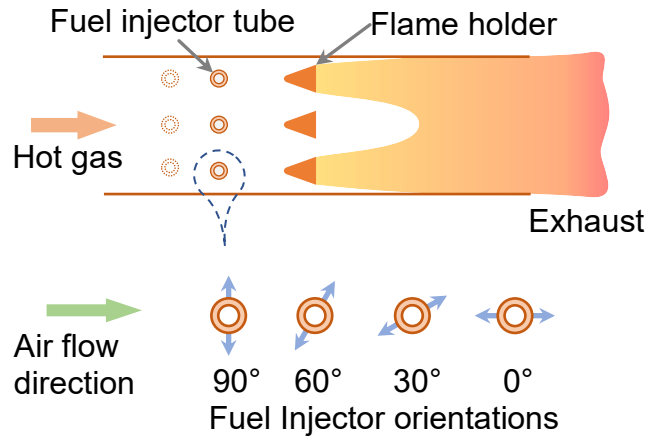


Figure A.5 : Schematic of the fuel injector orientations used for all the injectors, starting from transverse injection to injection in line with the flow direction. The effect of the injector orientation on transverse thermoacoustic instability is studied.

We have plotted the variation of RMS of p' with respect to the flow Reynolds number in Figure A.6. We observe in Figure A.6 that the onset of screech occurs earlier or at a lower Reynolds number with decreasing angle of injection, except for the in-line injector configuration. The screech induced blow out is marked by a sudden drop in p'_{rms} below a value that is observed before the onset of screech (refer Figure A.6). we observe that the screech induced blow out is delayed i.e., it occurs at a higher Reynolds number with decreasing the angle of fuel injection. We find that the thermoacoustic instability is stable for a wider range of Reynolds number with decreasing angle of injector orientation. We find it interesting to note that the occurrence of screech is favoured by the decreasing angle of fuel injector except for the fuel injector orientation which is in line with the flow direction. Contrarily, the screech is completely suppressed with in-line configuration of fuel injection. We are not clear as to the mechanism of such a suppression of thermoacoustic instability with in-line configuration of fuel injector. We surmise that the possible mechanism could be perturbation of fuel spray by the acoustic field set up in the region which does not significantly affect the in-line configuration of fuel injection. Otherwise, it could be the differences in the fuel

distribution caused by the different orientation of the fuel injector which affects the fuel-air ratio at the shear layer and wake of the flame holders.

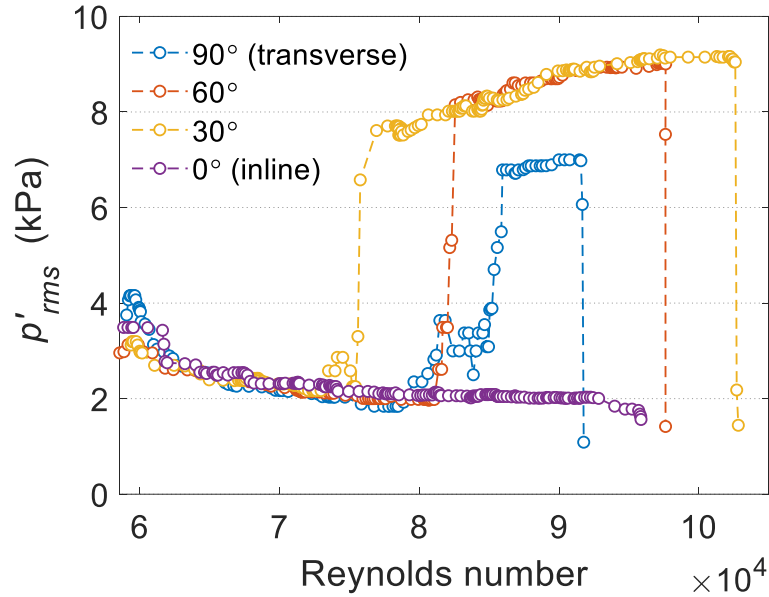


Figure A.6 : The variation of RMS of p' with respect to the flow Reynolds number for different fuel injector orientation such as 90° (transverse injection), 60°, 30°, and 0° (in line with the flow direction).

A. 3. SUMMARY

To understand the acoustic field set up upstream of the flame holders during transverse thermoacoustic instability, we installed several pressure transducers in the upstream portion of the test section and measured the acoustic pressure. We observe that the sound waves generated in the combustion region radiates upstream through the gaps of the flame holders and sets up a partially travelling wave in the upstream portion of the flame holders. Though the inlet of the test section is provided with an abrupt area change at the interface between plenum and the test section, the inlet does not simulate an acoustically open end. The sound is radiated out of the test section at the inlet of the test section as suggested by the direction of the travelling waves. The acoustic field set up in the upstream region is a combined longitudinal-transverse mode which is a

potential source of spray perturbation resulting in fluctuations in the equivalence ratio at the wake of the flame holders.

Further, we studied the effect of orientation of the fuel injectors on the transverse thermoacoustic instability. The onset of screech occurs at a lower Reynolds number with decreasing angle of fuel injection starting from transverse injection i.e. 90° with respect to flow direction. Though the transverse thermoacoustic instability is found to be stable for wider range of Reynolds number with decreasing angle of fuel injection, the thermoacoustic instability is completely suppressed with in-line orientation of the fuel injectors. We surmise that the possible mechanism could be acoustic perturbation of the fuel sprays, otherwise the differences in the fuel distribution due to the different orientation of the fuel injectors.

REFERENCES

- Acharya, V., Emerson, B., Mondragon, U., Brown, C., Shin, D.-H., McDonell, V., and Lieuwen, T. C.** (2011). Measurements and Analysis of Bluff-Body Flame Response to Transverse Excitation. *Volume 2: Combustion, Fuels and Emissions, Parts A and B*, 60(54624), 301–309. <https://doi.org/10.1115/GT2011-45268>
- Amaral, L. A. N., and Ottino, J. M.** (2004). Complex networks. *The European Physical Journal B - Condensed Matter*, 38(2), 147–162. <https://doi.org/10.1140/epjb/e2004-00110-5>
- Anderson, W. E., Miller, K. L., Ryan, H. M., Pal, S., Santoro, R. J., and Dressler, J. L.** (1998). Effects of Periodic Atomization on Combustion Instability in Liquid-Fueled Propulsion Systems. *Journal of Propulsion and Power*, 14(5), 818–825. <https://doi.org/10.2514/2.5345>
- Andreini, A., Facchini, B., Giusti, A., and Turrini, F.** (2014). Assessment of Flame Transfer Function Formulations for the Thermoacoustic Analysis of Lean Burn Aero-engine Combustors. *Energy Procedia*, 45, 1422–1431. <https://doi.org/https://doi.org/10.1016/j.egypro.2014.01.149>
- Ashwin, P., Wieczorek, S., Vitolo, R., and Cox, P.** (2012). Tipping points in open systems: Bifurcation, noise-induced and rate-dependent examples in the climate system. *Philosophical Transactions of the Royal Society A: Mathematical, Physical and Engineering Sciences*, 370(1962), 1166–1184. <https://doi.org/10.1098/rsta.2011.0306>
- Baer, S. M., Erneux, T., and Rinzel, J.** (1989). The slow passage through a Hopf bifurcation: Delay, memory effects, and resonance. *SIAM Journal on Applied Mathematics*, 49(1), 55–71. <https://doi.org/10.1137/0149003>
- Bennett, M., Schatz, M. F., Rockwood, H., and K. Wiesenfeld.** (2002). Huygens' s clocks. *Proc. R. Soc. Lond. A*, 458(Huygens 1669), 563–579.
- Biwa, T., Tozuka, S., and Yazaki, T.** (2015). Amplitude Death in Coupled Thermoacoustic Oscillators. *Physical Review Applied*, 3(3), 1–5. <https://doi.org/10.1103/PhysRevApplied.3.034006>
- Blackshear, P.** (1955). Study of screeching combustion in a 6 inch simulated afterburner. In *Naca* (Issue TN 3567).

- Blasius, B., and Tönjes, R.** (2007). Predator-prey oscillations, synchronization and pattern formation in ecological systems. In *Analysis and Control of Complex Nonlinear Processes in Physics, Chemistry and Biology: Vol. Volume 5* (pp. 397–427). WORLD SCIENTIFIC. https://doi.org/doi:10.1142/9789812706911_0015
- Bloxside, G. J., Dowling, A. P., and Langhorne, P. J.** (1988). Reheat buzz: an acoustically coupled combustion instability. Part 2. Theory. *Journal of Fluid Mechanics*, 193(1), 445. <https://doi.org/10.1017/S0022112088002216>
- Bonciolini, G., Boujo, E., and Noiray, N.** (2017). Output-only parameter identification of a colored-noise-driven Van-der-Pol oscillator: Thermoacoustic instabilities as an example. *Physical Review E*, 95(6), 1–15. <https://doi.org/10.1103/PhysRevE.95.062217>
- Bonciolini, G., Ebi, D., Boujo, E., and Noiray, N.** (2018). Experiments and modelling of rate-dependent transition delay in a stochastic subcritical bifurcation. *Royal Society Open Science*, 5(3), 1–18. <https://doi.org/10.1098/rsos.172078>
- Bonciolini, G., Ebi, D., Doll, U., Weilenmann, M., and Noiray, N.** (2019). Effect of wall thermal inertia upon transient thermoacoustic dynamics of a swirl-stabilized flame. *Proceedings of the Combustion Institute*, 37(4), 5351–5358. <https://doi.org/10.1016/j.proci.2018.06.229>
- Bunde, A., and Havlin, S.** (1996). Percolation I. In *Fractals and Disordered Systems* (pp. 59–114). Springer Berlin Heidelberg. https://doi.org/10.1007/978-3-642-84868-1_2
- Camazine, S., Franks, N., Sneyd, J., Bonabeau, E., Deneubourg, J.-L., and Theraulaz, G.** (2001). *Self-Organization in Biological Systems*.
- Candel, S.** (2002). Combustion dynamics and control: Progress and challenges. *Proceedings of the Combustion Institute*, 29(1), 1–28. [https://doi.org/10.1016/S1540-7489\(02\)80007-4](https://doi.org/10.1016/S1540-7489(02)80007-4)
- Chakravarthy, S. R., Shreenivasan, O. J., Boehm, B., Dreizler, A., and Janicka, J.** (2007). Experimental characterization of onset of acoustic instability in a nonpremixed half-dump combustor. *The Journal of the Acoustical Society of America*, 122(1), 120–127. <https://doi.org/10.1121/1.2741374>
- Clark, W.** (1984, June 11). Identification of longitudinal acoustic modes associated with pressure oscillations in ramjets. *20th Joint Propulsion Conference*. <https://doi.org/10.2514/6.1984-1405>

- CROCCO, L., GREY, J., and HARRJE, D. T.** (1960). Theory of Liquid Propellant Rocket Combustion Instability and Its Experimental Verification. *ARS Journal*, 30(2), 159–168. <https://doi.org/10.2514/8.5020>
- Culick, F. E. C.** (1988). Combustion instabilities in liquid-fueled propulsion systems - an overview. *AGARD Conference on Combustion Instabilities in Liquid-Fueled Propulsion Systems*, 450(450), 1.
- Culick, F. E. C., and Kuentzmann, P.** (2006). Unsteady motions in combustion chambers for propulsion systems. *NATO RTO-AG-AVT-039, AGARDograph*, 323(December).
- Culick, F. E. C., Papparizos, L., Sterling, J., and Burnley, V.** (1992). *Combustion noise and combustion instabilities in propulsion systems*. <http://authors.library.caltech.edu/21851/>
- Culick, F. E. C., and Rogers, T.** (1980). *Modeling pressure oscillations in Ramjets*.
- Dange, S., Manoj, K., Banerjee, S., Pawar, S. A., Mondal, S., and Sujith, R. I.** (2019). Oscillation quenching and phase-flip bifurcation in coupled thermoacoustic systems. *Chaos*, 29(9). <https://doi.org/10.1063/1.5114695>
- Domen, S., Gotoda, H., Kuriyama, T., Okuno, Y., and Tachibana, S.** (2015). Detection and prevention of blowout in a lean premixed gas-turbine model combustor using the concept of dynamical system theory. *Proceedings of the Combustion Institute*, 35(3), 3245–3253. <https://doi.org/10.1016/j.proci.2014.07.014>
- Dowling, A. P.** (1995). The calculation of thermoacoustic oscillations. *Journal of Sound and Vibration*, 180(4), 557–581. <https://doi.org/10.1006/jsvi.1995.0100>
- Dowling, A. P.** (1997). Nonlinear self-excited oscillations of a ducted flame. *Journal of Fluid Mechanics*, 346, 271–290. <https://doi.org/10.1017/S0022112097006484>
- Dowling, A. P.** (1999). A kinematic model of a ducted flame. *Journal of Fluid Mechanics*, 394, 51–72. <https://doi.org/10.1017/S0022112099005686>
- Dowling, A. P., and Mahmoudi, Y.** (2015). Combustion noise. *Proceedings of the Combustion Institute*, 35(1), 65–100. <https://doi.org/10.1016/j.proci.2014.08.016>
- Durox, D., Schuller, T., Noiray, N., and Candel, S.** (2009). Experimental analysis of nonlinear flame transfer functions for different flame geometries. *Proceedings of*

Ebi, D., Denisov, A., Bonciolini, G., Boujo, E., and Noiray, N. (2018). Flame dynamics intermittency in the bistable region near a subcritical Hopf bifurcation. *Journal of Engineering for Gas Turbines and Power*, 140(6), 61504. <https://doi.org/10.1115/1.4038326>

Ebi, D., Doll, U., Bombach, R., and Noiray, N. (2018). Simultaneous high-speed OH-PLIF and PIV of a turbulent swirl flame experiencing thermoacoustic bi-stability. *19th International Symposium on the Application of Laser and Imaging Techniques to Fluid Mechanics* · , July.

Elias, I. (1959). Acoustical resonances produced by combustion of a fuel-air mixture in a rectangular duct. *The Journal of the Acoustical Society of America*, 31(3), 296. <https://doi.org/10.1121/1.1907715>

Emerson, B., Mondragon, U., Acharya, V., Shin, D. H., Brown, C., McDonell, V., and Lieuwen, T. C. (2013). Velocity and flame wrinkling characteristics of a transversely forced, bluff-body stabilized flame, Part I: Experiments and data analysis. *Combustion Science and Technology*, 185(7), 1056–1076. <https://doi.org/10.1080/00102202.2013.777714>

Emerson, B., Mondragon, U., Brown, C., Acharya, V., Shin, D.-H., McDonell, V., and Lieuwen, T. C. (2011). Dynamics of a Transversely Forced, Bluff Body Stabilized Flame. *49th AIAA Aerospace Sciences Meeting Including the New Horizons Forum and Aerospace Exposition, January*, 1–14. <https://doi.org/10.2514/6.2011-600>

Eser, J., Zheng, P., and Triesch, J. (2014). Nonlinear dynamics analysis of a self-organizing recurrent neural network: Chaos waning. *PLoS ONE*, 9(1). <https://doi.org/10.1371/journal.pone.0086962>

Fleifil, M., and Annaswamy, A. (1996). Response of a laminar premixed flame to flow oscillations: A kinematic model and thermoacoustic instability results. ... *and Flame*, 2180(96), 487–510. <http://www.sciencedirect.com/science/article/pii/0010218096000491>

Gentili, D., Valle, F., Albonetti, C., Liscio, F., and Cavallini, M. (2014). Self-Organization of Functional Materials in Confinement. *Accounts of Chemical Research*, 47(8), 2692–2699. <https://doi.org/10.1021/ar500210d>

George, N. B., Unni, V. R., Raghunathan, M., and Sujith, R. I. (2018). Pattern

formation during transition from combustion noise to thermoacoustic instability via intermittency. *Journal of Fluid Mechanics*, 849, 615–644. <https://doi.org/10.1017/jfm.2018.427>

Ghani, A., Poinso, T., Gicquel, L., and Staffelbach, G. (2015). LES of longitudinal and transverse self-excited combustion instabilities in a bluff-body stabilized turbulent premixed flame. *Combustion and Flame*, 162(11), 4075–4083. <https://doi.org/10.1016/j.combustflame.2015.08.024>

Glass, L. (2001). Synchronization and rhythmic processes in physiology. *Nature*, 410(6825), 277–284. <https://doi.org/10.1038/35065745>

Godavarthi, V., Unni, V. R., Gopalakrishnan, E. A., and Sujith, R. I. (2017). Recurrence networks to study dynamical transitions in a turbulent combustor. *Chaos*, 27(6). <https://doi.org/10.1063/1.4985275>

Goswami, B., Ambika, G., Marwan, N., and Kurths, J. (2012). On interrelations of recurrences and connectivity trends between stock indices. *Physica A: Statistical Mechanics and Its Applications*, 391(18), 4364–4376. <https://doi.org/10.1016/j.physa.2012.04.018>

Gotoda, H., Amano, M., Miyano, T., Ikawa, T., Maki, K., and Tachibana, S. (2012). Characterization of complexities in combustion instability in a lean premixed gas-turbine model combustor. *Chaos*, 22(4). <https://doi.org/10.1063/1.4766589>

Gotoda, H., Hayashi, K., Tsujimoto, R., Domen, S., and Tachibana, S. (2017). Dynamical properties of combustion instability in a laboratory-scale gas-turbine model combustor. *Journal of Engineering for Gas Turbines and Power*, 139(4), 41509.

Gotoda, H., Shinoda, Y., Kobayashi, M., Okuno, Y., and Tachibana, S. (2014). Detection and control of combustion instability based on the concept of dynamical system theory. *Physical Review E - Statistical, Nonlinear, and Soft Matter Physics*, 89(2), 22910. <https://doi.org/10.1103/PhysRevE.89.022910>

Grebogi, C., Ott, E., Romeiras, F., and Yorke, J. A. (1987). Critical exponents for crisis-induced intermittency. *Physical Review A*, 36(11), 5365–5380. <https://doi.org/10.1103/PhysRevA.36.5365>

Grinsted, A., Moore, J. C., and Jevrejeva, S. (2004). Application of the cross wavelet transform and wavelet coherence to geophysical time series. *Nonlin. Processes Geophys.*, 11(5/6), 561–566. <https://doi.org/10.5194/npg-11-561-2004>

- Gunnoo, H., Abcha, N., and Ezersky, A.** (2016). Frequency lock-in and phase synchronization of vortex shedding behind circular cylinder due to surface waves. *Physics Letters A*, 380(7), 863–868. <https://doi.org/https://doi.org/10.1016/j.physleta.2015.12.029>
- Hammer, P. W., Platt, N., Hammel, S. M., Heagy, J. F., and Lee, B. D.** (1994). Experimental observation of on-off intermittency. *Physical Review Letters*, 73(8), 1095–1098. <https://doi.org/10.1103/PhysRevLett.73.1095>
- Hegde, U. G., Reuter, D., Daniel, B. R., and Zinn, B. T.** (1987). Flame Driving of Longitudinal Instabilities in Dump Type Ramjet Combustors. *Combustion Science and Technology*, 55(4–6), 125–138. <https://doi.org/10.1080/00102208708947075>
- Hemchandra, S., Peters, N., and Lieuwen, T. C.** (2011). Heat release response of acoustically forced turbulent premixed flames—role of kinematic restoration. *Proceedings of the Combustion Institute*, 33(1), 1609–1617. <https://doi.org/10.1016/j.proci.2010.06.115>
- Heydarlaki, R., Aitchison, W., Kostka, P., and Kheirkhah, S.** (2019). Influences of initial and transient combustor wall-temperature on thermoacoustic oscillations of a small-scale power generator. *Experimental Thermal and Fluid Science*, 109, 109856. <https://doi.org/10.1016/j.expthermflusci.2019.109856>
- Higuera-Toledano, M. T., Brinkschulte, U., and Rettberg, A.** (Eds.). (2013). *Self-Organization in Embedded Real-Time Systems*. Springer New York. <https://doi.org/10.1007/978-1-4614-1969-3>
- Hirsch, J. E., Huberman, B. A., and Scalapino, D. J.** (1982). Theory of intermittency. *Physical Review A*, 25(1), 519–532. <https://doi.org/10.1103/PhysRevA.25.519>
- Ho, C.-M.** (1984). Perturbed Free Shear Layers. *Annual Review of Fluid Mechanics*, 16(1), 365–424. <https://doi.org/10.1146/annurev.fluid.16.1.365>
- Issartel, J., Bardainne, T., Gaillot, P., and Marin, L.** (2015). The relevance of the cross-wavelet transform in the analysis of human interaction – a tutorial . In *Frontiers in Psychology* (Vol. 5, p. 1566). <https://www.frontiersin.org/article/10.3389/fpsyg.2014.01566>
- Jones, A. T.** (1945). Singing Flames. *The Journal of the Acoustical Society of America*, 16(4), 254–266. <https://doi.org/10.1121/1.1916288>
- Kabiraj, L., and Sujith, R. I.** (2012). Nonlinear self-excited thermoacoustic

oscillations: intermittency and flame blowout. *Journal of Fluid Mechanics*, 713, 1–22. <https://doi.org/10.1017/jfm.2012.463>

Kabiraj, L., Sujith, R. I., and Wahi, P. (2012). Bifurcations of self-excited ducted laminar premixed flames. *Journal of Engineering for Gas Turbines and Power*, 134(3), 031502. <https://doi.org/10.1115/1.4004402>

Karlis, E., Liu, Y., Hardalupas, Y., and Taylor, A. M. K. P. (2019). H₂ enrichment of CH₄ blends in lean premixed gas turbine combustion: An experimental study on effects on flame shape and thermoacoustic oscillation dynamics. *Fuel*, 254. <https://doi.org/10.1016/j.fuel.2019.05.107>

Kerbs, W., Bethke, S., Lepers, J., Flohr, P., and Prade, B. (2006). Thermoacoustic design tools and passive control: Siemens power generation approaches. In *Combustion Instabilities In Gas Turbine Engines: Operational Experience, Fundamental Mechanisms, and Modeling* (pp. 89–112). American Institute of Aeronautics and Astronautics. <https://doi.org/doi:10.2514/5.9781600866807.0089.0112>

Kheirkhah, S., Gülder, Ö. L., Maurice, G., Halter, F., and Gökalp, I. (2016). On periodic behavior of weakly turbulent premixed flame corrugations. *Combustion and Flame*, 168, 147–165. <https://doi.org/10.1016/j.combustflame.2016.03.013>

Kolumban, G., Kennedy, M. P., and Chua, L. O. (1997). The role of synchronization in digital communications using chaos. I . Fundamentals of digital communications. *IEEE Transactions on Circuits and Systems I: Fundamental Theory and Applications*, 44(10), 927–936. <https://doi.org/10.1109/81.633882>

Krishnan, A., Manikandan, R., Midhun, P. R., Reeja, K. V., Unni, V. R., Sujith, R. I., Marwan, N., and Kurths, J. (2019). Mitigation of oscillatory instability in turbulent reactive flows: A novel approach using complex networks. *EPL (Europhysics Letters)*, 128(1), 14003. <https://doi.org/10.1209/0295-5075/128/14003>

Krishnan, A., Sujith, R. I., Marwan, N., and Kurths, J. (2019). On the emergence of large clusters of acoustic power sources at the onset of thermoacoustic instability in a turbulent combustor. *Journal of Fluid Mechanics*, 455–482. <https://doi.org/10.1017/jfm.2019.429>

Lacasa, L., Luque, B., Ballesteros, F., Luque, J., and Nuño, J. C. (2008). From time series to complex networks: the visibility graph. *Proceedings of the National Academy of Sciences of the United States of America*, 105(13), 4972–4975. <https://doi.org/10.1073/pnas.0709247105>

- Langhorne, P., and Bloxside, G.** (1988). Reheat buzz: an acoustically coupled combustion instability. Part 1. Experiment. *Journal of Fluid Mechanics*, 193. http://journals.cambridge.org/abstract_S0022112088002216
- Leitner, S., and Wall, F.** (Eds.). (2014). *Artificial Economics and Self Organization* (Vol. 669). Springer International Publishing. <https://doi.org/10.1007/978-3-319-00912-4>
- Li, J., Chou, S. K., Huang, G., Yang, W. M., and Li, Z. W.** (2009). Study on premixed combustion in cylindrical micro combustors: Transient flame behavior and wall heat flux. *Experimental Thermal and Fluid Science*, 33(4), 764–773. <https://doi.org/10.1016/J.EXPTHERMFLUSCI.2009.01.012>
- Lieuwen, T. C.** (2003). Statistical characteristics of pressure oscillations in a premixed combustor. *Journal of Sound and Vibration*, 260(1), 3–17. <http://www.sciencedirect.com/science/article/pii/S0022460X02008957>
- Lieuwen, T. C., and Banaszuk, A.** (2005). Background noise effects on combustor stability. *Journal of Propulsion and Power*, June, 1–10. <http://arc.aiaa.org/doi/pdf/10.2514/1.5549>
- Lieuwen, T. C., and Yang, V.** (2006). Combustion Instabilities In Gas Turbine Engines. In *Volume 210 Progress in Astronautics and Aeronautics*. American Institute of Aeronautics and Astronautics. <https://doi.org/10.2514/4.866807>
- Lilly, J M, and Olhede, S. C.** (2012). Generalized Morse Wavelets as a Superfamily of Analytic Wavelets. *IEEE Transactions on Signal Processing*, 60(11), 6036–6041. <https://doi.org/10.1109/TSP.2012.2210890>
- Lilly, Jonathan M.** (2017). Element analysis: a wavelet-based method for analysing time-localized events in noisy time series. *Proceedings. Mathematical, Physical, and Engineering Sciences*, 473(2200), 20160776. <https://doi.org/10.1098/rspa.2016.0776>
- Luque, B., Lacasa, L., Ballesteros, F., and Luque, J.** (2009). Horizontal visibility graphs: Exact results for random time series. *Physical Review E - Statistical, Nonlinear, and Soft Matter Physics*, 80(4), 1–11. <https://doi.org/10.1103/PhysRevE.80.046103>
- Majumdar, A., Ockendon, J., Howell, P., and Surovyatkina, E.** (2013). Transitions through critical temperatures in nematic liquid crystals. *Physical Review E*, 88(2), 022501. <https://doi.org/10.1103/PhysRevE.88.022501>

- Mandel, P., and Erneux, T.** (1984). Laser Lorenz equations with a time-dependent parameter. *Physical Review Letters*, 53(19), 1818–1820. <https://doi.org/10.1103/PhysRevLett.53.1818>
- Mandel, P., and Erneux, T.** (1987). The slow passage through a steady bifurcation: Delay and memory effects. *Journal of Statistical Physics*, 48(5–6), 1059–1070. <https://doi.org/10.1007/BF01009533>
- Mannella, R., Moss, F., and McClintock, P. V. E.** (1987). Postponed bifurcations of a ring-laser model with a swept parameter and additive colored noise. *Physical Review A*, 35(6), 2560–2566. <https://doi.org/10.1103/PhysRevA.35.2560>
- Marov, M. Y., and Kolesnichenko, A. V.** (2013). *Turbulence and Self-Organization* (Vol. 389). Springer New York. <https://doi.org/10.1007/978-1-4614-5155-6>
- Mikhailov, A. S., and Ertl, G.** (2017). *Chemical Complexity*. Springer International Publishing. <https://doi.org/10.1007/978-3-319-57377-9>
- Miyazaki, J.** (2013). *Pattern Formations and Oscillatory Phenomena: 2. Belousov–Zhabotinsky Reaction*. Elsevier Science. <https://books.google.co.in/books?id=60F2DAAAQBAJ>
- Mondal, S., Pawar, S. A., and Sujith, R. I.** (2017). Synchronous behaviour of two interacting oscillatory systems undergoing quasiperiodic route to chaos. *Chaos*, 27(10). <https://doi.org/10.1063/1.4991744>
- Mondal, S., Pawar, S. A., and Sujith, R. I.** (2019). Forced synchronization and asynchronous quenching of periodic oscillations in a thermoacoustic system. *Journal of Fluid Mechanics*, 864, 73–96. <https://doi.org/10.1017/jfm.2018.1011>
- Mondal, S., Unni, V. R., and Sujith, R. I.** (2017). Onset of thermoacoustic instability in turbulent combustors: An emergence of synchronized periodicity through formation of chimera-like states. *Journal of Fluid Mechanics*, 811, 659–681. <https://doi.org/10.1017/jfm.2016.770>
- Mongia, H. C., Held, T. J., Hsiao, G. C., and Pandalai, R. C.** (2006). Incorporation of combustion instability issues into design process: GE aero derivative and aero engines experience. In *Combustion Instabilities In Gas Turbine Engines: Operational Experience, Fundamental Mechanisms, and Modeling* (pp. 43–63). American Institute of Aeronautics and Astronautics. <https://doi.org/doi:10.2514/5.9781600866807.0043.0063>

- Murat Altay, H., Hudgins, D. E., Speth, R. L., Annaswamy, A. M., and Ghoniem, A. F.** (2010). Mitigation of thermoacoustic instability utilizing steady air injection near the flame anchoring zone. *Combustion and Flame*, 157(4), 686–700. <https://doi.org/10.1016/j.combustflame.2010.01.012>
- Murata, S., and Kurokawa, H.** (2012). *Self-Organizing Robots* (Vol. 77). Springer Tokyo. <https://doi.org/10.1007/978-4-431-54055-7>
- Murayama, S., and Gotoda, H.** (2019). Attenuation behavior of thermoacoustic combustion instability analyzed by a complex-network- and synchronization-based approach. *Physical Review E*, 99(5), 1–8. <https://doi.org/10.1103/PhysRevE.99.052222>
- Murugesan, M., and Sujith, R. I.** (2014). *Threshold grouping method to derive complex networks from time series*. 4(7), 17–23.
- Murugesan, M., and Sujith, R. I.** (2015). Combustion noise is scale-free: Transition from scale-free to order at the onset of thermoacoustic instability. *Journal of Fluid Mechanics*, 772, 225–245. <https://doi.org/10.1017/jfm.2015.215>
- Nair, V., and Sujith, R. I.** (2014a). A reduced-order model for the onset of combustion instability: Physical mechanisms for intermittency and precursors. *Proceedings of the Combustion Institute*, 35(3), 3193–3200. <https://doi.org/10.1016/j.proci.2014.07.007>
- Nair, V., and Sujith, R. I.** (2014b). Multifractality in combustion noise: predicting an impending combustion instability. *Journal of Fluid Mechanics*, 747(x), 635–655. <https://doi.org/10.1017/jfm.2014.171>
- Nair, V., Thampi, G., Karuppusamy, S., Gopalan, S., and Sujith, R. I.** (2013). Loss of chaos in combustion noise as a precursor of impending combustion instability. *International Journal of Spray and Combustion Dynamics*, 5(4), 273–290. <https://doi.org/10.1260/1756-8277.5.4.273>
- Nair, V., Thampi, G., and Sujith, R. I.** (2014a). Intermittency route to thermoacoustic instability in turbulent combustors. *Journal of Fluid Mechanics*, 756, 470–487. <https://doi.org/10.1017/jfm.2014.468>
- Nair, V., Thampi, G., and Sujith, R. I.** (2014b). Intermittency route to thermoacoustic instability in turbulent combustors. *Journal of Fluid Mechanics*, 756, 470–487. <https://doi.org/10.1017/jfm.2014.468>

- Noiray, N., and Schuermans, B.** (2013a). On the dynamic nature of azimuthal thermoacoustic modes in annular gas turbine combustion chambers. *Proceedings of the Royal Society A: Mathematical, Physical and Engineering Sciences*, 469(2151), 20120535. <https://doi.org/10.1098/rspa.2012.0535>
- Noiray, N., and Schuermans, B.** (2013b). Deterministic quantities characterizing noise driven Hopf bifurcations in gas turbine combustors. *International Journal of Non-Linear Mechanics*, 50, 152–163. <https://doi.org/10.1016/j.ijnonlinmec.2012.11.008>
- Okuno, Y., Small, M., and Gotoda, H.** (2015). Dynamics of self-excited thermoacoustic instability in a combustion system: Pseudo-periodic and high-dimensional nature. *Chaos*, 25(4), 10–15. <https://doi.org/10.1063/1.4914358>
- Orsucci, F., Giuliani, A., Webber, C., Zbilut, J., Fonagy, P., and Mazza, M.** (2006). Combinatorics and synchronization in natural semiotics. *Physica A: Statistical Mechanics and Its Applications*, 361(2), 665–676. <https://doi.org/https://doi.org/10.1016/j.physa.2005.06.044>
- Parkar, L. J., Sawyer, R. F., and Ganji, A. R.** (1979). Measurement of Vortex Frequencies in a Lean, Premixed Prevaporized Combustor†. *Combustion Science and Technology*, 20(5–6), 235–241. <https://doi.org/10.1080/00102207908946912>
- Parmentier, J.-F., Salas, P., Wolf, P., Staffelbach, G., Nicoud, F., and Poinso, T.** (2012). A simple analytical model to study and control azimuthal instabilities in annular combustion chambers. *Combustion and Flame*, 159(7), 2374–2387. <https://doi.org/10.1016/j.combustflame.2012.02.007>
- Paschereit, C., Schuermans, B., and Campos-Delgado, D.** (2001). Active combustion control using an evolution algorithm. *39th Aerospace Sciences Meeting and Exhibit, c.* <https://doi.org/10.2514/6.2001-783>
- Pavithran, I., Unni, V. R., Varghese, A. J., Sujith, R. I., Saha, A., Marwan, N., and Kurths, J.** (2020). Universality in the emergence of oscillatory instabilities in turbulent flows. *EPL (Europhysics Letters)*, 129(2), 24004. <https://doi.org/10.1209/0295-5075/129/24004>
- Pawar, S. A., Seshadri, A., Unni, V. R., and Sujith, R. I.** (2017). Thermoacoustic instability as mutual synchronization between the acoustic field of the confinement and turbulent reactive flow. *Journal of Fluid Mechanics*, 827, 664–693. <https://doi.org/10.1017/jfm.2017.438>
- Pawar, S. A., and Sujith, R. I.** (2018a). Transition to thermoacoustic instability in a

- turbulent combustor. *Journal of the Combustion Society of Japan*, 60(192), 99–111. https://doi.org/10.20619/jcombsj.60.192_99
- Pawar, S. A., and Sujith, R. I.** (2018b). *Intermittency: A State that Precedes Thermoacoustic Instability* (pp. 403–430). https://doi.org/10.1007/978-981-10-7449-3_14
- Pawar, S. A., Vishnu, R., Vadivukkarasan, M., Panchagnula, M. V., and Sujith, R. I.** (2015). Intermittency route to combustion instability in a laboratory spray combustor. *Journal of Engineering for Gas Turbines and Power*, 138(4), 041505. <https://doi.org/10.1115/1.4031405>
- Pikovsky, A., Rosenblum, M., and Kurths, J.** (2001). *Synchronization*. Cambridge University Press. <https://doi.org/10.1017/CBO9780511755743>
- Pitz, R. W., and Daily, J. W.** (1983). Combustion in a turbulent mixing layer formed at a rearward-facing step. *AIAA Journal*, 21(11), 1565–1570. <https://doi.org/10.2514/3.8290>
- Platt, N., Hammel, S. M., and Heagy, J. F.** (1994). Effects of additive noise on on-off intermittency. *Physical Review Letters*, 72(22), 3498–3501. <https://doi.org/10.1103/PhysRevLett.72.3498>
- Poinsot, T. J., Trounev, A. C., Veynante, D. P., Candel, S. M., and Esposito, E. J.** (1987). Vortex-driven acoustically coupled combustion instabilities. In *Journal of Fluid Mechanics* (Vol. 177, Issue 1, p. 265). <https://doi.org/10.1017/S0022112087000958>
- Pomeau, Y., and Manneville, P.** (1980). Intermittent transition to turbulence in dissipative dynamical systems. *Communications in Mathematical Physics*, 74(2), 189–197. <https://doi.org/10.1007/BF01197757>
- Rani, V. K., and Rani, S. L.** (2018). Development of a comprehensive flame transfer function and its application to predict combustion instabilities in a dump combustor. *Combustion Science and Technology*, 190(8), 1313–1353. <https://doi.org/10.1080/00102202.2018.1440215>
- Rayleigh, Lord.** (1878). The explanation of certain acoustical phenomena. *Roy. Inst. Proc.*, 8(455), 319–321. <https://doi.org/10.1038/018319a0>
- Read, P. L., and Castrejón-Pita, A. A.** (2010). *Synchronization in Climate Dynamics and Other Extended Systems BT - Nonlinear Dynamics and Chaos: Advances and*

Perspectives (M. Thiel, J. Kurths, M. C. Romano, G. Károlyi, and A. Moura (Eds.); pp. 153–176). Springer Berlin Heidelberg. https://doi.org/10.1007/978-3-642-04629-2_8

Repp, B. H., and Su, Y.-H. (2013). Sensorimotor synchronization: A review of recent research (2006–2012). *Psychonomic Bulletin & Review*, 20(3), 403–452. <https://doi.org/10.3758/s13423-012-0371-2>

Rogers, D. E. (1956). A Mechanism for High-Frequency Oscillation in Ramjet Combustors and Afterburners. *Journal of Jet Propulsion*, 26(6), 456–462. <https://doi.org/10.2514/8.7049>

Rogers, D. E., and Marble, F. E. (1956). A mechanism for high-frequency oscillation in ramjet combustors and afterburners. *Journal of Jet Propulsion*, 26(6), 456–462. <https://doi.org/10.2514/8.7049>

Romano, M. C., Thiel, M., Kurths, J., Kiss, I. Z., and Hudson, J. L. (2005). Detection of synchronization for non-phase-coherent and non-stationary data. *Europhysics Letters*, 71(3), 466–472. <https://doi.org/10.1209/epl/i2005-10095-1>

Schadow, K. C., and Gutmark, E. (1992). Combustion instability related to vortex shedding in dump combustors and their passive control. *Progress in Energy and Combustion Science*, 18(2), 117–132. [https://doi.org/10.1016/0360-1285\(92\)90020-2](https://doi.org/10.1016/0360-1285(92)90020-2)

Schuller, T., Durox, D., and Candel, S. (2003). A unified model for the prediction of laminar flame transfer functions. *Combustion and Flame*, 134(1–2), 21–34. [https://doi.org/10.1016/S0010-2180\(03\)00042-7](https://doi.org/10.1016/S0010-2180(03)00042-7)

Schuller, Thierry, Ducruix, S., Durox, D., and Candel, S. (2002). Modeling tools for the prediction of premixed flame transfer functions. *Proceedings of the Combustion Institute*, 29(1), 107–113. [https://doi.org/10.1016/S1540-7489\(02\)80018-9](https://doi.org/10.1016/S1540-7489(02)80018-9)

Schwing, J., Sattelmayer, T., and Noiray, N. (2011). Interaction of vortex shedding and transverse high-frequency pressure oscillations in a tubular combustion chamber. *Proceedings of the ASME Turbo Expo 2011, Vancouver, British Columbia, Canada*, 1–10. <https://doi.org/GT2011-45246>

Shanbhogue, S., Shin, D.-H., Hemchandra, S., Plaks, D., and Lieuwen, T. C. (2009). Flame sheet dynamics of bluff-body stabilized flames during longitudinal acoustic forcing. *Proceedings of the Combustion Institute*, 32(2), 1787–1794. <https://doi.org/10.1016/j.proci.2008.06.034>

- Shcherbik, D., Cross, C. N., Fricker, A., Bibik, O., Scarborough, D., Lubarsky, E., and Zinn, B. T.** (2009). Dynamics of V-gutter-stabilized Jet-A flames in a single flame holder combustor with full optical access. In *45th AIAA/ASME/SAE/ASEE Joint Propulsion Conference and Exhibit* (p. 5291). American Institute of Aeronautics and Astronautics. <https://doi.org/10.2514/6.2009-5291>
- Shin, D.-H., Plaks, D. V., Lieuwen, T. C., Mondragon, U. M., Brown, C. T., and McDonell, V. G.** (2011). Dynamics of a Longitudinally Forced, Bluff Body Stabilized Flame. *Journal of Propulsion and Power*, 27(1), 105–116. <https://doi.org/10.2514/1.48056>
- Sivasegaram, S., Thompson, B. E., and Whitelaw, J. H.** (1989). Acoustic characterization relevant to gas turbine augmentors. *Journal of Propulsion and Power*, 5(1), 109–115. <https://doi.org/10.2514/3.23122>
- Smith, D., and Zukoski, E.** (1985). *Combustion instability sustained by unsteady vortex combustion*. <http://authors.library.caltech.edu/21176/>
- Sole, R., and Bascompte, J.** (2012). Self-organization in complex ecosystems. *Self-Organization in Complex Ecosystems*, 1–373.
- Stanley, H. E.** (1987). *Introduction to Phase Transitions and Critical Phenomena*. Oxford University Press. <https://books.google.co.in/books?id=C3BzcUxoANkC>
- Sterling, J. D., and Zukoski, E. E.** (1991). Nonlinear Dynamics of Laboratory Combustor Pressure Oscillations. *Combustion Science and Technology*, 77(4–6), 225–238. <https://doi.org/10.1080/00102209108951729>
- Strahle, W. C.** (1978). Combustion noise. *Progress in Energy and Combustion Science*, 4(3), 157–176. [https://doi.org/10.1016/0360-1285\(78\)90002-3](https://doi.org/10.1016/0360-1285(78)90002-3)
- Strogatz, S. H.** (2018). *Nonlinear Dynamics and Chaos*. CRC Press. <https://doi.org/10.1201/9780429492563>
- Sujith, R. I., and Unni, V. R.** (2020). Complex system approach to investigate and mitigate thermoacoustic instability in turbulent combustors. *Physics of Fluids*, 32(6), 061401. <https://doi.org/10.1063/5.0003702>
- Tan, C. O., Cohen, M. A., Eckberg, D. L., and Taylor, J. A.** (2009). Fractal properties of human heart period variability: Physiological and methodological implications. *Journal of Physiology*, 587(15), 3929–3941. <https://doi.org/10.1113/jphysiol.2009.169219>

- Tass, P., Rosenblum, M. G., Weule, J., Kurths, J., Pikovsky, A., Volkmann, J., Schnitzler, A., and Freund, H.-J.** (1998). Detection of n:m Phase Locking from Noisy Data: Application to Magnetoencephalography. *Physical Review Letters*, 81(15), 3291–3294. <https://doi.org/10.1103/PhysRevLett.81.3291>
- Thomas, N., Mondal, S., Pawar, S. A., and Sujith, R. I.** (2018). Effect of time-delay and dissipative coupling on amplitude death in coupled thermoacoustic oscillators. *Chaos*, 28(3). <https://doi.org/10.1063/1.5009999>
- Tony, J., Subarna, S., Syamkumar, K. S., Sudha, G., Akshay, S., Gopalakrishnan, E. A., Surovyatkina, E., and Sujith, R. I.** (2017). Experimental investigation on preconditioned rate induced tipping in a thermoacoustic system. *Scientific Reports*, 7(1), 1–7. <https://doi.org/10.1038/s41598-017-05814-y>
- Torrence, C., and Compo, G. P.** (1998). A Practical Guide to Wavelet Analysis. *Bulletin of the American Meteorological Society*, 79(1), 61–78. [https://doi.org/10.1175/1520-0477\(1998\)079<0061:APGTWA>2.0.CO;2](https://doi.org/10.1175/1520-0477(1998)079<0061:APGTWA>2.0.CO;2)
- Trout, A. M., Koffel, W. K., and Smolak, G. R.** (1956). Investigation of afterburner combustion screech and methods of its control at high combustor pressure levels. *NACA-RM-E55K25*.
- Uhm, J. H., and Acharya, S.** (2004). Control of combustion instability with a high-momentum air-jet. *Combustion and Flame*, 139(1–2), 106–125. <https://doi.org/10.1016/j.combustflame.2004.07.007>
- Unni, V. R., Krishnan, A., Manikandan, R., George, N. B., Sujith, R. I., Marwan, N., and Kurths, J.** (2018). On the emergence of critical regions at the onset of thermoacoustic instability in a turbulent combustor. *Chaos*, 28(6). <https://doi.org/10.1063/1.5028159>
- Unni, V. R., and Sujith, R. I.** (2017). Flame dynamics during intermittency in a turbulent combustor. *Proceedings of the Combustion Institute*, 36(3), 3791–3798. <https://doi.org/10.1016/j.proci.2016.08.030>
- Wieczorek, S., Ashwin, P., Luke, C. M., and Cox, P. M.** (2011). Excitability in ramped systems: The compost-bomb instability. *Proceedings of the Royal Society A: Mathematical, Physical and Engineering Sciences*, 467(2129), 1243–1269. <https://doi.org/10.1098/rspa.2010.0485>
- Wilhite, J. M., Dolan, B. J., Kabiraj, L., Villalva Gomez, R., Gutmark, E. J., and Paschereit, C. O.** (2016). Analysis of combustion oscillations in a staged MLDI burner using decomposition methods and recurrence analysis. *54th AIAA*

Aerospace Sciences Meeting, 1156. <https://doi.org/10.2514/6.2016-1156>

Xiao, Y., Wang, Y., and Lai, Y. C. (2009). Dependence of intermittency scaling on threshold in chaotic systems. *Physical Review E - Statistical, Nonlinear, and Soft Matter Physics*, 80(5). <https://doi.org/10.1103/PhysRevE.80.057202>

Yu, K. H., Trouvé, A., and Daily, J. W. (1991). Low-frequency pressure oscillations in a model ramjet combustor. *Journal of Fluid Mechanics*, 232(1), 47. <https://doi.org/10.1017/S0022112091003622>

Zdravkovich, M. M. (1982). Modification of Vortex Shedding in the Synchronization Range. *Journal of Fluids Engineering*, 104(4), 513–517. <https://doi.org/10.1115/1.3241895>

Zhou, H., Tao, C., Liu, Z., Meng, S., and Cen, K. (2020). Optimal control of turbulent premixed combustion instability with annular micropore air jets. *Aerospace Science and Technology*, 98, 105650. <https://doi.org/10.1016/j.ast.2019.105650>

Zorick, T., and Mandelkern, M. A. (2013). Multifractal Detrended Fluctuation Analysis of Human EEG: Preliminary Investigation and Comparison with the Wavelet Transform Modulus Maxima Technique. *PLoS ONE*, 8(7), 1–7. <https://doi.org/10.1371/journal.pone.0068360>

Zukoski, E. E., and Marble, F. E. (1955). The role of wake transition in the process of flame stabilization on bluff bodies. *AGARD Combustion Researches and Reviews*, 167–180.